Magnetic Field Induced Optical Harmonic Generation in the Semiconductors ZnO and EuX

Dissertation

presented to the Institute of Physics of the
TU Dortmund University, Germany,
in partial fulfillment of the requirements
for the degree of

Doktor rer. nat.

by
Marco Lafrentz

technische universität
dortmund

Dortmund, August 2013

Day of the oral examination: 27th September, 2013

Examination board:
Prof. Dr. Dmitri R. Yakovlev
Prof. Dr. Metin Tolan
Dr. Bärbel Siegmann
Prof. Dr. Bernhard Spaan

Contents

Introduction

Interactions of very intense and coherent light fields provided by modern laser systems with media reveal optical phenomena showing nonlinear dependences on the incident light intensity [1–3]. This research field called nonlinear optics gains continuously more attention and its achievements find applications in multiple fields of science [3–5]. Among them, frequency conversion processes, where new colors are generated from monochromatic light, like harmonics generation, parametric generation, or four-wave mixing are particularly interesting for technology. These processes allow the production of laser systems at frequencies that are unavailable otherwise. Profound examples in modern technology are green and blue lasers achieved by frequency doubling.

The fundamental three photon process, where two photons of the same frequency are converted to one photon with twice the frequency called second harmonic generation (SHG), has a distinctively prominent role among the manifold processes [6]. The selection rules of SHG are radically different from linear optics opening new avenues to probe the optical and electronic properties of a system. SHG has become a widely used tool to investigate all different kinds of materials reaching from bulk semiconductors and colloidal quantum dots to molecules and complex chemical compounds [1, 4, 7]. Even in medical research SHG leads to prosperous insights, e.g., the high spatial resolution microscopy of the eye [8, 9]. Utilizing such optical nonlinearities successfully requires the detailed understanding of their underlying processes.

SHG studies on semiconductors have attracted a lot of attention since the beginning of nonlinear optics, leading to thousands of related publications. Especially the pronounced sensitivity towards symmetries promises magnificent opportunities for studies in applied fields [10]. Magnetic and electric fields are appropriate controls to selectively break inherent symmetries. In the last decade manifold magnetic field induced contributions to SHG were identified [11]. In the diamagnetic semiconductors GaAs and CdTe the magnetic field induced second harmonic (MFISH) was attributed to the orbital quantization of Landau-Levels [12]. In diluted magnetic semiconductors (Cd,Mn)Te the MFISH was shown to stem from the large spin splittings [13]. In the magnetic compounds EuTe and EuSe the MFISH was traced down to originate from the parallel alignment of their spin sub-lattices [14].

The optical properties of semiconductors are largely determined by excitons, bound electron-hole pairs, which have been intensively studied by linear optics. Surpris-

ingly, the role of excitons in the SHG process has remained essentially unexplored in experimental and theoretical studies. This gap motivates the spectroscopic study of SHG in hexagonal ZnO. It has a rich exciton structure and is well suited to investigate the influence of excitons on SHG.

In case the SHG is forbidden, e.g., in centrosymmetric materials, allowed third harmonic generation (THG) contributions might be studied instead. In contrast to SHG spectroscopy, publications on THG spectroscopy are scarce. The spectroscopic study of THG in cubic, magnetic EuTe and EuSe is performed in order to discuss its strengths and advantages. In addition, the results are compared to recent spectroscopic SHG studies in the same materials [15].

Gained perceptions are deepened and expanded by exploring the influence of controllable external magnetic and electric fields. Such perturbations break specific symmetries purposefully leading to induced contributions. The additional adjustable parameters enrich the experimental capabilities.

This thesis is structured in three parts: First, an introduction to harmonic generation spectroscopy provides the theoretical background and presents the experimental setup. Second, the second harmonic generation spectroscopy of the exciton structure in wurtzite ZnO is analyzed and interpreted on the basis of a microscopic discussion. Thirdly, the third harmonic generation spectroscopy in vicinity of the band gap in cubic, magnetic EuSe and EuTe is discussed and, afterwards, compared to the second harmonic generation spectroscopy studies.

1 Optical Harmonic Generation Spectroscopy

Optical harmonic generation can be derived phenomenologically from the very basic principles of electromagnetism, although quantum mechanics are necessary to fully grasp the nature of this phenomenon.

1.1 Theoretical Background

First, the generation of optical harmonic waves is derived as a direct consequence of the Maxwell's equations. Second, the polarization and the susceptibility of a medium is introduced and discussed. Thirdly, the quantum mechanical origin of the susceptibilities is outlined.

1.1.1 Electromagnetic Wave Equation

Maxwell's equations comprise the complete set of equations, which are necessary to describe the dynamics of electromagnetic problems. In the form of effective charges and currents (all charges/currents are summed up in an effective charge/current), they can be written in the microscopic form; see for example Refs. [3, 16]:

$$\text{div } \mathbf{E} = \frac{\tilde{\rho}}{\epsilon_0} \tag{1.1}$$

$$\text{div } \mathbf{B} = 0 \tag{1.2}$$

$$\text{curl } \mathbf{E} = -\mu_0 \frac{\partial \mathbf{B}}{\partial t} \tag{1.3}$$

$$\text{curl } \mathbf{B} = \epsilon_0 \mu_0 \frac{\partial \mathbf{E}}{\partial t} + \mu_0 \tilde{\mathbf{j}} \tag{1.4}$$

Here, $\mathbf{E}$ and $\mathbf{B}$ are the electric and magnetic fields[1], ϵ_0 and μ_0 the dielectric and magnetic constants, $\tilde{\rho}$ and $\tilde{\mathbf{j}}$ are the effective charge and current densities. Taking

[1] More accurately, $\mathbf{E}$ is the electric field strength, and $\mathbf{B}$ is the magnetic flux density.

the curl of (1.3), using the vector identity $\mathbf{a} \times (\mathbf{b} \times \mathbf{c}) = \mathbf{b} \cdot (\mathbf{a} \cdot \mathbf{c}) - (\mathbf{a} \cdot \mathbf{b})\,\mathbf{c}$, and the relations (1.1) and (1.4)

$$\begin{aligned} \text{curl } (\text{curl } \mathbf{E}) &= -\frac{\partial}{\partial t}\text{curl } \mathbf{B} \,, & (1.5)\\ \text{grad } (\text{div } \mathbf{E}) - \Delta\mathbf{E} &= -\frac{\partial}{\partial t}\left(\epsilon_0\mu_0\frac{\partial \mathbf{E}}{\partial t} + \mu_0\tilde{\mathbf{j}}\right) \,, & (1.6)\\ \text{grad } \frac{\tilde{\rho}}{\epsilon_0} - \Delta\mathbf{E} &= -\epsilon_0\mu_0\frac{\partial^2\mathbf{E}}{\partial t^2} - \frac{\partial}{\partial t}\mu_0\tilde{\mathbf{j}} \,, & (1.7) \end{aligned}$$

the electromagnetic wave equation is derived for the electric field

$$\Delta\mathbf{E} - \frac{1}{\mathrm{c}^2}\frac{\partial^2\mathbf{E}}{\partial t^2} = \text{grad } \frac{\tilde{\rho}}{\epsilon_0} + \frac{\partial}{\partial t}\mu_0\tilde{\mathbf{j}} \,. \quad (1.8)$$

For the interaction of light with semiconductors, some assumptions are made to simplify this problem. (i) In loss-less, neutral, nonconducting, non-magnetic media the free charges and currents are assumed to be zero. (ii) For fast oscillating fields (like it is the case for photons) the gradient of the electric charge density is negligible small compared to the time derivation of the electric current density; see Refs. [1,2]. Thus, the effects of an incident light wave on a system are described by the changes in the electric current density. It can be expanded into a series of multipole moments [17–19]:

$$\tilde{\mathbf{j}} = \tfrac{\partial \mathbf{p}}{\partial t} + \tfrac{1}{\mu_0}\text{curl } \mathbf{m} - \tfrac{\partial}{\partial t}\text{div } \mathbf{q} + \ldots \,. \quad (1.9)$$

Here, $\mathbf{p}$ and $\mathbf{m}$ are the electric- and magnetic-dipole moments, and $\mathbf{q}$ are the electric-quadrupole moments. All are induced by the incoming light field, because it is assumed that no intrinsic moments are present. With these assumptions, the induced electric and magnetic moments become source terms that influence the dynamics of the electric light field itself:

$$\Delta\mathbf{E} - \frac{1}{\mathrm{c}^2}\frac{\partial^2\mathbf{E}}{\partial t^2} = \mu_0\frac{\partial^2\mathbf{p}}{\partial t^2} + \frac{\partial}{\partial t}\text{curl } \mathbf{m} - \mu_0\frac{\partial^2}{\partial t^2}\text{div } \mathbf{q} + \ldots \,. \quad (1.10)$$

It is convenient to introduce the electric displacement field $\mathbf{D}$ and the magnetic field strength $\mathbf{H}$:

$$\begin{aligned} \mathbf{D} &= \epsilon_0\mathbf{E} + \mathbf{P} \,, & (1.11)\\ \mathbf{H} &= \frac{1}{\mu_0}\mathbf{B} - \mathbf{M} \,. & (1.12) \end{aligned}$$

P and **M** are called the polarization and magnetization of the medium, respectively. They correct the electric and magnetic fields by accounting for the induced electric and magnetic moments. They can be understood as the total macroscopic dipole moments originating from the averaged microscopic moments. Then, Maxwell's equations can be rewritten in their macroscopic form (with the assumption that no free carriers and currents are present):

$$\text{curl } \mathbf{E} = -\frac{\partial \mathbf{B}}{\partial t} , \tag{1.13}$$

$$\text{curl } \mathbf{H} = \frac{\partial \mathbf{D}}{\partial t} , \tag{1.14}$$

and the wave equation becomes

$$\Delta \mathbf{E} - \frac{1}{\mathrm{c}^2}\frac{\partial^2 \mathbf{E}}{\partial t^2} = \mu_0 \frac{\partial^2 \mathbf{P}}{\partial t^2} + \frac{\partial}{\partial t}\text{curl } \mathbf{M} . \tag{1.15}$$

1.1.2 Polarization and Susceptibility

The optical harmonic generation is an effect that emerges quickly during the discussion of the polarization **P**. In general, it is assumed to be expandable into a power series of the incoming electric field $\mathbf{E}^{\omega}$ [2]:

$$\frac{1}{\epsilon_0}\mathbf{P} = \chi^{(1)}\mathbf{E}^{\omega} + \chi^{(2)}\mathbf{E}^{\omega}\mathbf{E}^{\omega} + \chi^{(3)}\mathbf{E}^{\omega}\mathbf{E}^{\omega}\mathbf{E}^{\omega} + ... , \tag{1.16}$$

where $\chi^{(i)}$ are the i-th order susceptibilities describing the optical properties of the system. Their magnitude decreases quickly with increasing order, i.e., high-order effects are relevant for intense light fields. The ansatz of a plane monochromatic wave already demonstrates that the nonlinear source terms generate optical harmonic light waves of frequency $n\omega$ ($n \in \mathbb{N}$):

$$\mathbf{E}^{\omega}(\mathbf{r}, t) = \mathbf{E}' \exp^{\mathrm{i}(\mathbf{kr}-\omega t)} + \text{c.c.} \tag{1.17}$$

Here, **k** is the light wave vector, ω the frequency of the light wave (later, a superscript will indicate the corresponding frequency: $\mathbf{k}^{\omega}$), **r** is the position, and t the time. Thus, the second term in Eq. (1.16) becomes

$$\frac{1}{\epsilon_0}\mathbf{P}^{(2)} = \chi^{(2)}\mathbf{E}'\mathbf{E}'^{*} + \left(\chi^{(2)}\mathbf{E}'^{2} \exp^{\mathrm{i}(2\mathbf{kr}-2\omega t)} + \text{c.c.}\right) . \tag{1.18}$$

[2] For a discussion of the situation, when the series in Eq. (1.16) does not converge, see, e.g., Ref. [1] Chap. 6.

The terms in brackets depending on 2ω are responsible for the second harmonic generation. The first term describes the effect called optical rectification, which is not discussed here; for a discussion see, e.g., Refs. [1–3]. The third harmonic generation can be shown to originate from $\mathbf{P}^{(3)}$, accordingly. Thus, studying the SHG or THG yields information on the second or third order susceptibility, respectively. In the following, $\mathbf{P}^{(2)}$ is discussed exemplarily in more detail.

Often it is instructive to modify the optical properties of the studied system by external perturbations, e.g., static electric or magnetic fields, stress, etc. In these cases it is convenient to separate the susceptibility into a crystallographic part, the natural response of the crystal, and a part, that is induced by the external perturbation. The second order polarization can then be written as

$$\mathbf{P} = \epsilon_0(\chi^{\text{cryst}} + \chi^{\text{ind}})\mathbf{E}^{\omega}\mathbf{E}^{\omega}. \tag{1.19}$$

In first order, a linear dependence on the perturbation may be extracted from the induced susceptibility, e.g., for a static electric field $\mathbf{E}_0$:

$$\frac{1}{\epsilon_0}\mathbf{P} = \chi^{\text{cryst}}\mathbf{E}^{\omega}\mathbf{E}^{\omega} + \chi^{\text{ind}\prime}\mathbf{E}^{\omega}\mathbf{E}^{\omega}\mathbf{E}_0. \tag{1.20}$$

In more general cases, the dependences on the external perturbations cannot be extracted easily from the susceptibility anymore, and the induced contributions become:

$$\mathbf{P}^{\text{ind}} = \epsilon_0\chi^{\text{ind}}(\mathbf{B}_0, \mathbf{E}_0)\mathbf{E}^{\omega}\mathbf{E}^{\omega}, \tag{1.21}$$

where the nonlinear optical susceptibility $\chi^{\text{ind}}(\mathbf{B}_0, \mathbf{E}_0)$ accounts for phenomena induced by static magnetic and electric fields.

Is the energy of the outgoing light wave in resonance with an excited crystal state, e.g., the second harmonic is in resonance with the exciton energy $\mathcal{E}_{\text{exc}}$, the electric-quadrupole (EQ) and magnetic-dipole (MD) contributions may become important, and have to be taken into account as well. In such cases, it is convenient to consider an effective polarization depending on the resonance energy, which sums up all contributions (for a detailed description of this concept see Ref. [20]):

$$\mathbf{P}_{\text{eff}}(\mathcal{E}_{\text{exc}}) = \epsilon_0\chi(\mathcal{E}_{\text{exc}}, \mathbf{k}_{\text{exc}})\mathbf{E}^{\omega}\mathbf{E}^{\omega}, \tag{1.22}$$

where the nonlinear optical susceptibility $\chi(\mathcal{E}_{\text{exc}}, \mathbf{k}_{\text{exc}})$ describes spatial-dispersion phenomena including EQ and MD contributions. $\mathbf{k}_{\text{exc}} = 2n\mathbf{k}^{\omega}$ is the exciton wave vector, where n is the refractive index at the fundamental energy $\hbar\omega$, and $\mathbf{k}^{\omega}$ is the wave vector of the incoming light.

In some cases, multiple mechanisms are induced by the same perturbation. Then their susceptibilities have to be summed up to account for interferences among them:

$$\mathbf{P} = \epsilon_0(\chi^{\text{cryst}} + \chi^{\text{ind}}_{\text{mechanism A}} + \chi^{\text{ind}}_{\text{mechanism B}})\mathbf{E}^{\omega}\mathbf{E}^{\omega}. \tag{1.23}$$

1.1.3 Polarization Anisotropies

The experimental study of the emitted harmonic light polarization reveals the properties of the just discussed polarization of the medium. According to Neumann's principle "the symmetry of a physical phenomenon is at least as high as the crystallographic symmetry", it is possible to predict these properties to a certain extent from the space group of the crystal; see, e.g., Refs. [1, 2, 21, 22]. Group theoretical considerations allow to foresee zero and non-zero elements of a susceptibility, and to deduce linear dependences between them. As a consequence, the emitted harmonic light polarizations in Eq. (1.16) show distinct angular distributions, which can be modeled due to the group theoretical predictions. In Sec. 5.1 the algorithm, which is used to model such rotational polarization dependences, is given and discussed. These rotational anisotropies give comprehensive information on the symmetry of the involved nonlinear susceptibilities and underlying processes. Thus they help to distinguish nonlinear optical mechanisms of different nature, which is especially important when more than one mechanism may be involved.

1.1.4 Quantum Mechanical Picture

The introduced susceptibilities describe the optical properties of the material, which are determined by its transition matrix elements. In quantum mechanics the interaction of a system with a light field can be described by the minimal coupling $\mathbf{p} \rightarrow \mathbf{p} - q\mathbf{A}$ and $\mathrm{i}\hbar\frac{\partial}{\partial t} \rightarrow \mathrm{i}\hbar\frac{\partial}{\partial t} - qU$ in the Schrödinger's equation; see, e.g., Refs. [1, 2, 19, 23–25]. This leads to the interaction hamiltonian:

$$\mathbf{H}^{\text{int}} = \sum_i -\frac{q\mathbf{pA}}{m} - \frac{q\mathbf{Ap}}{m} + \frac{q^2\mathbf{A}^2}{2m} + qU \tag{1.24}$$

m and q are the particle's masses and charges. The sum is carried out over all interacting particles. The vector potential $\mathbf{A}$ and the scalar potential U describe the light wave. Note, that Eq. (1.24) does not consider relativistic corrections, i.e., the interaction with the spin remains disregarded.

Choosing the radiation gauge div$\mathbf{A} = 0$ and $U = 0$, the interaction Hamilton simplifies to; compare, e.g., with Refs. [24, 25]:

$$\mathbf{H}^{\text{int}} = \sum_i -\frac{2q\mathbf{pA}}{m} + \frac{q^2\mathbf{A}^2}{2m} \tag{1.25}$$

If the solutions of $|\Psi_i\rangle$ of the Schrödinger equation $\mathrm{i}\hbar\frac{\partial}{\partial t}|\Psi\rangle = \mathbf{H}|\Psi\rangle$ including the interactions in Eq. (1.25) are known, the expectation value of the polarization at 2ω is given by

$$\left\langle \mathbf{P}^{2\omega} \right\rangle = \langle\Psi| \mathbf{P}^{2\omega} |\Psi\rangle . \tag{1.26}$$

The full polarization $\mathbf{P}^{2\omega}$ is given by the electric- and magnetic-dipole, and higher order momenta operators. In calculations, the choice of the momentum operator determines the outgoing transition, e.g., calculating the expectation value of the ED operator will yield the susceptibility that describes microscopic processes in which the emission is via an ED transition. In the following the superscript is neglected $\mathbf{P}^{2\omega} = \mathbf{P}$.

Approximated solutions $|\Psi\rangle = \left|\Psi^{(0)}\right\rangle + \lambda\left|\Psi^{(1)}\right\rangle + \lambda^2\left|\Psi^{(2)}\right\rangle + ...$ can be obtained by perturbation theory. It is assumed that $\lambda \ll 1$, and that the series converges quickly. $\left|\Psi^{(0)}\right\rangle$ are the solutions of the unperturbed system $\mathbf{H}^0$ without time dependence, i.e., $\left|\Psi^{(0)}\right\rangle$ are the eigenstates of the crystal ($\left\langle \Psi_l^{(0)} \middle| \Psi_m^{(0)} \right\rangle = \delta_{lm}$ and $\left\langle \Psi_l^{(0)} \middle| \mathbf{H}^0 \middle| \Psi_m^{(0)} \right\rangle = \mathcal{E}_m\delta_{lm}$). In time-dependent perturbation theory, the time-dependent solutions are constructed from the solutions of the unperturbed system:

$$|\Psi(t)\rangle = \sum_n b_n(t)\mathrm{e}^{-\frac{\mathrm{i}\mathcal{E}_n t}{\hbar}} \left|\Psi_n^{(0)}\right\rangle \tag{1.27}$$

$$\Rightarrow \mathrm{i}\hbar\frac{\mathrm{d}}{\mathrm{d}t}b_n(t) = \sum_k \mathrm{e}^{-\frac{\mathrm{i}(\mathcal{E}_n-\mathcal{E}_k)t}{\hbar}} \left\langle \Psi_n^{(0)} \right| \lambda\mathbf{H}^{\text{int}} \left| \Psi_k^{(0)} \right\rangle b_k(t) , \tag{1.28}$$

$$\text{assuming } b_n(t) = b_n^{(0)}(t) + \lambda^1 b_n^{(1)}(t) + \lambda^2 b_n^{(2)}(t) + ... \text{ and } b_n^{(0)}(t) = b_n^{(0)} \tag{1.29}$$

$$\Rightarrow \mathrm{i}\hbar\frac{\mathrm{d}}{\mathrm{d}t}b_n^{(i)}(t) = \sum_k \mathrm{e}^{-\frac{\mathrm{i}(\mathcal{E}_n-\mathcal{E}_k)t}{\hbar}} \left\langle \Psi_n^{(0)} \right| \mathbf{H}^{\text{int}} \left| \Psi_k^{(0)} \right\rangle b_k^{(i-1)}(t) \tag{1.30}$$

This recurrence yields in first order:

$$b_n^{(1)}(t) = \frac{1}{\mathrm{i}\hbar}\int_0^{t'} \mathrm{d}t' \mathrm{e}^{-\frac{\mathrm{i}(\mathcal{E}_n-\mathcal{E}_i)}{t}} \left\langle \Psi_n^{(0)} \right| \mathbf{H}^{\text{int}} \left| \Psi_i^{(0)} \right\rangle \tag{1.31}$$

Thus, the first order correction is linear in the transition matrix elements determined by the perturbation. It follows from the recurrence that the n-th order correction

will be proportional to the n-th order in the incoming field. Further, the n-th order correction to the wave function can be written as:

$$\left|\Psi^{(n)}\right\rangle = \sum_i b_i^{(n)} \left|\Psi_i^{(0)}\right\rangle \ . \tag{1.32}$$

The expectation value of $\mathbf{P}$ becomes up to second order in perturbation theory:

$$\begin{aligned}
\langle \mathbf{P} \rangle &= \left\langle \Psi^{(0)} \right| \mathbf{P} \left| \Psi^{(0)} \right\rangle && (1.33)\\
&+ \left\langle \Psi^{(0)} \right| \mathbf{P} \left| \Psi^{(1)} \right\rangle + \left\langle \Psi^{(1)} \right| \mathbf{P} \left| \Psi^{(0)} \right\rangle && (1.34)\\
&+ \left\langle \Psi^{(1)} \right| \mathbf{P} \left| \Psi^{(1)} \right\rangle + \left\langle \Psi^{(0)} \right| \mathbf{P} \left| \Psi^{(2)} \right\rangle + \left\langle \Psi^{(2)} \right| \mathbf{P} \left| \Psi^{(0)} \right\rangle && (1.35)\\
&+ \left\langle \Psi^{(1)} \right| \mathbf{P} \left| \Psi^{(2)} \right\rangle + \left\langle \Psi^{(2)} \right| \mathbf{P} \left| \Psi^{(1)} \right\rangle + \left\langle \Psi^{(2)} \right| \mathbf{P} \left| \Psi^{(2)} \right\rangle \ . && (1.36)
\end{aligned}$$

The terms can be sorted according to their order in the perturbation of the incoming field; see for example Refs. [1,7]. Consequently, e.g., the 2-nd order polarization $P^{(2)}$, i.e., the contribution quadratic in the electric field, is obtained by

$$\left\langle \mathbf{P}^{(2)} \right\rangle = \left\langle \Psi^{(0)} \right| \mathbf{P} \left| \Psi^{(2)} \right\rangle + \left\langle \Psi^{(1)} \right| \mathbf{P} \left| \Psi^{(1)} \right\rangle + \left\langle \Psi^{(2)} \right| \mathbf{P} \left| \Psi^{(0)} \right\rangle \ , \tag{1.37}$$

and the respective susceptibility can be calculated according to

$$\chi^{(i)} = \frac{P^{(i)}}{\left(\mathbf{E}^{\omega}\right)^i}, \tag{1.38}$$

where $P^{(i)} \propto \left\langle \mathbf{P}^{(2)} \right\rangle$. The terms in Eq. (1.37) describe different processes of which the first one will be of interest. It describes the process of a two-photon excitation of a state with higher energy than the ground state and a respective one-photon emission.

The excitation processes are governed by the transition matrix elements $\langle n| \mathbf{H}^{\mathrm{int}} |i\rangle$ induced by the incoming light field. For the vector potential $\mathbf{A}$, the following ansatz is valid:

$$\mathbf{A}(\mathbf{r}, t) = \sum_k \mathbf{A}_k \mathrm{e}^{-\mathrm{i}\omega_k t + \mathrm{i}\mathbf{kr}} + \mathbf{A}_k \mathrm{e}^{+\mathrm{i}\omega_k t - \mathrm{i}\mathbf{kr}} \ . \tag{1.39}$$

The linear term $-\frac{2q\mathbf{pA}}{m}$ in Eq. (1.25) is responsible for the transitions between the crystal states. The term quadratic in the vector potential is neglected for the following discussion, although it can be of interest occasionally, e.g., for the description of diamagnetism. In the present work the wave length $\lambda = \frac{2\pi}{k}$ is large compared to

the lattice constant a and the dimensions of the crystal, and the Euler function can be approximated by its first Taylor polynomials:

$$\mathrm{e}^{\pm \mathrm{i}\mathbf{kr}} = 1 \pm \mathrm{i}\mathbf{kr} - \frac{1}{2}(\mathbf{kr})^2 + \mathcal{O}\left(\mathbf{k}^3\right) \tag{1.40}$$

The + and − describe the emission and absorption of photons with frequency ω_k, respectively. A multipole expansion up to the second order of the interaction matrix between two states $\langle f|$ and $|g\rangle$ yields:

$$\left\langle f \left| \frac{qA\mathbf{p}\,(1 \pm \mathrm{i}\mathbf{kr})}{m} \right| g \right\rangle \tag{1.41}$$

These matrix elements can be rewritten in a way (see for example Refs. [23, 24]), that the transitions can be classified in accordance with multipole moments:

$$\langle f\,|\mathbf{p}|\,g\rangle \rightarrow \propto \mathbf{r}\text{, electric-dipole transition} \tag{1.42}$$

$$\langle f\,|\mathrm{i}\mathbf{pkr}|\,g\rangle \rightarrow \propto \mathrm{i}\mathbf{kL}\text{, magnetic-dipole transition, and} \tag{1.43}$$

$$\propto \mathbf{kr}^2\text{, electric-quadrupole transition} \tag{1.44}$$

It is readily seen that magnetic-dipole and electric-quadrupole transitions depend linear on $\mathbf{k}$. They originate from the same order of multipole expansion and are of the same order, but much weaker than the electric-dipole transitions. Generally they are assumed to be $\alpha \approx \frac{1}{137}$ times weaker [25].

For the emission process the momentum operators have to replaced by the respective wave vector, e.g., for the emission of second harmonic $\mathbf{k} \longrightarrow 2\mathbf{k}^{\omega}$.

The electric field $\mathbf{E}$ is obtained from the vector potential $\mathbf{A}$ by the relation [23]:

$$\mathbf{E} = -\frac{\partial}{\partial t}\mathbf{A} = \mathrm{i}\sum_k \left(\omega_k \mathbf{A}_k \mathrm{e}^{-\mathrm{i}\omega_k t + \mathrm{i}\mathbf{kr}} + c.c.\right). \tag{1.45}$$

The time origin shall be chosen so that:

$$\mathrm{i}\omega_k \mathbf{A}_k = \frac{\mathbf{E}_k}{2}\,, \tag{1.46}$$

$$\mathrm{i}k\mathbf{A}_k = \frac{\mathbf{B}_k}{2}\,, \tag{1.47}$$

$$\frac{E_k}{B_k} = \frac{\omega_k}{k} = c\,. \tag{1.48}$$

The interaction Hamiltonian $-\frac{2q\mathbf{pA}}{m}$ in Eq. (1.25) can be rewritten for a monochromatic electric field as:

$$\mathbf{V}^{\mathrm{int}} = \frac{\mathrm{i}q\mathbf{pE}}{m\omega}\,. \tag{1.49}$$

1.1.5 Influence of Static Magnetic and Electric Fields

The generation of optical harmonics is a coherent process being very sensitive to the symmetry properties of the system under investigation. Application of external perturbations can be described by a reduction of the crystal symmetry. This directly influences the nonlinear response function χ and may lead to new field induced components. Especially the magnetic field has proven to be a very fruitful source of induced contributions to harmonics generation [12–14, 26, 27].

This section briefly summarizes the strongest effects of static magnetic and electric fields on crystal excitations; for detailed discussions of these perturbations see Refs. [23–25, 28–30]. A perturbation may have two consequences: (i) the energy correction and (ii) the mixing of states.

The treatment of magnetic fields is generally separated into three regimes [28]:

- The weak field regime - $\mathcal{E}_{\mathrm{Ryd}} \gg \hbar\omega_c \Rightarrow \hbar\frac{eB}{\mu\mathcal{E}_{\mathrm{Ryd}}} \ll 1$, the Coulomb energy dominates and the magnetic field can be treated according to perturbation theory.
- The strong field regime - $\mathcal{E}_{\mathrm{Ryd}} \ll \hbar\omega_c \Rightarrow \hbar\frac{eB}{\mu\mathcal{E}_{\mathrm{Ryd}}} \gg 1$, leading to the formation of Landau levels; see e.g., Ref. [26].
- The intermediate field strength is difficult to handle; see, e.g., Ref. [28].

Here, $\mathcal{E}_{\mathrm{Ryd}} = 13.6\ \mathrm{eV}\frac{\mu}{m_0}\frac{1}{\epsilon_r^2}$ is the exciton Rydberg energy, $\epsilon_r = 1 + \chi$ is the relative permittivity, $\hbar\omega_c = \hbar\frac{eB}{\mu}$ is the cyclotron energy, and $\mu = \frac{m_\mathrm{e} m_\mathrm{h}}{m_\mathrm{e}+m_\mathrm{h}}$ the reduced exciton mass. The presented studies fit into the weak field regime, which is therefore assumed to be valid in the following.

The interaction between static electromagnetic fields and particles is summarized in the Lorentz force

$$\mathbf{F} = q\left(\mathbf{E} + \mathbf{v} \times \mathbf{B}\right) \ . \tag{1.50}$$

It describes the forces on a particle with charge q and velocity v.

Diamagnetic Shift

For bound complexes, e.g., excitons, the Lorentz force deforms their relative motion. Phenomenologically this can be understood as a change in the overall angular momentum. This change is proportional and antiparallel to $\mathbf{B}$. Thus, the change in the inherent magnetic dipole moment is proportional to B as well. The energy

of a magnetic moment scales linear with the magnetic field B leading to an overall energy correction quadratic in B:

$$\Delta\mathcal{E}_{\text{dia}} = \alpha_{\text{dia}}\mathbf{B}^2 \ . \tag{1.51}$$

The expressions for the factor α_{dia} can be found in literature, e.g., for ZnO in Ref. [31]. For $1S$ excitons, α_{dia} is proportional to the square of the exciton Bohr radius defined as $a_{\text{B}} = a_{\text{B}}^{\text{hydr}}\epsilon_r\frac{m_0}{\mu}$, with the hydrogen Bohr radius $a_{\text{B}}^{\text{hydr}} \approx 0.53$ Å; see Ref. [28]. More accurately an effective exciton radius can be calculated according to $r_{\text{exc}} = \frac{3n^2-l(l+1)}{2}a_{\text{B}}$. It increases with the main quantum number n, and is further depended on the orbital quantum number l. This directly reflects that states with an higher main quantum number show stronger diamagnetic shifts.

The diamagnetic shift is present for all exciton states [31]. On the one hand, it is not strong enough to be regarded as a direct mixing mechanism. On the other hand, it may enhance the mixing by other mechanisms due to favorable energy shifts.

Zeeman Effect

States that show a non-vanishing magnetic moment for $\mathbf{B} = 0$ couple directly to an applied magnetic field. There are two types of perturbations, that can be distinguished in case the spin-orbit interaction is small, for a detailed discussion of the Hamiltonian in wurzite structures see Refs. [31, 32]. The spin Zeeman effect describes the coupling of the magnetic field to the magnetic moment caused by the electron or hole spin:

$$\Delta\mathcal{E}_{\text{spin Zee}} \ = \ \pm\frac{1}{2}g\mu_{\text{B}}B \tag{1.52}$$

This perturbation mixes different spin states with the same orbital function by the perturbation $(\sigma\mathbf{B})$, where σ is a Pauli matrix. The electron and hole g-factors $(g = g_{\text{e}} + g_{\text{h}})$ are taken from literature, e.g., for ZnO see Ref. [49]. The orbital Zeeman effect describes the coupling of the magnetic field to the magnetic moment caused by the angular momentum of the envelope of the exciton:

$$\Delta\mathcal{E}_{\text{orb Zee}} = \pm g_{\text{orb}}\mu_{\text{B}}B \tag{1.53}$$

It mixes different orbital functions for exciton states having nonzero envelope orbital momentum L, e.g., P excitons with $l = 1$, by the perturbation $\propto (\mathbf{LB})$. The expressions for the orbital g-factor can be found in literature, e.g., for ZnO in Ref. [31].

The magnetic field is of even parity and yields non-zero matrix elements solely for states of same parity.

A detailed discussion of the Zeeman eigenvalues and eigenfunction can be found in Refs. [31,32].

Magneto-Stark Effect on Excitons

Excitons with non-vanishing crystal momentum $\hbar\mathbf{k}$ exhibit in magnetic fields an energy correction

$$\Delta\mathcal{E} \;=\; r_{\mathrm{exc}} e E_{\mathrm{eff}} \tag{1.54}$$

proportional to an effective electric field, see Ref. [33, 34],

$$\mathbf{E}_{\mathrm{eff}} = \frac{\hbar}{M_{\mathrm{exc}}} \left[\mathbf{k}_{\mathrm{exc}} \times \mathbf{B}\right] \;. \tag{1.55}$$

Here, $M_{\mathrm{exc}} = m_{\mathrm{e}} + m_{\mathrm{h}}$ denotes the exciton translation mass. This effect stems from oppositely directed Lorentz forces acting on electron and hole with opposite electric charge. The respective perturbation of the exciton wave function is equivalent to the effect of the effective electric field $\mathbf{E}_{\mathrm{eff}}$ on the exciton at rest.

Stark Effect

An electronic state of non-vanishing electric dipole moment $\mathbf{p} = q\mathbf{r}$ couples directly to a static electric field $\mathbf{E}$ [23, 30]. This effect is called the Stark effect, and described in quantum mechanics via the perturbation:

$$\mathbf{H}^{\mathrm{Stark}} \;=\; \mathbf{pE} \;. \tag{1.56}$$

$$\tag{1.57}$$

The electric dipole moment $\mathbf{p}$ is calculated by the position operator $\mathbf{r}$, which is of odd parity. Hence, only states of opposite parity get mixed by the Stark effect.

1.2 Optical Setup

The main components of the optical setup are a laser system consisting of a seeding laser, a pump laser and an optical parametric oscillator (OPO), a split-coil cryostat, a monochromator, a charge-coupled-device (CCD) camera, numerous optical components, and a computer with respective software. The data of most measurements is collected in an automated process. Therefore, most components are driven and read out by customized measurement routines programmed in LabView. The orientation of the sample and the alignment of lenses and other optics alike are adjusted manually on a regular basis. For the most time, two types of measurements are performed: (i) The investigation of the frequency dependence of the harmonic light intensity for fixed light polarizations. (ii) The angular dependence of light polarizations for fixed frequencies.

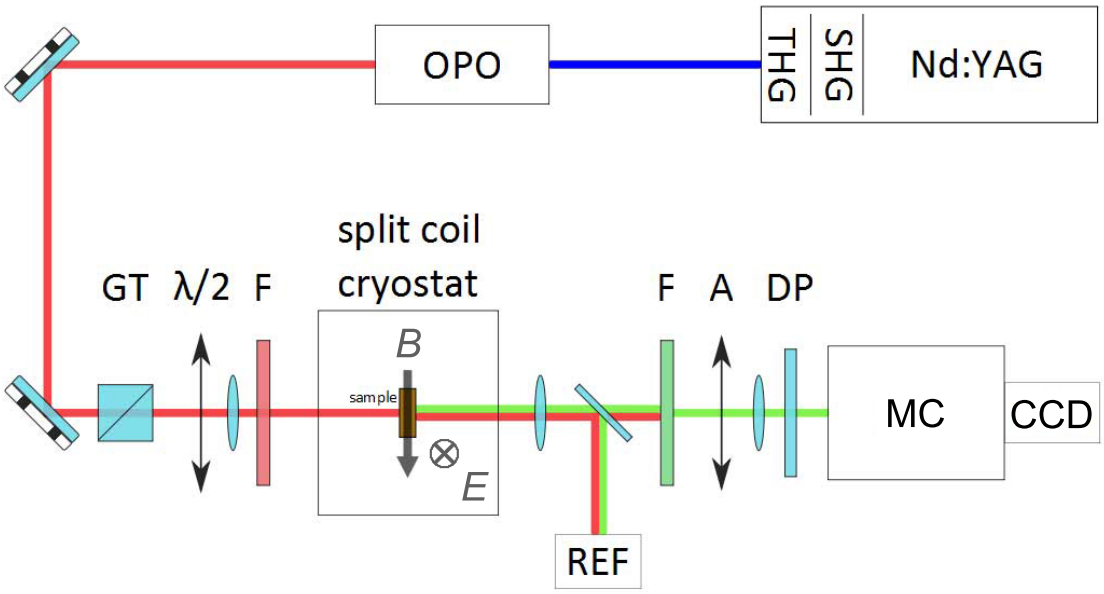

Figure 1.1: Sketch of the optical setup.

Figure 1.1 shows a sketch of the used optical setup. The basis is provided by a Nd-YAG laser system to achieve the required high laser intensities. An OPO built of two Beta-Bariumborat (BBO) crystals allows measurements over a large spectral range ($412 - 2550$ nm). A spit-coil cryostat facilitates low temperatures down to 1.6 K and high magnetic fields up to 10 T at the sample. Electric fields can be applied via electrodes of a custom sample holder. A CCD-camera detects the light intensity, which is spectrally selected by a monochromator. These main components are described in detail in the following subsections.

SHG and THG spectra are obtained by tuning synchronously the fundamental light

energy and the selectively detected harmonic light energy of twice or triple the frequency. The spectra are measured in transmission geometry, i.e., $\mathbf{k}^{\omega} \parallel \mathbf{k}^{2\omega}$. The setup allows the adjustment of numerous parameters: (i) The tuning of the fundamental light intensity allows to check the nonlinear nature of the signals. Further, it needs to be adjusted for each sample to optimize the signal strength without damaging the sample. (ii) The settings of fundamental and harmonic light polarizations allow to match specific selection rules. (iii) The dependences on the magnetic and electric field strengths give insights into the mechanisms involved in the harmonic generation. The magnetic field is applied either in Faraday ($\mathbf{k} \parallel \mathbf{B}$) or in Voigt ($\mathbf{k} \perp \mathbf{B}$) geometry. (iv) The temperature dependence provides additional information on the involved mechanisms. (v) The angle of light incidence can increase the number of addressable tensor components, e.g., for light incident on a tilted sample other components are addressed than for the normal incidence on the surface with a distinct orientation.

Rotational anisotropies are measured in four different geometries:

- $I_{\parallel}^{2\omega} \mapsto \mathbf{E}^{2\omega} \parallel \mathbf{E}^{\omega}$, fundamental and SHG light polarization are chosen to be parallel, and are turned synchronously by the same angle during measurements.
- $I_{\perp}^{2\omega} \mapsto \mathbf{E}^{2\omega} \perp \mathbf{E}^{\omega}$, fundamental and SHG light polarization are turned synchronously, whereas the SHG light polarization is always 90° ahead.
- $I_{\parallel\mathbf{B}}^{2\omega} \mapsto \mathbf{E}^{2\omega} \parallel \mathbf{B}$, SHG light polarization is fixed parallel to the magnetic field direction while the fundamental light polarization is turned around $\mathbf{k}$.
- $I_{\perp\mathbf{B}}^{2\omega} \mapsto \mathbf{E}^{2\omega} \perp \mathbf{B}$, SHG light polarization is fixed perpendicular to the magnetic field direction while the fundamental light polarization is turned around $\mathbf{k}$.

1.2.1 Laser System

To obtain the pump beam a flash lamp filled with xenon pumps neodymium-doped yttrium aluminum garnet (Nd:$Y_3Al_5O_{12}$) rods. At maximum population inversion the Pockels cell enables the back coupling of radiation through an optical resonator and lasing begins [35].

A Pockels cell is an electronically controlled attenuator. It consists of a birefringent KDP crystal and two polarization foils, one before and one behind the crystal. Their polarization planes are twisted by 90°. Variation of the high voltage applied to the crystal allows to turn the polarization plane of light passing through, and the transmission rate can be set between 0 and 100 percent. The electronic control unit is synchronized to the 10 Hz repetition rate of the flash lamp. The pulse energy achieves its maximum in case the Pockels cell opens 15 μs after a pump duration of 200 μs. The control of this delay allows a stepless setting of the pulse energy. Further Nd-YAG rods pumped by the same flash lamp increase the emitted laser

radiation. the temperature of the rods and the flash lamp is precisely stabilized through water cooling. At the fundamental wave length of 1064 nm pulse energies of up to 800 mJ can be gained for pulse durations of $6-8$ ns. The frequency tripling to 355 nm by two consecutive KDP-crystals can reach a conversion rate of up to 30 %. Line widths of < 90 MHz can be achieved in the longitudinal single mode operation with the help of a fibrous coupled injection seeder.

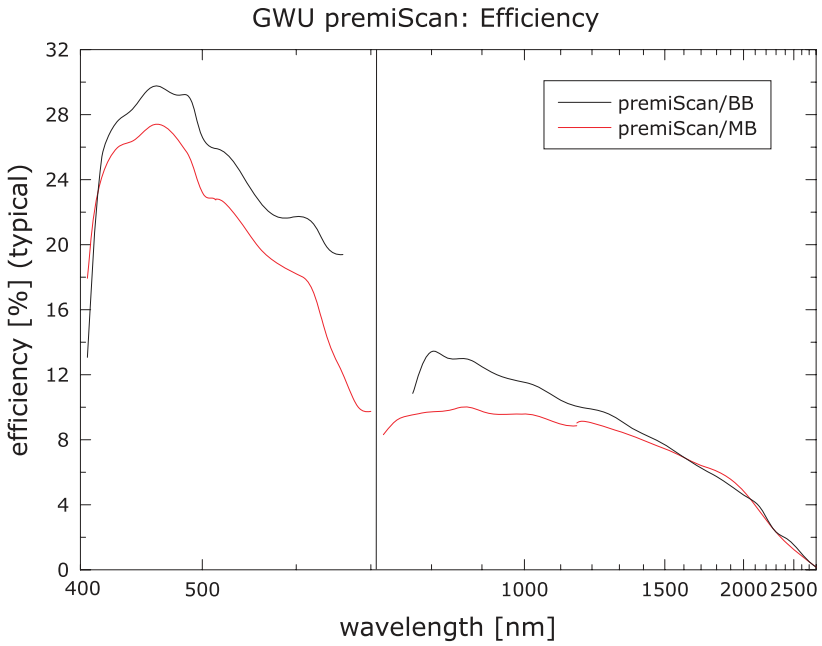

Figure 1.2: Conversion efficiency of the premiScan (versions midband MB and broadband BB) taken from [36].

The used OPO model premiScan (midband version) from GWU is based on two long turnable birefringent type II Beta-Bariumborat (β-BaB_2O_4) crystals from Castech. Type II crystals provide smaller line widths especially in vicinity of the degeneracy compared to type I crystals (compare the line widths of versions MB type II and BB type I shown in Fig. 1.3), that show a more efficient conversion (see Fig. 1.2). Inside the BBO-crystals the pump beam induces the generation signal and idler radiation through a nonlinear parametric process [38]. The radiation with higher energy is conventionally called the signal. Typically the signal beam passes six rounds in the resonator set up in the short configuration (the end mirror does not reflect the idler). The polarizations of signal and idler are perpendicular to each other and their beams are separated by a Glan-Thompson prism.

The generation of both waves fulfills the conservation of energy

$$\omega_P = \omega_S + \omega_I \tag{1.58}$$

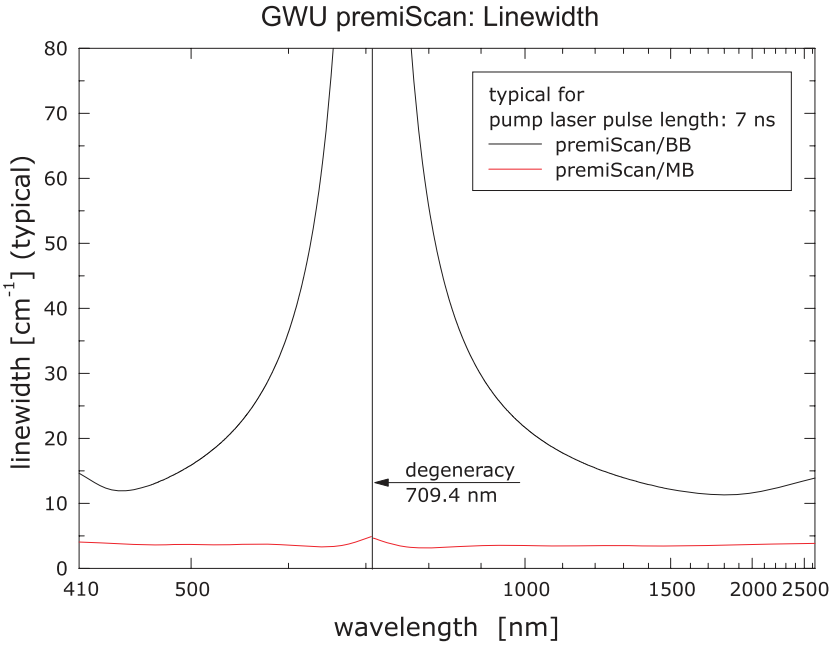

Figure 1.3: Line widths of the premiScan (versions midband MB and broadband BB) taken from [36].

and momentum

$$n_P\omega_P = n_S\omega_S + n_I\omega_I, \tag{1.59}$$

where ω is the angular frequency, n is the refractive index, and the wave vector is $k_i = \frac{n_i\omega_i}{c}$. The emitted wave length is set by means of angle tunning, which allows spectroscopic studies over a broad spectral range: the red crystal allows to tune the range of $514 - 1145$ nm, whereas the blue crystal covers $412 - 514$ nm (signal) and $1145 - 2550$ nm (idler) (see Fig. 1.4). Both crystals differ only in their orientation with respect to the resonator axis.

The large vertical divergence ($3 - 8$ mrad) of the signal and convergence (8 mrad) of the idler are adjusted to the weak horizontal beam divergence (< 0.5 mrad) by a cylindric lens with a large focal length (700 mm).

Note, that their are two major advantages of an OPO based ns laser system: (i) The efficiency is large, and the spectral dependence is flat compared to, e.g., a fs system. (ii) For pulse widths typically > 1 ns, the waves can be considered essentially monochromatic [3].

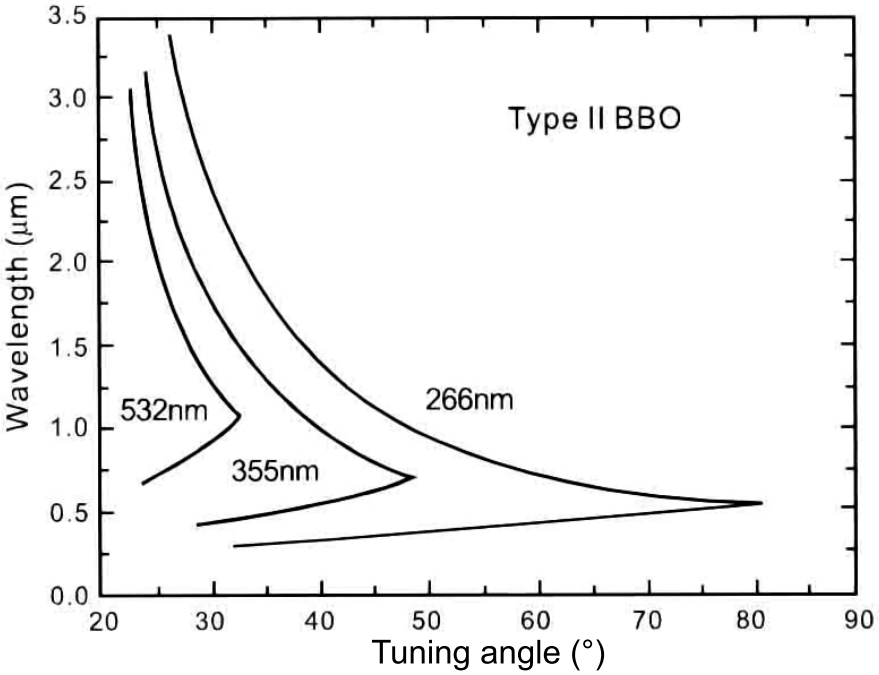

Figure 1.4: Reachable wave lengths in a BBO crystal via angle tuning for different pump waves taken from [37].

1.2.2 Cryostat

The Spectromag from Oxford Instruments is built of three main components: a nitrogen shield, a helium tank, and a VTI (Variable Temperature Inset). All parts are isolated by vacuum ($\sim 10^{-7}$ bar). The N_2 shield reduces the He consumption and prevents thermal bridges. The combination of a needle valve controlling the connection between He tank and VTI, and an electric heater allows to set the sample temperature between 4.2 and 300 K. Temperatures down to 1.6 K can be achieved by under-inflation. The superconducting split-coils can generate magnetic fields up to 11 T. Four windows allow measurements in Faraday ($\mathbf{k} \parallel \mathbf{B}$) and in Voigt ($\mathbf{k} \perp \mathbf{B}$) geometry.

1.2.3 Analyzing Optics

A $\frac{\lambda}{2}$-plate mounted on a electronic rotation stage (polarizer) sets the linear polarization plane of the fundamental light wave. biconvex lenses focus the fundamental beam on the sample. Selected color filters (Tab. 1.1) in front of the sample suppress accidentally generated harmonics from lenses/mirrors. Further filters behind the sample block the transmitted fundamental light (Tab. 1.2). A polarization foil/Glan-Thompson prism mounted on a rotation stage selects the detected harmonics light

Filter / Thickness [mm]	Block [nm]	Pass [nm]
Si/1	673 – 1032	1346 – 2064
RG850/3	500 – 838	1000 – 1676
OG590/3	305 – 550	610 – 1100
GG385/3	206 – 356	412 – 712

Table 1.1: Filter in front of the sample.

Filter / Thickness [mm]	Pass [nm]	Block [nm]
RG9/3	730 – 1025	1460 – 2050
KG2/2	500 – 800	1000 – 1600
BG39/3	340 – 636	680 – 1272
UG11/1	269 – 378	538 – 756
UG5/1	230 – 330	460 – 660

Table 1.2: Filter behind the sample.

polarization (analyzer). A depolarizer partly compensates the polarization dependent efficiency of the monochromator (see Fig. 1.5). Lenses project the emitted light on the entrance slit of the monochromator.

1.2.4 Detection System

Inside the Jobin Yvon HR460 a collimator projects this focused light on turnable and switchable blazed gratings. A collector focuses the spectrally widened light on the CCD chip. Two holographic gratings are mounted. Their efficiencies are shown in Fig. 1.5. The grating 53018 is optimized for a central wave length of 400 nm and has a density of 1800 lines/mm. The grating 53028 is optimized for a central wave length of 750 nm with a density of 1200 lines/mm.

The Pixis256E from Acton is an air and Peltier cooled charge-coupled-device (CCD) camera [40]. A photo active media creates charge carriers, which are transported to a signal amplifier by moving potential traps on the analogy of a shift register. The amplifier transforms the charge into a voltage. After several rounds the whole 256×1024 pixel array is read out and digitalized. A working temperature of -70 °C reduces the dark current and a vacuum atmosphere protects against contamination. The camera is sensitive to light in the spectral region $250 - 1050$ nm.

Various corrections of the signal are necessary to ensure the comparability of different measurements performed under different conditions. Intensities recorded by the camera are corrected for the efficiency curves of the CDD chip and the monochromator directly during the measurement. Further, a reference signal, which intensity is about ~ 1 % of the transmitted laser beam, is recorded by an energy meter. Two energy meters were used: the head QE12LP-S-M8-D0 with the respective monitor

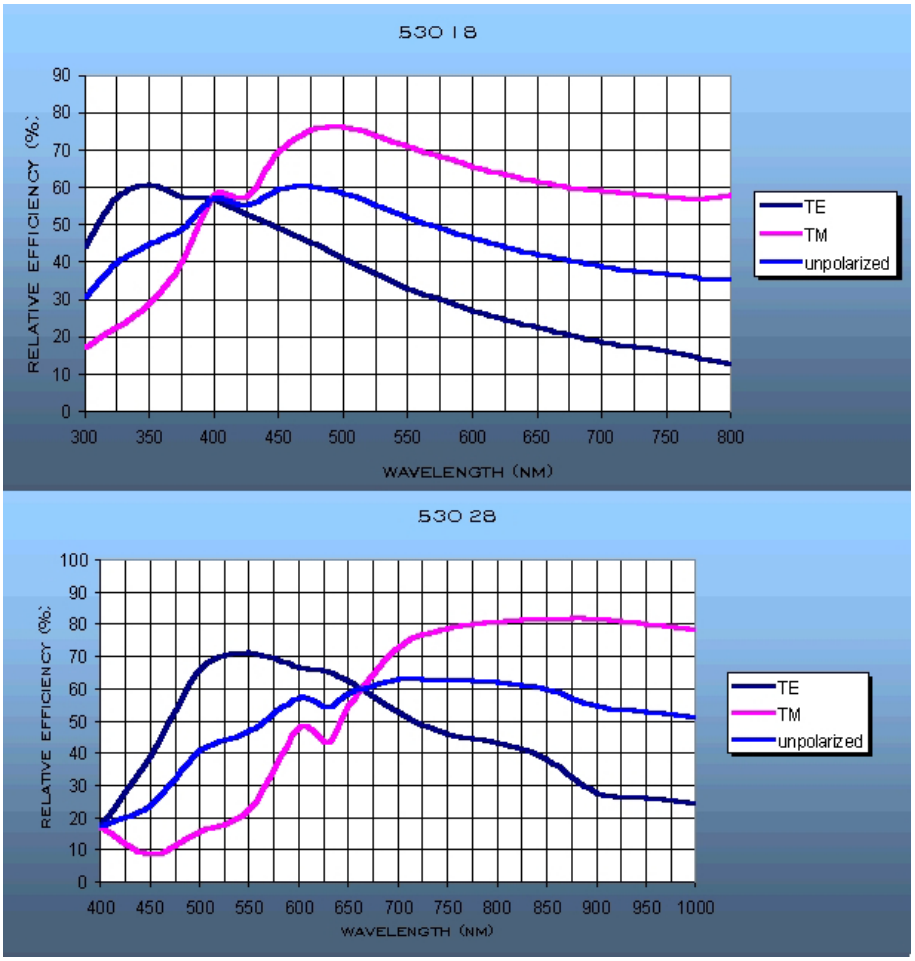

Figure 1.5: Efficiency of the gratings used in the monochromator taken from [39].

from Maestro and the head RjP-375 in combination with the monitor Rm-6600 from LaserProbe Inc. The normalization on the square (for SHG) and the cube (for THG) of the reference accounts for temporal variations and different laser settings.

1.2.5 Custom Sample Holder

Figure 1.7 shows technical drawings and a photograph of the custom sample holder. It was designed for the Oxford Spectromag to apply electric fields **E** perpendicular and simultaneously to the magnetic field **B** of the split-coil. It is made from nylon and brass. The basis made from nylon rods and plates is insulating and insensitive to large temperature variations. The brazen poles are radiused and polished spherical segments wired to an external connector. The distance between the poles can be set by three adjustable springs.

The application of static electric fields to ZnO samples has shown to be very chal-

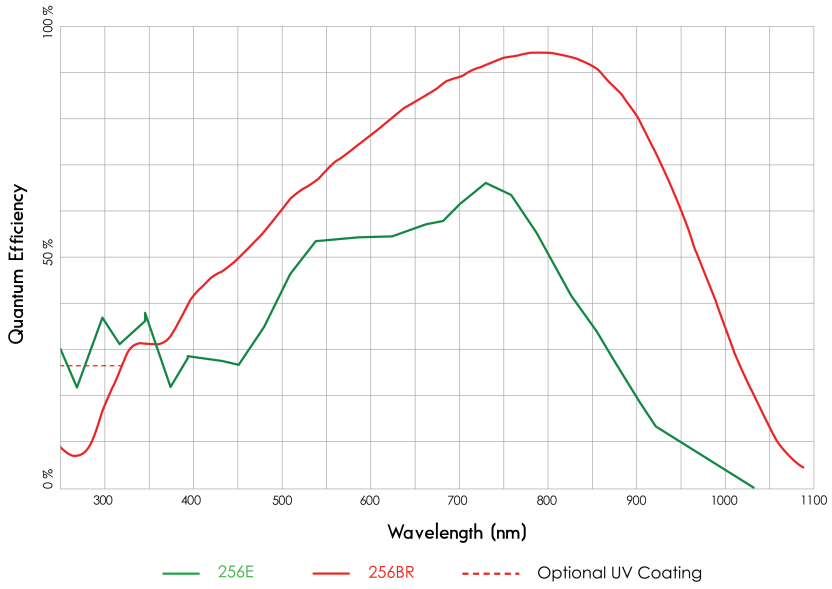

Figure 1.6: Quantum efficiency of the CCD camera chip taken from [40].

lenging. Other attempts than the above described custom sample holder failed to be applicable for different reasons. In case, the sample was put in-between copper plates, and the contact was achieved by the gravitational forces, the contact was unstable and, thus, insufficient to obtain reproducible results. Further, the direct wiring of copper cables to the sample by conductive silver or soldering showed to be unpractical, because it led to unwanted side effects, e.g., damaging the sample, creating conductive pathways through the sample holder, or insufficient accessibility of the sample surface.

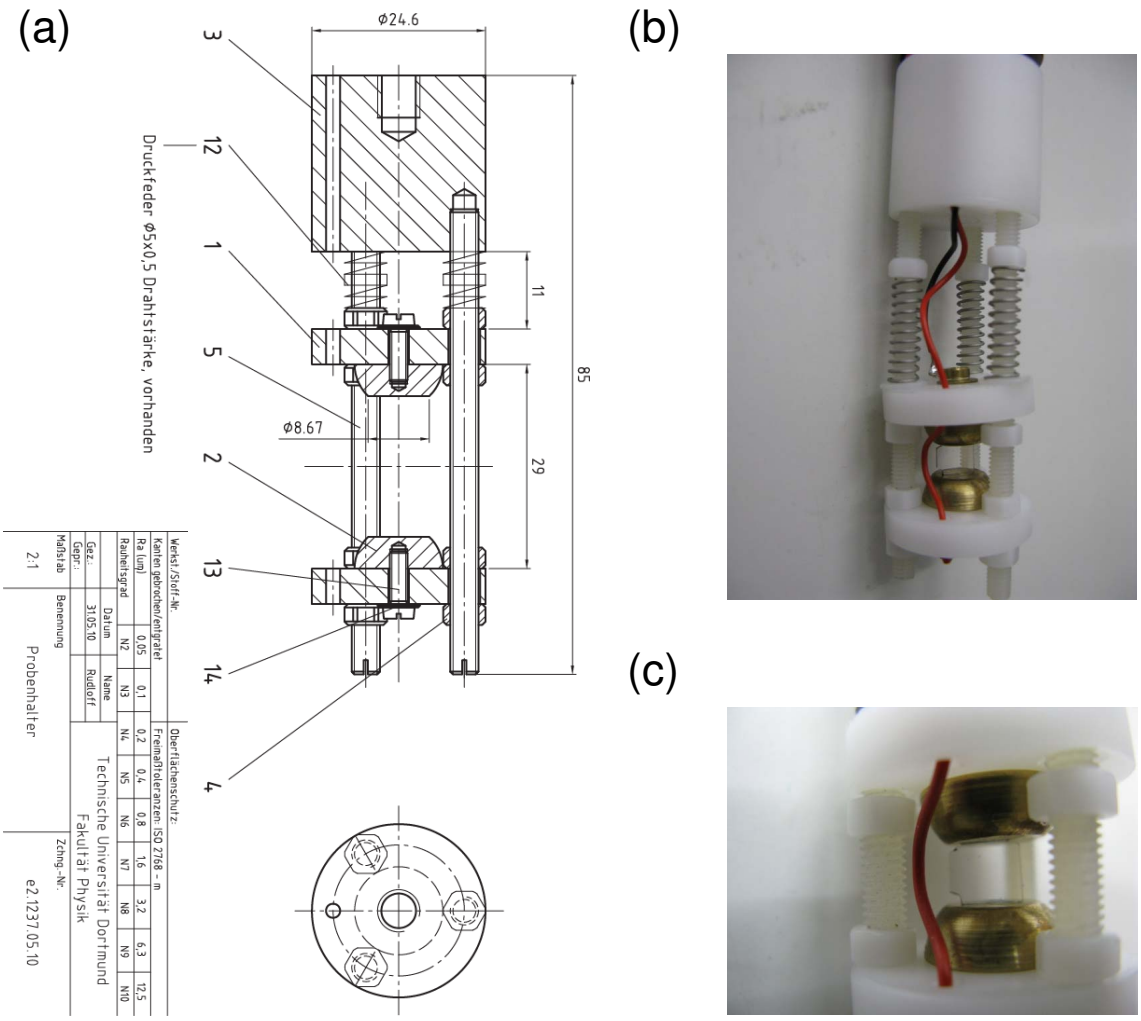

Figure 1.7: (a) Technical drawing of the custom sample holder designed for the application of electric fields. (b,c) Photographs showing a ZnO sample mounted inside the custom sample holder.

2 Second Harmonic Generation of Exciton-Polaritons in ZnO

ZnO is widely used in every day life. Huge amounts of ZnO, mainly in form of white powder, are processed every year as additive in various products. ZnO is involved in the production of many common goods, e.g., plastics, cements, ceramics, lubricants, medical and sun cremes. Further, ZnO is of great importance for sciences and technologies. It is a large direct band-gap semiconductor with large exciton binding energies, which is favorable for, e.g., solar cells, TFT LCDs, and LEDs. Other major advantages of ZnO are the potentially low production costs due to simple and advanced growing methods. Recent interest is fueled by the availability of ZnO crystals of very high quality, which is necessary to investigate its potential for efficient high temperature exciton-based semiconductor lasers of low threshold. For more and detailed information on ZnO see the review by Özgur [41] and references therein. An early attempt to detect SHG signals in the spectral region of the C-exciton in ZnO and the $1S$ excitons in CuCl was undertaken in Refs. [42, 43].

2.1 Band Structure and Electronic Configuration

In the majority of cases, ZnO crystals are grown in the hexagonal wurtzite structure, which is the thermodynamically stable phase at ambient conditions [41, 44, 45]. Its lattice is built on two intertwined Zinc and Oxide hexagonal-close-packed sublattices so that each atom is tetrahedrally surrounded by four atoms of the other kind; an arrangement being typical for the covalent sp^3 hybridization. Each unit cell contains two Zn^{2+} and two O^{2-} ions. Figure 2.1 (a) illustrates the wurtzite crystal and typical tetrahedrons within. Typical lattice constants of ZnO are $a_0 = 3.25$ Å (edge of hexagon) and $c_0 = 5.21$ Å (along z-axis) [46].

The electronic structure of wurtzite ZnO is shown in Fig. 2.1 (b). As a consequence of the large fraction of ionic bonding, the valence band is primarily formed from $2p$ orbitals of O^{2-} ions and the conduction band is primarily formed from $4s$ orbitals of Zn^{2+} ions. The band gap is about 3.437 eV at low temperatures [44, 47]. The hexagonal crystal field splits the $2p$-levels into two subbands of Γ_5 and Γ_1 symmetry. Taking into account spin wave functions and consequently the spin-orbit interaction gives rise to further splittings into three spin degenerated valence band states ($\Gamma_1 \oplus$

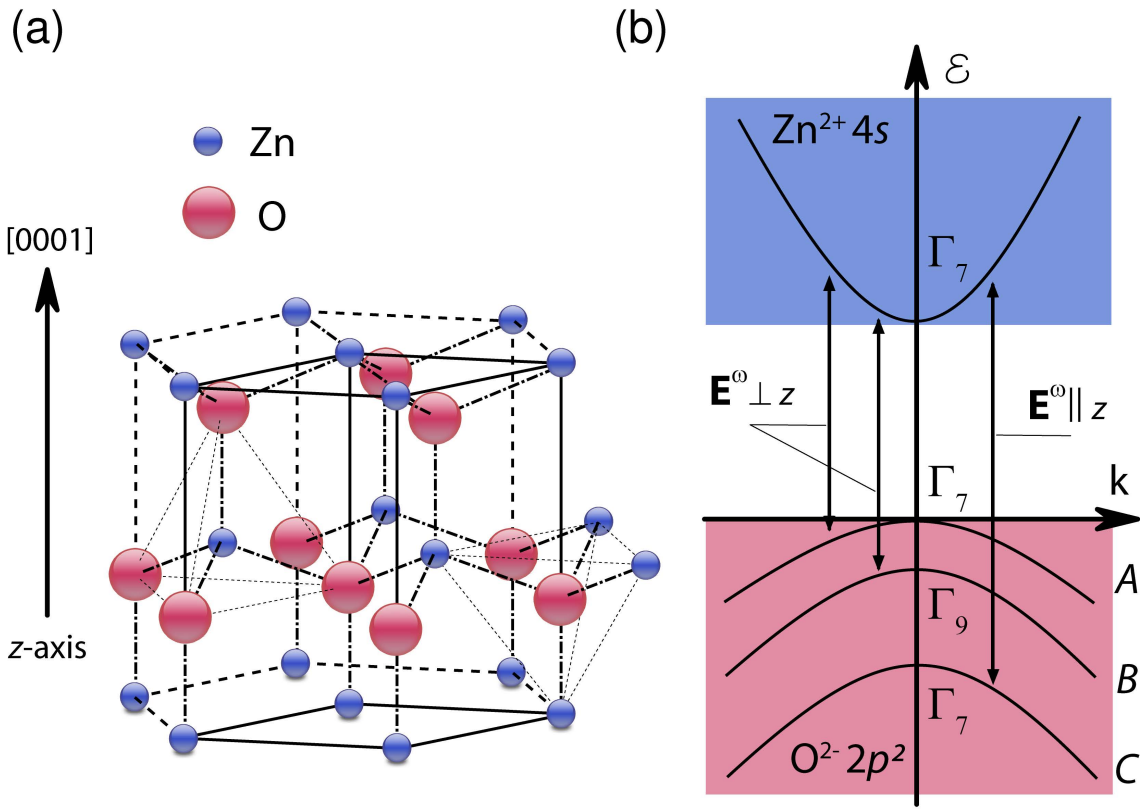

Figure 2.1: (a) Uniaxial crystal structure of wurtzite ZnO. The hexagonal crystal axis is chosen to be the z-axis ([0001] $\parallel$ **z**), in literature it is sometimes also labeled as c-axis . (b) Electronic structure of wurtzite ZnO near the Γ point ($k = 0$). One photon transitions are allowed from A and B valence bands to the lowest conduction band for $\mathbf{E}^{\omega} \perp \mathbf{z}$. Respective transitions from the C valence band are strongest for $\mathbf{E}^{\omega} \parallel \mathbf{z}$.

$\Gamma_5) \oplus \Gamma_7 = \Gamma_7 \oplus \Gamma_9 \oplus \Gamma_7$. But in contrast to the usual order A (Γ_9), B (Γ_7), and C (Γ_7) in wurtzite semiconductors, ZnO has an inverted valence band ordering A (Γ_7), B (Γ_9), and C (Γ_7) due to its negative spin-orbit coupling coefficients originating from the repulsion of the close lying $3d$-orbitals of the Zn ions [44].

Optical transitions from the two upper valence bands A (Γ_7) and B (Γ_9), both having almost entirely Γ_5 character, to the conduction band (Γ_7) obey in principle the same selection rules, because the spin-orbit coupling in ZnO is small and the resulting admixture of the $|z\rangle$ character (Γ_1) to the Bloch wave functions of the A (Γ_7) valence band is small $\left(\frac{\Delta_{\text{spin-orbit}}}{\Delta_{\text{crystal-field}}}\right)^2 \approx \left(\frac{5-6\text{ meV}}{50\text{meV}}\right)^2 \approx 0.01$ [48, 49]. These transitions are electric-dipole allowed for $\mathbf{E}^{\omega} \perp \mathbf{z}$ (Γ_5), where $\mathbf{E}^{\omega}$ is the electric field of the fundamental light wave. In contrast, transitions from the lowest valence band C (Γ_7) to the conduction band (Γ_7) are electric-dipole allowed for $\mathbf{E}^{\omega} \parallel \mathbf{z}$ (Γ_1); see Fig. 2.1 (b).

Three exciton series are formed in ZnO by a Γ_7 electron and a hole from one of

the A (Γ_7), B (Γ_9), or C (Γ_7) bands. It determines the labeling of the exciton as A-,B-, or C-exciton, respectively. These excitons have approximately the same binding energy of $\simeq$ 60 meV and a Bohr radius of $a_\mathrm{B} \simeq 1.8$ nm. The exciton symmetries result from the direct product of the envelope function symmetry and the symmetry of conduction and valence bands Bloch states; see, e.g., Ref. [31] for details. The energies of the resulting one-photon allowed and forbidden states, in ZnO called ortho- and paraexciton, are split by the short-range exchange interaction [30]. For the S-symmetry excitons of the A- and B-series, the strong one-photon-allowed orthoexciton states have Γ_5 symmetry. They are twofold spin-degenerate and polarized perpendicular to the z-axis. For the C-series the strong one-photon-allowed orthoexcitons posses Γ_1 symmetry and are polarized parallel to the z-axis. As a result, for light propagating along the z-axis ($\mathbf{k} \parallel \mathbf{z}$) both Γ_5 excitons are transverse and form polaritons (see Sec. 2.2), while the Γ_1 exciton is longitudinal and cannot be excited. For light propagating perpendicular to the z-axis ($\mathbf{k} \perp \mathbf{z}$), one of the Γ_5 exciton states is transverse and another is longitudinal, while the Γ_1 exciton is transverse. The energies of the longitudinal excitons are shifted to higher energies by the long-range exchange interaction [30].

2.2 Exciton-Polaritons

Strong light-matter interaction in ZnO leads to the formation of coupled exciton-photon states called exciton-polaritons, i.e., states with strong oscillator strength and solutions of the light field cannot be treated separately [30]. The interaction of transverse excitons with photons leads to the formation of lower (LPB) and upper (UPB) polariton branches. Their symmetries depend strongly on the direction of light propagation. In ZnO their dispersion relations are obtained from the condition $\epsilon_\perp(\omega, \mathbf{k}) = (kc/\omega)^2$ for Γ_5 excitons and $\epsilon_\parallel(\omega, \mathbf{k}) = (kc/\omega)^2$ for Γ_1 excitons [50]. $\epsilon_\perp$ and $\epsilon_\parallel$ are dielectric functions for the electric field of light polarized perpendicular and parallel to the z-axis, respectively. They include contributions of exciton resonances with energies close to $\hbar\omega$. The energy of the UPB at $k = 0$ coincides with the energies of the longitudinal excitons determined from $\epsilon_{\perp,\parallel}(\omega, k = 0) = 0$, while the energies of the LPB at $k \to \infty$ coincide with the energies of the transverse excitons. If $\mathbf{k}$ is not parallel or perpendicular to the crystal z-axis, polaritons form so called mixed-mode or extraordinary polaritons [44, 50–52].

The $1S$ exciton-polariton-dispersion relations were studied in detail by two-photon absorption and three-photon-difference frequency generation by Fiebig [52] and Wrzesinski [50]. Fiebig considered the $1S$, $2S$ excitons and two background oscillators to model his experimental results, whereas Wrzesinski included $2S$ states and all higher oscillators in one background oscillator. Their results are summed up in the Appendix 5 in Table 5.1. Figure 2.2 shows the $1S$ dispersion relations (here given in the Kurosawa form underlining the impact of excitons on the dielectric

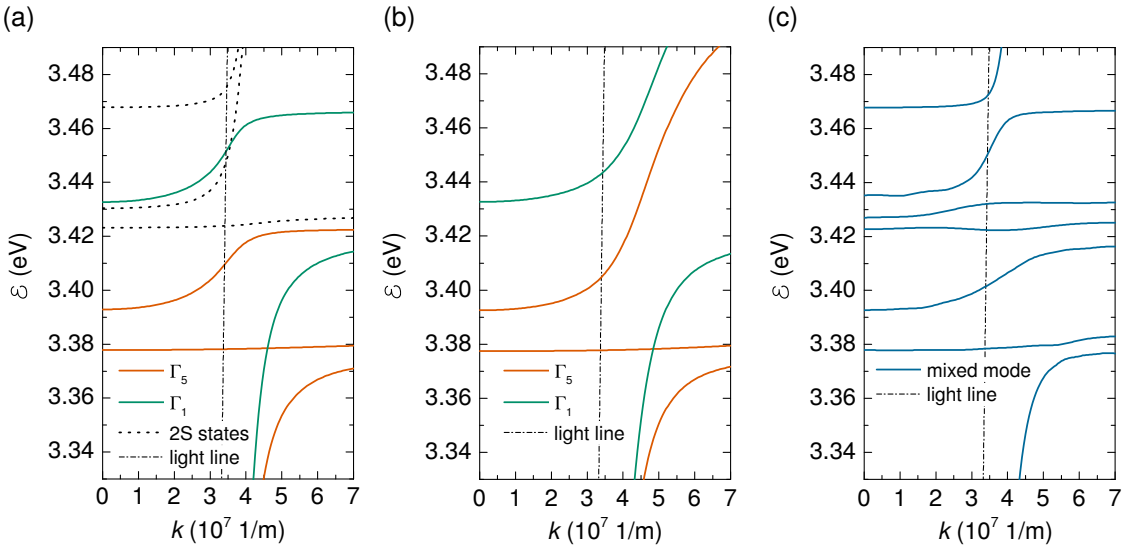

Figure 2.2: The ordinary exciton-polariton-dispersion relations in the region of the $1S$ exciton energies according to (a) [52] and (b) [50]. Γ_5 and Γ_1 denote the pure geometries $\mathbf{E}^\omega \parallel \mathbf{z}$ and $\mathbf{E}^\omega \perp \mathbf{z}$, respectively. (c) The extraordinary exciton-polariton-dispersion relations in the region of the $1S$ exciton energies according to Eq. (2.3) for $\theta = 49°$ based on the results from Ref. [52].

functions)

$$\epsilon_\perp = \frac{\hbar^2 c^2 k^2}{\mathcal{E}_\perp^2} = \epsilon_{\perp,\mathrm{b}} \prod_i \frac{\mathcal{E}_\perp^2 - L_{\mathrm{exc},i}^2}{\mathcal{E}_\perp^2 - T_{\mathrm{exc},i}^2} \text{ and} \tag{2.1}$$

$$\epsilon_\parallel = \frac{\hbar^2 c^2 k^2}{\mathcal{E}_\parallel^2} = \epsilon_{\parallel,\mathrm{b}} \prod_i \frac{\mathcal{E}_\parallel^2 - L_{\mathrm{exc},i}^2}{\mathcal{E}_\parallel^2 - T_{\mathrm{exc},i}^2}, \tag{2.2}$$

according to (a) Fiebig and (b) Wrzesinski. $\mathcal{E}$ denote the polariton energies. ϵ_b describe the dielectric background constants. T and L are the transverse, and respectively longitudinal exciton energies. The light line follows $\mathcal{E} = \hbar c \frac{k}{n}$. The refractive index $n = 1.97$ ([53, 54]) of ZnO is assumed to be constant, because its energy dependence in the region of the fundamental light is small. The consideration of the $2S$ state influences the slope of the $1S$ polariton branches at intersections with the light line. It is seen that the intersection is shifted to lower energies, when the $2S$-states are not accounted for explicitly. Fiebig's results from [52] will be used as a basis for the interpretation of our data.

Fiebig also showed, that for a tilted sample geometry $\angle(\mathbf{k}, \mathbf{z}) \neq 0°$ mixed-mode (mimo) polaritons are observed. They can be modeled separately by shifting the transverse exciton energies to higher energies until the longitudinal-transverse splitting Δ_{L-T} vanishes completely for $\angle(\mathbf{k}, \mathbf{z}) = 90°$. Alternatively the polariton-

dispersion relations can be described by

$$\frac{\hbar^2 c^2 k^2}{\mathcal{E}^2_{\mathrm{mimo}}} = \epsilon_{\mathrm{mimo}} = \frac{\epsilon_{\parallel}\epsilon_{\perp}}{\epsilon_{\parallel}\sin^2\theta + \epsilon_{\perp}\cos^2\theta}. \tag{2.3}$$

Figure 2.2 (c) shows a mixed-mode dispersion for $\theta = 49°$ based on the results of [52]. Further, the investigation of the mixed-mode polariton has underlined that interactions among $1S$ excitons between A and B, and A and C series must be taken into account, while the interaction between B and C series can be neglected.

2.3 Polarization Selection Rules

The uniaxial lattice of wurtzite ZnO belongs to the point group $6mm$ (space group $P6_3mc$) [44, 55] and SHG is allowed in leading order of the electric-dipole (ED) approximation. As first step, only these ED contributions arising from off-resonant and band-gap states at the fundamental $\hbar\omega$ and SHG $2\hbar\omega$ photon energies are considered. The polar hexagonal [0001]-axis is chosen to be parallel to the z-axis of the Cartesian coordinate system. This choice is in accordance with Birss' notation: [0001] $\parallel$ **z**, $[2\bar{1}\bar{1}0] \parallel$ **x**, and $[01\bar{1}0] \parallel$ **y** [22]. The first-order crystallographic SHG polarization $\mathbf{P}^{2\omega}$ is written as

$$P_i^{2\omega} = \epsilon_0 \chi_{ijl}^{\mathrm{cryst}}(\omega, \omega, 2\omega) E_j^{\omega} E_l^{\omega}, \tag{2.4}$$

where i, j, l are Cartesian indices, ϵ_0 is the vacuum permittivity, $\chi_{ijl}^{\mathrm{cryst}}$ are the crystallographic contributions to the optical susceptibility $\chi^{(2)}$, and $E^{\omega}_{j(l)}$ are components of the light field $\mathbf{E}^{\omega}$. In the electric-dipole approximation and absence of external fields, group theory predicts for bulk ZnO the following nonzero components of the crystallographic nonlinear optical susceptibility $\chi_{ijl}^{\mathrm{cryst}}$: $\chi_{xxz} = \chi_{xzx} = \chi_{yyz} = \chi_{yzy}, \chi_{zxx} = \chi_{zyy}$, and χ_{zzz} [1, 21]. The values of the tensor components dependent on energy and vary most strongly for different valence bands.

Figures 2.4 (a) and (b) show typical anisotropies for the parallel ($I_{\parallel}$) and crossed ($I_{\perp}$) configurations in representative measurement geometries; the tensor components are assumed to be real for simplicity. The modeling illustrates that the shapes of anisotropies directly reflect the orientation of the crystal. The clubs in the parallel configuration are always oriented along the z-direction, while the signal is zero perpendicular to the z-direction[1]. In the perpendicular configuration the reversed is valid. The shape of the polarization emission in the parallel configuration can be understood on the basis of symmetry considerations as follows: For $\theta = 0°$, the Γ_1 excitons formed from the C valence band can be excited by two photons

[1] z-direction denotes the projection of the z-axis onto the rotation plane.

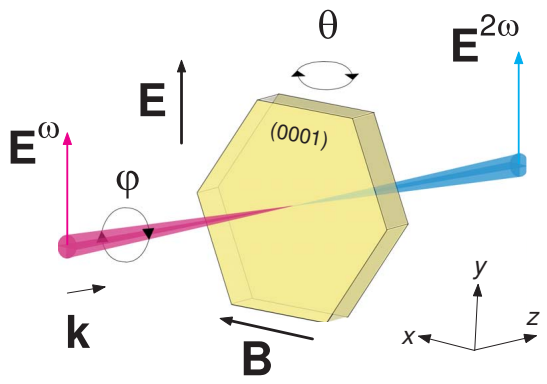

Figure 2.3: A sketch demonstrating the measurement geometry: θ is the tilting angle of the sample around $[0\bar{1}10]$, φ is the turning angle of $\mathbf{E}^{\omega}$ around $\mathbf{k}$. Static electric and magnetic fields are perpendicular to each other and to the propagation direction of the light ($\mathbf{k} \perp \mathbf{E}$, $\mathbf{k} \perp \mathbf{B}$).

($\Gamma_1 \otimes \Gamma_1 = \Gamma_1$) and emit simultaneously one photon (Γ_1). For $\theta = 90°$, excitation ($\Gamma_5 \otimes \Gamma_5 = \Gamma_1 \oplus \Gamma_2 \oplus \Gamma_6$) and emission ($\Gamma_5$) of the same state are not feasible and signals are zero. For intermediate orientations $0° \leq \theta \leq 90°$ the Γ_5 states originating from the A, B valence bands are active for SHG (two photons $\Gamma_1 \otimes \Gamma_5 = \Gamma_5$, one photon Γ_5), as well as the C valence band states. In the perpendicular configuration signals of the C valence band dominate the pattern. For $\theta = 90°$, excitation ($\Gamma_5 \otimes \Gamma_5 = \Gamma_1 \oplus ...$) of the Γ_1 states is possible and the Γ_1 emission is detected. In the configuration $\theta = 0°$, selected excitation ($\Gamma_1 \otimes \Gamma_1 = \Gamma_1$) and detected emission (Γ_5) do not allow the observation of any signal. The other shown model anisotropies can be explained accordingly.

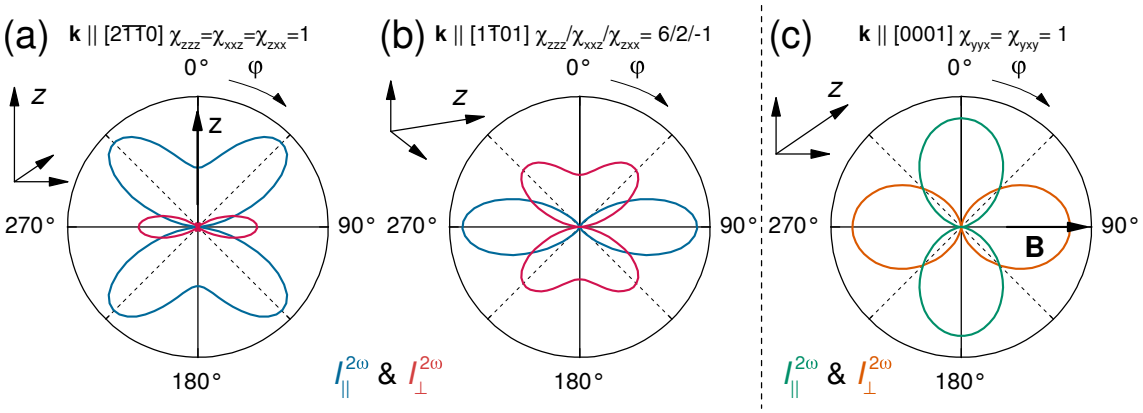

Figure 2.4: Model anisotropies of SHG in ZnO with full C_{6v} symmetry for different geometries and different ratios of the tensor components (only real components are assumed for simplicity). Blue and red lines illustrate the parallel ($I_{\parallel}$) and crossed ($I_{\perp}$) measurement configurations respectively. (a) Crystallographic SHG for $\mathbf{k} \parallel \mathbf{x}$. (b) Crystallographic SHG for $\mathbf{k} \perp \mathbf{x}$, $\mathbf{k} \nparallel \mathbf{z}$, and $\mathbf{k} \nparallel \mathbf{y}$. (c) Blue and red lines illustrate the parallel and crossed measurement configurations respectively. (c) Magnetic field induced SHG for $\mathbf{k} \parallel \mathbf{z}$.

However, the SHG process in a more general case can involve electric-quadrupole (EQ) and magnetic-dipole (MD) contributions which, therefore, have to be taken into account. They become important, especially when the outgoing SHG is in resonance, e.g., with the exciton energy $\mathcal{E}_{\rm exc}$. As second step, higher-order contributions are considered. The incoming fundamental electric field $\mathbf{E}^{\omega}(\mathbf{r},t) = \mathbf{E}^{\omega}\exp[\mathrm{i}(\mathbf{kr}-\omega t)]$ generates an effective polarization inside the semiconductor at the double frequency [20]:

$$P^{2\omega}_{{\rm eff},i}(\mathcal{E}_{\rm exc},\mathbf{k}_{\rm exc}) = \epsilon_0 \chi^{\rm cryst}_{ijl}(\mathcal{E}_{\rm exc},\mathbf{k}_{\rm exc}) E^{\omega}_j E^{\omega}_l, \tag{2.5}$$

where the nonlinear optical susceptibility $\chi^{\rm cryst}_{ijl}(\mathcal{E}_{\rm exc},\mathbf{k}_{\rm exc})$ describes the spatial-dispersion phenomena, i.e., the EQ and MD contributions. $\mathbf{k}_{\rm exc} = 2n\mathbf{k}$ is the exciton-polariton wave vector, n is the refractive index at the fundamental energy $\hbar\omega$, and $\mathbf{k}$ is the wave vector of the incoming light.

A further step includes the influence of external fields on the effective polarization inside ZnO:

$$P^{2\omega}_{{\rm eff},B,E,i}(\mathcal{E}_{\rm exc},\mathbf{k}_{\rm exc},\mathbf{B},\mathbf{E}) = \epsilon_0 \chi^{\rm ind}_{ijl}(\mathcal{E}_{\rm exc},\mathbf{k}_{\rm exc},\mathbf{B},\mathbf{E}) E^{\omega}_j E^{\omega}_l, \tag{2.6}$$

where the nonlinear optical susceptibility $\chi^{\rm ind}_{ijl}(\mathcal{E}_{\rm exc},\mathbf{k}_{\rm exc},\mathbf{B},\mathbf{E})$ accounts for phenomena induced by external magnetic $\mathbf{B}$ and electric $\mathbf{E}$ fields. A group theoretical analysis predicts for external electric or magnetic fields additional nonzero tensor components of the nonlinear optical susceptibility $\chi^{(2)}$; see, e.g., Refs. [21,22]. These become interesting particularly in the geometry $\mathbf{k}^{\omega} \parallel \mathbf{z}$, where crystallographic SHG is forbidden. When the susceptibility depends linearly on the external field, group theoretical considerations provide for $\mathbf{k} \parallel \mathbf{z}$ the following nonzero tensor components: $\chi_{yyx} = \chi_{yxy}$, $\chi_{xxy} = \chi_{xyx}$, $\chi_{yyy} = 2\chi_{xxy} + \chi_{yxx}$, and $\chi_{xxx} = 2\chi_{yyx} + \chi_{xyy}$. Figure 2.4 (c) illustrates the induced SHG polarization anisotropies for $\chi \propto B$, $\mathbf{B} \parallel \mathbf{x}$, and $\mathbf{k} \parallel \mathbf{z}$:

$$I^{2\omega}_{\parallel} \propto \chi_{yyy}\cos^2\varphi, \tag{2.7}$$

$$I^{2\omega}_{\perp} \propto \chi_{yyy}\sin^2\varphi. \tag{2.8}$$

Symmetries of exciton states can be modified by electric and magnetic fields enabling the mixing of states. Later it will be shown that the application of a magnetic or electric field perpendicular to the hexagonal z-axis may reduce symmetries of the exciton states so that the field dependence is nonlinear and the relation either

$\chi_{yyy} = \chi_{yxx} + 2\chi_{xxy}$ or $\chi_{xxx} = 2\chi_{yyx} + \chi_{xyy}$ is violated depending on the orientation of the perturbation:

$$I^{2\omega}_{\perp\mathbf{B}} \propto [\chi_{yyy}\cos^2\varphi + \chi_{yxx}\sin^2\varphi]^2, \tag{2.9}$$
$$I^{2\omega}_{\parallel\mathbf{B}} \propto [\chi_{xxy}\sin\varphi]^2, \tag{2.10}$$
$$I^{2\omega}_{\parallel} \propto \cos^2\varphi[\chi_{yyy}\cos^2\varphi + (\chi_{yxx} + 2\chi_{xxy})\sin^2\varphi]^2, \tag{2.11}$$
$$I^{2\omega}_{\perp} \propto \sin^2\varphi[(\chi_{yyy} - 2\chi_{xxy})\cos^2\varphi + \chi_{yxx}\sin^2\varphi]^2. \tag{2.12}$$

The polarization selection rules for THG ($\chi^{(3)}$) in the configuration $\mathbf{k} \parallel \mathbf{z}$ without external perturbations are rather simple. The one independent tensor component $\chi_{xyxy} = \chi_{yxyx} = \chi_{xxyy} = \chi_{yyxx} = \chi_{xyyx} = \chi_{yxxy}, \chi_{xxxx} = \chi_{yyyy} = 3\chi_{xyxy}$ gives rise to isotropic emission of THG light polarization in the parallel configuration and no THG is seen in the crossed configuration.

2.4 Samples

ID	Thickness (μm)	Orientation	Growing Method	Substrate	Origin
TD1a	500	(0001)	hydrothermal	bulk	TokyoDenpa Co., Ltd.
TD1b	500	(0001)	hydrothermal	bulk	TokyoDenpa Co., Ltd.
TD2_4	500	(0001)	hydrothermal	bulk	TokyoDenpa Co., Ltd.
EN73.2	3000	(0001)	-	bulk	D. Fröhlich (Dortmund)
No13,15,39,...	273-1090	(0001)	MBE	Al_2O_3	C. Meier (Paderborn)
P1199	1.3	(0001)	MBE	GaN(2μm)/saphire	A. Bakin (Braunschweig)
Crys-m	435	$(4\bar{1}3\bar{2})$	hydrothermal	bulk	CrysTec GmbH
Crys-a	284	(1120)	hydrothermal	bulk	CrysTec GmbH

Table 2.1: List of ZnO samples.

Many ZnO samples from various sources grown by different methods were studied. The bulk samples grown hydrothermally by TokyoDenpa (TD) have proven to be the most suitable for the investigation of SHG in ZnO due to their strong signals. Figure 2.5 illustrates that the TD samples show high SHG intensities, and the most pronounced features, while the off-resonant SHG is weak. For the study of electric-field-induced SHG it was necessary to anneal the samples which results in an increase in resistivity; e.g., the sample with label EN73.2 was annealed at 700 °C for 20 hours, and showed an increase of resistivity from 10^6 Ohm to 10^9 Ohm. All further measurements shown in this work were performed on the sample TD1a for the just mentioned reasons, except for the electric field measurements, which were performed on the sample EN73.2 having the highest resistivity. The orientations of the samples TD1a, TD1b, TD2_4, and EN73.2 were checked by Laue diagrams and with a polarization microscope.

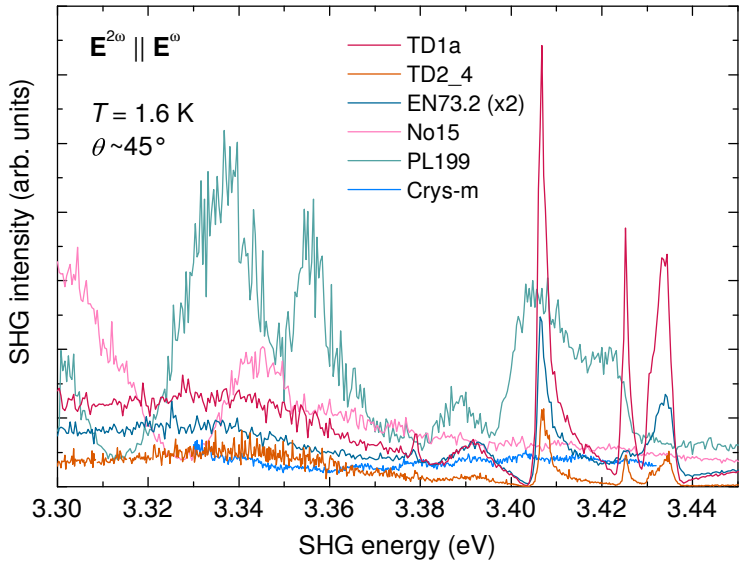

Figure 2.5: Crystallographic spectra of various ZnO samples for $\mathbf{E}^{2\omega} \parallel \mathbf{E}^{\omega}$ in the range of 3.30 eV$\leq \mathcal{E} \leq$ 3.45 eV at $T = 1.6$ K.

2.5 Power Dependence of SHG in ZnO

The nonlinear nature of the observed signals is exemplary shown in Figure 2.6. The crystallographic and induced signals in ZnO show the expected quadratic dependence on the incident light power; compare with Eq. (1.19).

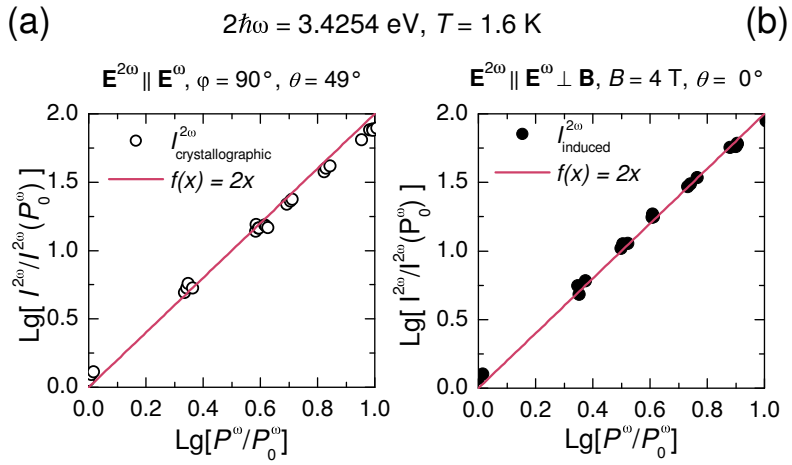

Figure 2.6: Quadratic dependence of the crystallographic (a) and induced (b) SHG light intensity of ZnO at $2\hbar\omega = 3.4254$ eV.

2.6 Crystallographic Contributions to $\chi^{(2)}$

Figure 2.7 (a) shows the crystallographic SHG spectrum of ZnO for $\mathbf{E}^{2\omega} \parallel \mathbf{E}^{\omega}$ and $\varphi = 90°$. The sample is tilted[2] by $\theta = 49°$. In this configuration both the fundamental and harmonic electric-field polarizations lie in the (z, x)-plane. All three nonzero tensor components χ_{xxz}, χ_{zxx}, and χ_{zzz} of χ^{cryst} are addressed. Two-photon excitation is feasible for Γ_1, Γ_2, and Γ_6, and emission visible for Γ_1 and Γ_5. The light line crosses the modeled mixed-mode-polariton-dispersion curves several times in the investigated region. In the following the observed spectral features will be matched with these intersections.

The first feature is observed at 3.3788 eV, which corresponds energetically to the middle $1S(A, B)$ extraordinary polariton branch; see first intersection of the light line with the dispersion curves in Fig. 2.2 (c). They are referred to as A, B branches although being mixed-mode polaritons, because the influence of the C-valence band is small [52]. The relative sharp spectral shape can be understood qualitatively by two arguments: The intersection between the light line and the dispersion curve is almost at a right angle and the damping of the $1S(A)$ exciton is small ≈ 0.1 meV [56]. The second feature around 3.3918 eV lies in the vicinity of the longitudinal $1S_{\text{L}}(B)$ exciton energy. The shape is rather broad and it is not a sharp line like it was the case for the first feature. It appears to stem from the intersection with the upper $1S(A, B)$ extraordinary polariton branch, since its anisotropies show the same pattern as the intersection with the middle A, B extraordinary polariton branch; compare Figs. 2.8 (b) and (c). Qualitative explanations are again given by the relative small angle at which the light line intersects the polariton branch, and the strong $1S(B)$ damping of about 2 meV [56].

Around 3.407 eV a further feature having a high SHG intensity is observed. Its intensity is five times stronger than the peaks linked to the mixed-mode polaritons. It lacks a partner in literature and is therefore referred to as X-line. In a previous work by Kaminski [57], this line was attributed to the upper mixed-mode polariton branch. The following arguments raise doubts about that interpretation: (a) The intensity is much stronger than that for the middle branch. A respective strong oscillator strength indicates that the C valence band is involved in the SHG process. (b) The polarization anisotropies are very similar to those of the $1S(C)$ exciton polariton. But Fiebig [58] has seen that the C valence band has no remarkable influence on the $L - T$ splitting of the B polariton which dominates the attributes of the upper A, B mixed-mode branch. (c) A dependence on the tilting angle θ is expected for the upper $1S(A, B)$ polariton branch, nevertheless it was not observed. (d) The spectral asymmetry of the strong signal seems to originate from interference with another broader SHG signal, which is here linked to the upper $1S(A, B)$ polariton branch. An interference is only expected between signals governed by A, B and

[2]The tilting angle θ is derived by fitting the crystal orientation; see Eq. (5.2).

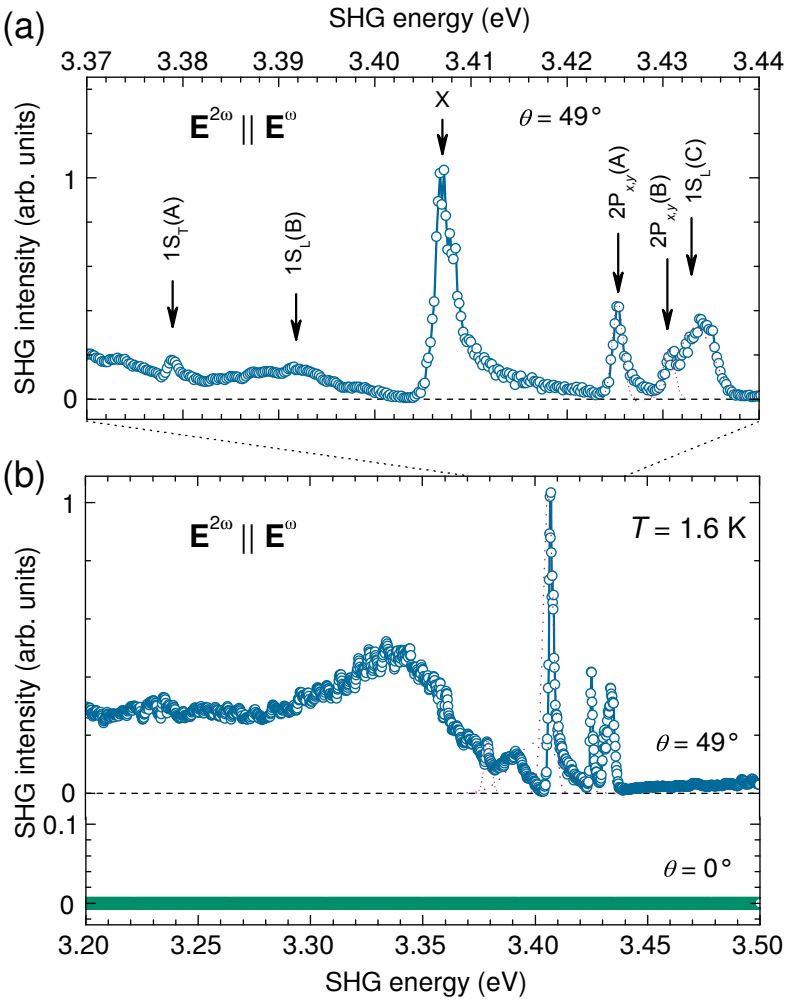

Figure 2.7: Crystallographic SHG spectra of ZnO for $\mathbf{E}^{2\omega} \parallel \mathbf{E}^{\omega}$ and $\varphi = 90°$ (compare with anisotropies in Fig. 2.8) measured at $T = 1.6$ K. (a) Enlargement of the exciton region 3.37-3.44 eV for $\theta = 49°$. Arrows mark exciton energies taken from literature [52]. (b) Wide-range spectra 3.2-3.5 eV for $\theta = 49°$ (blue circles) and 0° (green circles). No SHG is detected for $\mathbf{k} \parallel \mathbf{z}$ ($\theta = 0°$). Red dashed lines are Lorentz curves as guides for the eye.

C valence bands. This asymmetry related to interference is absent for a geometry where signals of the A, B bands are suppressed (analyzer 0° and polarizer 90°). We propose that the X-line belongs to a bound C exciton. Further features are observed for 3.4254 eV and 3.4304 eV, which are linked to the $2P_{x,y}(A)$ and $2P_{x,y}(B)$ excitons. These states will dominate the magnetic field induced signals for normal incidence as it will be shown in following paragraphs. The highest energy feature is seen around 3.4338 eV and is explained by the intersection of the light line with the mixed-mode polariton branch closest to the $1S_L(C)$ exciton energy. It is more intense than the other features linked to intersection points, because the oscillator strength of the $C(\Gamma_1)$ exciton is larger (about 4 times) than that of the $A(\Gamma_5)$ exciton [56]. The broad peak structure can be understood by the large damping of ≈ 2 meV [56]. The

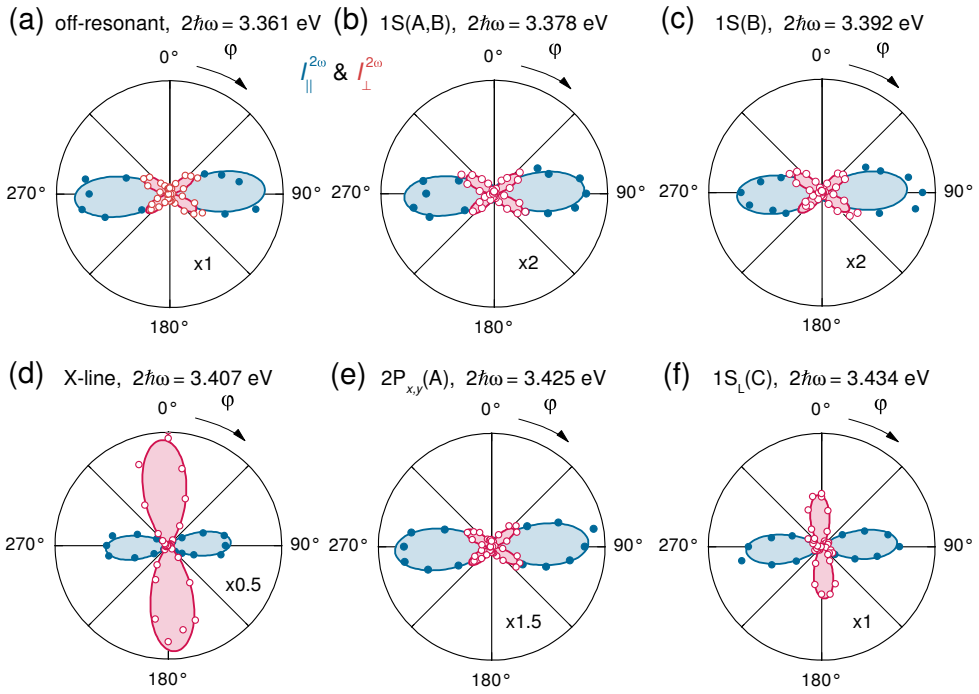

Figure 2.8: Angular distributions of the crystallographic SHG polarization measured at $\theta = 49°$ for different energies. Blue and red circles show the geometries $I_{\parallel}^{2\omega}$ and $I_{\perp}^{2\omega}$, respectively. Lines and shaded areas show best fits according to Eq. (2.4). (a) Off-resonant signals at $2\hbar\omega = 3.361$ eV. (b) Middle $1S(A,B)$ extraordinary polariton branch at $2\hbar\omega = 3.378$ eV. Signals are scaled up by a factor of 2. (c) Upper $1S(A,B)$ extraordinary polariton branch at $2\hbar\omega = 3.392$ eV. Signals are scaled up by a factor of 2. (d) X-line at $2\hbar\omega = 3.407$ eV. Signals are scaled down by a factor of 2. (e) $2P_{x,y}(A)$ exciton line at $2\hbar\omega = 3.425$ eV. Signals are scaled up by a factor of 1.5. (f) Mixed-mode polariton at $2\hbar\omega = 3.434$ eV close to $1S_{\mathrm{L}}(C)$ exciton energy.

intersections for $2\hbar\omega > 3.45$ eV are not observed leading to the conclusion that their attributes are governed by the $2S$ states and their oscillator strengths are too weak. However, around 3.472 eV an additional feature is vaguely perceptible and it may be linked to the intersection with the polariton branch closest to the $2S(C)$ exciton energy.

With the light wave vector $k \approx 3.37 \times 10^7$ 1/m the lowest polariton branch cannot be reached (the light line does not cross the lower polariton branch; see Fig. 2.7). Nevertheless, it can contribute to the off-resonant SHG background at lower energies shown in the wide range spectrum in Fig. 2.7 (b). Its anisotropies, demonstrated in Fig. 2.8 (a), show that the off-resonant SHG at low energies is determined by the A, B valence bands. For $\mathbf{k} \parallel \mathbf{z}$ no SHG is observed; see Fig. 2.7 (c). In this measurement geometry (Fig. 2.3) crystallographic SHG is symmetry forbidden; see Sec. 2.3. This orientation is chosen, because it allows the sole study of the generation of second harmonic induced by external magnetic and electric fields.

2.7 SHG of $1S$ Exciton-Polaritons in Magnetic Fields

Blatter et al. have studied the effects of magnetic fields on the $1S(A,B)$ exciton polaritons in detail in Ref. [59]. They have shown that in this spectral region the diamagnetic shift, pure k-dependent terms, and higher-order contributions are negligible compared to the spin Zeeman effect. The following chapter will discuss how the off-diagonal element in the Hamiltonian due to the spin Zeeman effect can be used to generate SHG of $1S$ paraexcitons and orthoexcitons in ZnO, which would not contribute to SHG without a magnetic field for $\mathbf{k} \parallel \mathbf{z}$.

2.7.1 Theoretical Considerations

The transformation properties of a static magnetic field $\mathbf{B} \perp \mathbf{z}$ are represented by Γ_5 in C_{6v}. In ZnO it couples $A\Gamma_5$ and $A\Gamma_{1,2}$ $1S$ states for the A-series, while for the B-series the $B\Gamma_5$ and $B\Gamma_6$ $1S$ states are coupled ($\Gamma_1 \otimes \Gamma_5 = \Gamma_5$,$\Gamma_2 \otimes \Gamma_5 = \Gamma_5$,$\Gamma_6 \otimes \Gamma_5 = \Gamma_5 \oplus ...$) [59,60]. Coupling only among orthoexcitons or only among paraexcitons would be feasible for $\mathbf{B} \parallel \mathbf{z}$ (Γ_2). In the considered configuration $\mathbf{B} \parallel \mathbf{x}$ the states $A\Gamma_{5y}$ and $A\Gamma_1$, and $B\Gamma_{5y}$ and $B\Gamma_6$ become mixed [59]. The Γ_5 states of the A and B polaritons in ZnO couple and form three joint polariton branches, which is shown in Sec. 2.2. This coupling will be neglected in the following calculations, but included in their discussion afterwards. The mixed states for $\mathbf{B} \parallel \mathbf{x} \perp \mathbf{k}$ can be derived approximately by diagonalizing the 2×2 Hamiltonians

$$\hat{H}^{A}_{\Gamma_{5y}/\Gamma_1} = \begin{pmatrix} \mathcal{E}_{\Gamma_1} & \mu_\mathrm{B} g_\mathrm{exc} B_x/2 \\ \mu_\mathrm{B} g_\mathrm{exc} B_x/2 & \mathcal{E}_{\Gamma_5} \end{pmatrix}, \tag{2.13}$$

$$\hat{H}^{B}_{\Gamma_{5y}/\Gamma_6} = \begin{pmatrix} \mathcal{E}_{\Gamma_6} & \mu_\mathrm{B} g_\mathrm{exc} B_x/2 \\ \mu_\mathrm{B} g_\mathrm{exc} B_x/2 & \mathcal{E}_{\Gamma_5} \end{pmatrix}, \tag{2.14}$$

where $\mathcal{E}_{\Gamma_{1,5,6}}$ are zero-field energies of the respective states. $g_\mathrm{exc} = |g_\mathrm{h}^{\perp} - g_\mathrm{e}^{\perp}|$ is the exciton effective g-factor for $\mathbf{B} \perp \mathbf{z}$. In ZnO the electron and hole g-factors are $g_\mathrm{e}^{\perp} \approx 1.95$, $g_\mathrm{h}^{A\perp} \approx 0.7$, and $g_\mathrm{h}^{B\perp} \approx 0$ [59]. In Ref. [49] $g_\mathrm{h}^{A\perp} \approx 0$ is published, but this difference has no qualitative consequences for the mechanism. As long as the hole and electron g-factors do not compensate each other, para- and orthoexcitons get mixed and can contribute to SHG. The energies of the coupled states in an external magnetic field B_x are given by

$$\mathcal{E}^{A\pm}_{\Gamma_{5y}/\Gamma_1} = \frac{1}{2}\left(\mathcal{E}_{\Gamma_1} + \mathcal{E}_{\Gamma_5} \pm \sqrt{\Delta^2_{1-5} + (\mu_\mathrm{B} g_\mathrm{exc} B_x)^2}\right), \tag{2.15}$$

$$\mathcal{E}^{B\pm}_{\Gamma_{5y}/\Gamma_6} = \frac{1}{2}\left(\mathcal{E}_{\Gamma_6} + \mathcal{E}_{\Gamma_5} \pm \sqrt{\Delta^2_{6-5} + (\mu_\mathrm{B} g_\mathrm{exc} B_x)^2}\right), \tag{2.16}$$

where $\Delta_{X-Y} = |\mathcal{E}_X - \mathcal{E}_Y|$ is the respective energy splitting. $\mathcal{E}_{\Gamma_5}$ are approximated by the respective longitudinal exciton energies $\mathcal{E}_{1S_L}$. The wave functions are obtained by

$$\Psi^A_{\Gamma_{5y}/\Gamma_1} = C_{\Gamma_{5y}}(B_x)\Psi^A_{\Gamma_{5y}} + C_{\Gamma_1}(B_x)\Psi^A_{\Gamma_{1,2}} \tag{2.17}$$

$$\Psi^B_{\Gamma_{5y}/\Gamma_6} = C_{\Gamma_{5y}}(B_x)\Psi^B_{\Gamma_{5y}} + C_{\Gamma_6}(B_x)\Psi^B_{\Gamma_6}\ , \tag{2.18}$$

with coefficients

$$C_{\Gamma_{5y}}(B_x) = \frac{2(\mathcal{E}^{A,B}_{\Gamma_{5y}} - \mathcal{E}^{A,B\pm})}{\sqrt{(\mu_B g_{exc} B_x)^2 + 4(\mathcal{E}^{A,B}_{\Gamma_{5y}} - \mathcal{E}^{A,B\pm})^2}}, \tag{2.19}$$

$$C_{\Gamma_1}(B_x) = -\frac{\mu_B g_{exc} B_x}{\sqrt{(\mu_B g_{exc} B_x)^2 + 4(\mathcal{E}^{A}_{\Gamma_{5y}} - \mathcal{E}^{A\pm})^2}}, \tag{2.20}$$

$$C_{\Gamma_6}(B_x) = -\frac{\mu_B g_{exc} B_x}{\sqrt{(\mu_B g_{exc} B_x)^2 + 4(\mathcal{E}^{B}_{\Gamma_{5y}} - \mathcal{E}^{B\pm})^2}}. \tag{2.21}$$

Figure 2.9 shows the mixing coefficients $C^A_{\Gamma_{5y}}$, $C^A_{\Gamma_1}$, $C^B_{\Gamma_{5y}}$, and $C^B_{\Gamma_6}$ for 0 T$< B <$ 10 T. For a sufficiently strong mixing, SHG will be possible because the Γ_5 part is ED al-

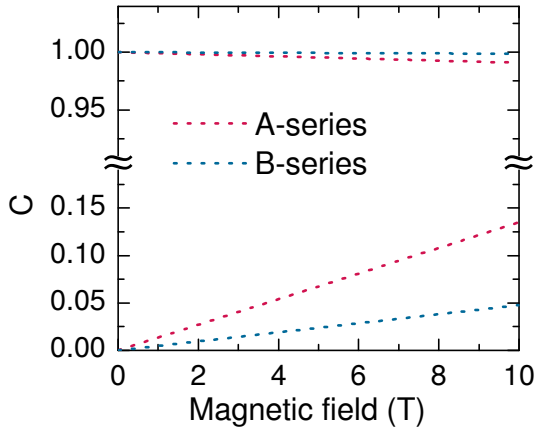

Figure 2.9: Mixing coefficients of the $1S(A,B)$ para- and orthoexcitons in ZnO due to the spin Zeeman effect following Eqs. (2.19)-(2.21).

lowed for one-photon emission, while the Γ_1, or Γ_6 part can be excited in two-photon processes. The magnetic-field-induced nonzero susceptibilities $\chi_{yyy} = \chi_{yxx}$ depend on the product of the mixing coefficients for the A- and B-series, respectively:

$$\chi_{yyy}(\mathcal{E}^{\pm}_{\Gamma_{5y}/\Gamma_{1,6}}, k_{exc}, B_x, 0) \propto C_{\Gamma_5}(B_x)C_{\Gamma_{1,6}}(B_x). \tag{2.22}$$

When the spin Zeeman energy $|\mu_B g_{exc} B_x|$ is much smaller than the zero-field splitting of the respective exciton-polariton states (being the case for the 1S states in ZnO), then the susceptibilities depend linear on B_x, i.e., the SHG intensity follows B^2, and the spatial wurtzite symmetry is not violated. The magnetic field breaks the time reversal symmetry, and the spin is not a good quantum number anymore.

The zero-field splittings $|\mathcal{E}(1S_L(A\Gamma_5)) - \mathcal{E}(1S(A\Gamma_1))| \approx 2.6$ meV for the A-series and $|\mathcal{E}(1S_L(B\Gamma_5)) - \mathcal{E}(1S(B\Gamma_6))| \approx 11.8$ meV for the B-series neglect the coupling between them. This leads qualitatively to stronger SHG for the A-series than for the B-series. In fact, the paraexcitons lie in vicinity of the middle 1S polariton branch. When the intersection of the light-line with the middle polariton branch is assumed for $\mathcal{E}^{A,B}_{\Gamma_{5y}}$ the splittings are about $\Delta^A \approx 4.7$ meV and $\Delta^B \approx 1.1$ meV, and SHG for the B-series is stronger than for the A-series. Experimental results will show that the observed signals for the A-series are in fact stronger, and neglecting the coupling between A and B states is a justified approximation. For more accurate descriptions an advanced theory is needed, which accounts for the coupling between A and B states, and the coupling to the photon field simultaneously.

For the parallel $\mathbf{P}^{2\omega}_{\text{eff}} \parallel \mathbf{E}^{\omega}$ and crossed $\mathbf{P}^{2\omega}_{\text{eff}} \perp \mathbf{E}^{\omega}$ geometries one can predict SHG signals with the same amplitude, and their anisotropies are described by $I^{2\omega}_{\parallel} \propto |\chi_{yyy}|^2 \cos^2\varphi$ and $I^{2\omega}_{\perp} \propto |\chi_{yxx}|^2 \sin^2\varphi$; see Eqs. (2.7) and (2.8). Further, for $\mathbf{B} \parallel \mathbf{x}$ the SHG signal polarized perpendicular to the magnetic field direction $I^{2\omega}_{\perp\mathbf{B}} \propto |\chi_{yyy}|^2$ does not depend on the excitation polarization direction, while the signal polarized parallel to the magnetic field vanishes $I^{2\omega}_{\parallel\mathbf{B}} \propto |\chi_{yxy}|^2 = 0$.

2.7.2 Experimental Results

Figure 2.10 (a) shows three lines in the region of the 1$S(A)$ exciton emerging in magnetic fields $\mathbf{B} \parallel \mathbf{x}$, with $\mathbf{k} \parallel \mathbf{z}$, and $\mathbf{E}^{2\omega/\omega} \parallel \mathbf{y}$. The strongest line at 3.3754 eV corresponds energetically to the degenerated 1$S(A\Gamma_{1,2})$ paraexcitons [50, 58]. Their very small magnetic-field-induced splitting cannot be resolved. The second line at 3.3780 eV is linked to the middle polariton branch of the $\Gamma_5(A, B)$ dispersion, as has been shown in Fig. 2.2 (a). The third and weakest line at 3.3811 eV coincides with the energy of the 1$S(B\Gamma_6)$ paraexciton [58,59]. It is seen for $B > 7$ T, which is apparently the approximate field, where Blattner et al. have seen the B paraexciton in transmission measurements [59]. It is possible that the mixing mechanism is not sufficiently strong in fields < 7 T for the B-series and the induced signals are too weak: Fig. 2.9 shows that the mixing coefficients of the A-series are larger than those of the B-series. The integrated intensities depend quadratically on the field strength; see Fig. 2.13 (a). It is in accordance with the theoretical model given in Eqs. (2.17) and (2.18). The rotational anisotropies given in Fig. 2.10 (c) are well described by $\propto \cos^2\varphi$ for $\mathbf{E}^{2\omega} \parallel \mathbf{E}^{\omega}$ and $\propto \sin^2\varphi$ for $\mathbf{E}^{2\omega} \perp \mathbf{E}^{\omega}$, and both configurations have the same amplitude. Hence, modeling the shapes is possible following the

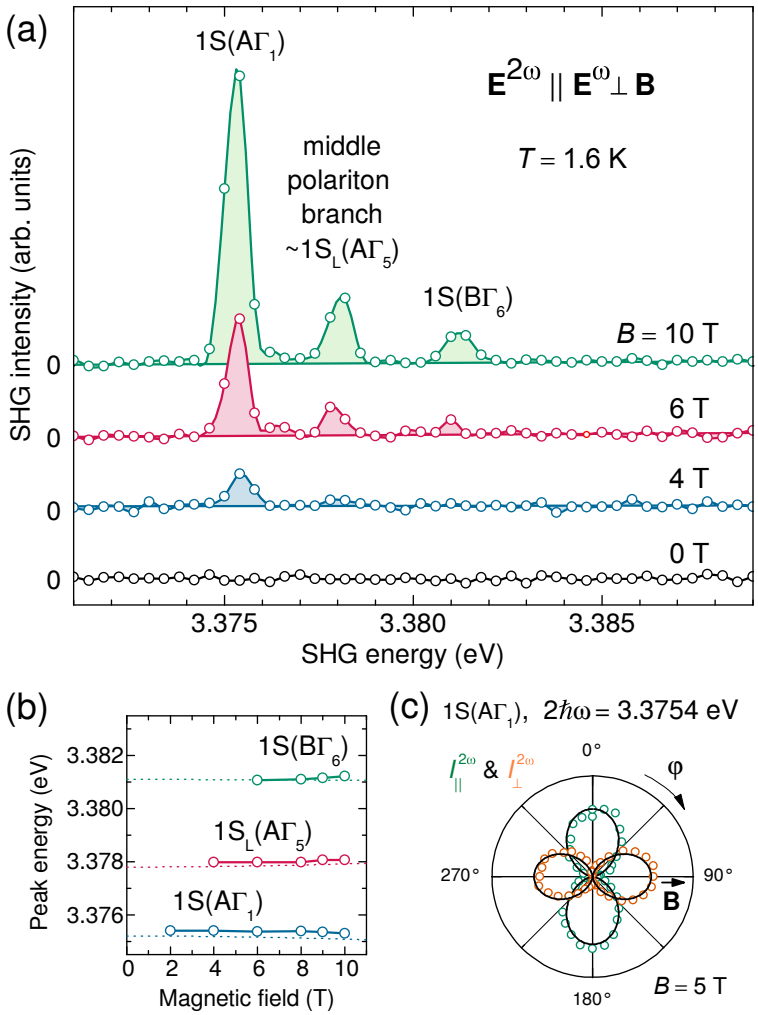

Figure 2.10: (a) Pure magnetic-field-induced SHG signals in vicinity of the $1S(A)$ exciton-polariton for $B = 0$, 4, 6, and 10 T. Measurements were performed for $\mathbf{E}^{2\omega} \parallel \mathbf{E}^{\omega} \perp \mathbf{B}$ at $T = 1.6$ K. (b) Peak energy vs. magnetic field: a magnetic field dependence of the peak energies is not resolved. Dotted lines follow Eqs. (2.15) and (2.16). (c) Rotational polarization anisotropies of the SHG intensity of the strongest line at $B = 5$ T being exemplary for all measured lines and fields. Green circles represent the configuration $\mathbf{E}^{2\omega} \parallel \mathbf{E}^{\omega}$ and orange circles show $\mathbf{E}^{2\omega} \perp \mathbf{E}^{\omega}$. Black lines give fits according to Eqs. (2.7) and (2.8).

predictions in Eqs. (2.7) and (2.8). The emission $I^{2\omega} \parallel \mathbf{x} \parallel \mathbf{B}$ vanishes for all incoming polarizations, whereas the detected signals $I^{2\omega} \parallel \mathbf{y} \perp \mathbf{B}$ are independent of the fundamental polarization. It follows that the emission stems from the Γ_{5y} parts of the wave functions. No emission from the Γ_{5x} is observed and contributions from $A\Gamma_2$ can be excluded. All lines are not expected to shift in magnetic fields, which was indeed observed (see Fig. 2.10 (b)).

The temperature dependence measured at $B = 7$ T shows a rapid decrease for in-

creasing temperature; see Fig. 2.20 (a). Temperature dependencies will be discussed separately in a later section (Sec. 2.10).

The observed magnetic-field-induced lines are fully explained by the mixing of strong one-photon-allowed orthoexcitons and two-photon-allowed paraexcitons. Note, that this allows magnetic-field-induced SHG spectroscopy to measure ortho- and paraexcitons in a single spectroscopic run. This mechanism is also valid for $2S$ states, but as their oscillator strengths are $\sim \frac{1}{2^2}$ smaller, no detectable signals can be expected. Although, it shall be kept in mind in case it is subject to possible enhancement by interference with stronger contributions.

2.8 SHG of $2S/2P$ Exciton-Polaritons in Magnetic Fields

In contrast to the $n = 1$ exciton region of ZnO, the influence of magnetic fields on its $n = 2$ region has not been explored in detail. Investigations of $2P$ magneto-excitons in ZnO are scarce. One example is the work of Dinges et al., who have investigated the Zeeman splitting of the $2P$ exciton states in the Faraday configuration by two photon absorption [61]. Our investigation by SHG spectroscopy in transmission geometry shows that the field-induced mixing of exciton wave functions has a remarkable influence on the nonlinear susceptibility $\chi^{(2)}(\omega, \omega, 2\omega)$ in the $n = 2$ exciton region. Studies of $2P$ excitons without external fields are found, e.g., in Refs. [52,62].

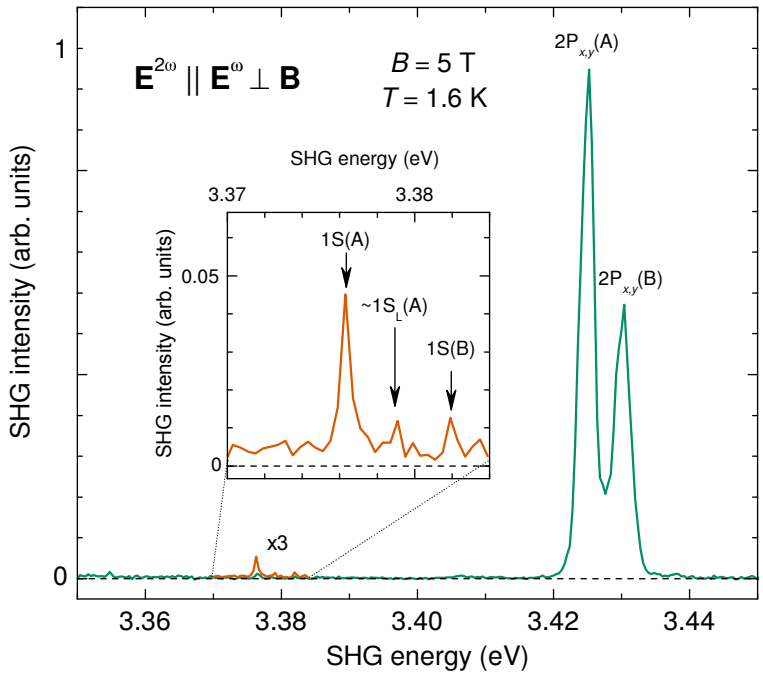

Figure 2.11: Magnetic-field-induced SHG is observed in ZnO in the range of $1S$ and $2P$ excitons. The wide-range spectrum ($3.35 - 3.45$ eV) is measured for $\mathbf{E}^{2\omega} \parallel \mathbf{E}^{\omega} \perp \mathbf{B}$, $B = 5$ T, and $\theta = 0°$ at $T = 1.6$ K. The inset shows the SHG of $1S$ excitons enhanced by a factor of 20. Integration time for data shown by the orange line is tripled compared to data shown by the green line.

Figure 2.11 demonstrates strong-magnetic-field induced SHG signals, which are surprisingly observed in vicinity of the $2S/2P(A, B)$ excitons. In the chosen experimental geometry ($\theta = 0°$), no crystallographic SHG is allowed, but a magnetic field applied perpendicular to the z-axis ($\mathbf{B} \perp \mathbf{k} \parallel \mathbf{z}$) leads to two strong lines. A comparison of the signal strength with the discussed $1S$ lines points out the high efficiency of the underlying mechanisms. The $n = 2$ signals are about 60 times

stronger than those of the $1S$ states, although the absorption of SHG light in the $1S$ range is only $5-7$ times stronger [63]. This behavior is very unexpected, because it differs from the observations in GaAs and CdTe, where the $1S$ exciton line always dominates magnetic-field-induced SHG spectra [12, 13, 26, 64]. In the following the $2S/2P(A, B)$ exciton energy range will be studied, analyzed, and discussed in detail. An early stage of this investigation is discussed in the dissertation by Kaminski [57], where the magneto-Stark effect is proposed as mechanism[3]. In the following, this assumption is verified by new and extensive data, especially in Section 2.9, by the analysis of its interference with a static electric field. Furthermore, the development of a microscopic theory and a thorough analysis of the new results reveal numerous other mechanisms that contribute to $\chi^{(2)}$ in this region. In addition, the temperature dependence of resonant SHG of excitons is shown in Sec. 2.10 to be governed by their damping.

2.8.1 Experimental Results

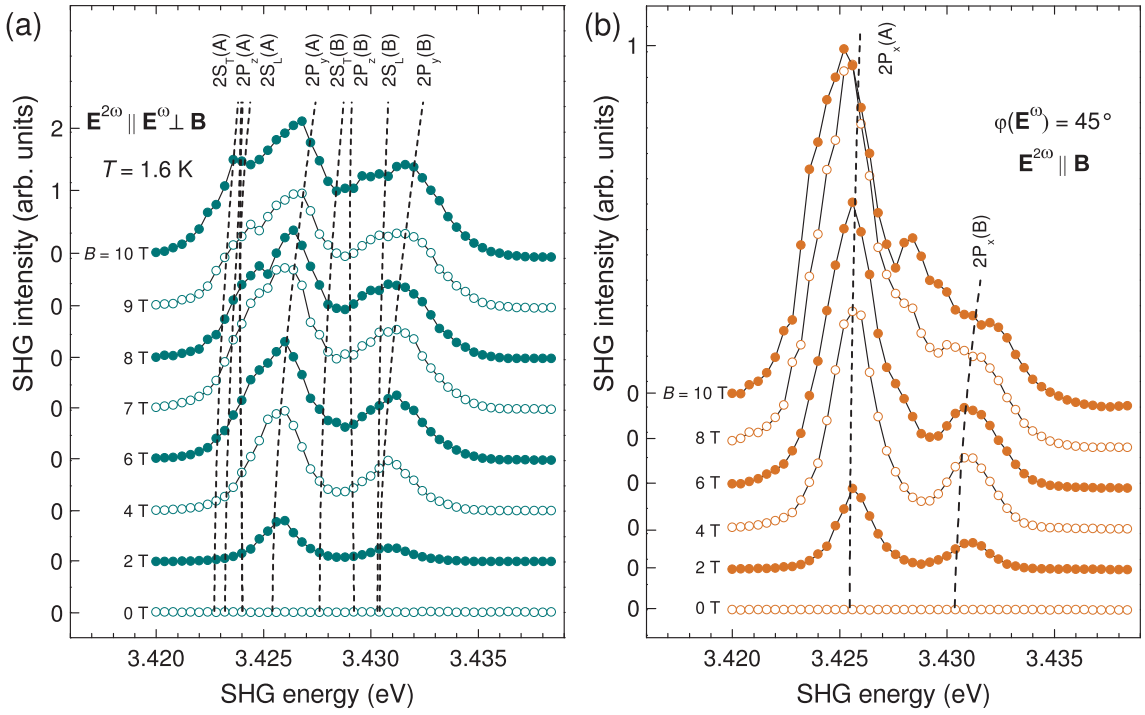

Figure 2.12: Magnetic-field-induced SHG spectra in the range of $2S/2P$ exciton states measured at $T = 1.6$ K. (a) $\mathbf{E}^{2\omega} \parallel \mathbf{E}^{\omega} \perp \mathbf{B}$. (b) $\mathbf{E}^{2\omega} \parallel \mathbf{B}$ and $\varphi = 45°$. Dashed lines give solutions of the model calculation given in Eq. (2.28).

The double-peak structure observed in low magnetic fields $B \leq 6$ T, as shown,e.g., in Figs. 2.11 and 2.12, has its maxima around 3.425 eV and 3.431 eV. These en-

[3]The magneto-Stark effect as mechanism for magnetic-field-induced SHG was published in 2013 in Phys. Rev. Lett. by Lafrentz, et al. [27].

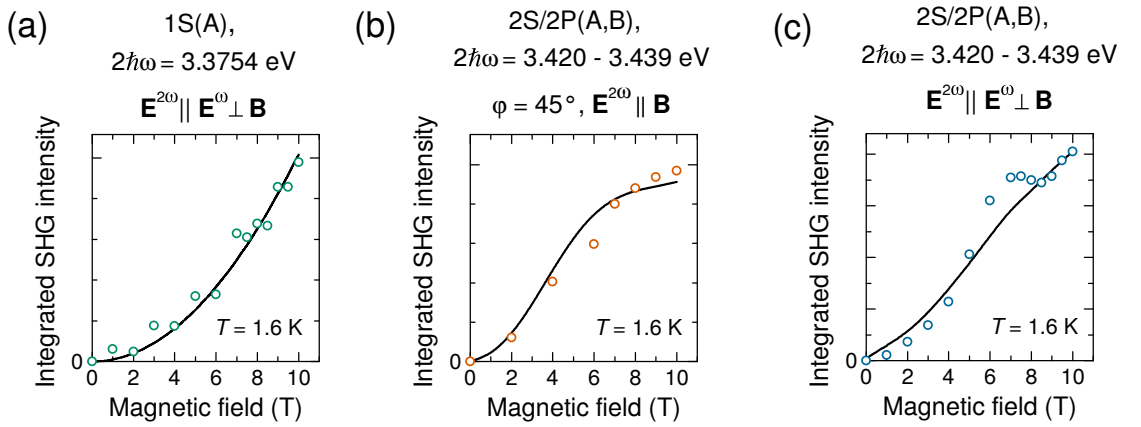

Figure 2.13: (a) Integrated SHG intensity for the strongest $1S$ line, $2\hbar\omega = 3.3754$ eV, [see Fig. 2.10 (a)] as a function of magnetic field (symbols). Line is a fit with $I_{\parallel}^{2\omega} \propto B^2$. (b) Integrated SHG intensity in the spectral range of $2S/2P(A,B)$ excitons, $23.420 \leq \hbar\omega \leq 3.439$ eV, (full spectral range of Fig. 2.12) as a function of magnetic field (symbols). Line is a model calculation for $2\hbar\omega = 3.4254$ eV (the energy of the strongest peak in the SHG spectra) and $\Gamma = 1.2$ meV. (c) Integrated SHG intensity as a function of magnetic field (symbols) in the same spectral range as (b), but for a different measurement geometry (see Fig. 2.12). Line is again model calculation exemplarily done for $2\hbar\omega = 3.4254$ eV and $\Gamma = 1.2$ meV.

ergies correspond well to the energies of the two-photon-allowed $2P_{x,y}(A,B)$ excitons [52,61]. In strong magnetic fields exceeding 6 T, these peaks evolve into complex structures, which are investigated in six different polarization configurations: (c1) $\mathbf{E}^{2\omega} \parallel \mathbf{E}^{\omega} \perp \mathbf{B}$, (c2) $\mathbf{E}^{2\omega} \parallel \mathbf{E}^{\omega} \parallel \mathbf{B}$, (c3) $\mathbf{E}^{2\omega} \perp \mathbf{B}$, $\varphi = 45°$, (c4) $\mathbf{E}^{2\omega} \parallel \mathbf{B}$, $\varphi = 45°$, (c5) $\mathbf{E}^{2\omega} \perp \mathbf{E}^{\omega} \perp \mathbf{B}$, and (c6) $\mathbf{E}^{2\omega} \perp \mathbf{E}^{\omega} \parallel \mathbf{B}$. Peak positions and signal strengths vary strongly for different configurations. Fig. 2.12 shows exemplarily two configurations (c1) and (c4): (a) $\mathbf{E}^{2\omega} \parallel \mathbf{E}^{\omega} \perp \mathbf{B}$ and (b) $\mathbf{E}^{2\omega} \parallel \mathbf{B}$, $\varphi(\mathbf{E}^{\omega}) = 45°$. Their direct comparison leads to the conclusion that signals from the various $n = 2$ states originate from different microscopic mechanisms possessing dinstinct symmetries. As a consequence, the $2S$, $2P_x$, $2P_y$, or $2P_z$ states become selectively pronounced by the choice of incoming and outgoing polarizations. SHG rotational anisotropies are measured at various energies, fields, and configurations (see Sec. 2.3). Figs. 2.14 and 2.15 display selected anisotropies to illustrate the most dominant attributes. Fig. 2.14 shows anisotropies at $2\hbar\omega = 3.424$ eV detected in different geometries, and measured at $B = 10$ T and $T = 1.6$ K. The orientation of clubs is governed by the direction of the magnetic field. Strongest signals are observed perpendicular to the field direction ($I^{2\omega} \propto \mathbf{P}^{2\omega} \perp \mathbf{B}$). Anisotropies of further spectral maxima are given in Fig. 2.15. Apparently, they show different patterns depending on the exciton states involved. The amplitude ratios between different configurations vary strongly for different energies, for example, compare ratios of parallel (blue) and crossed (red) configurations in Fig. 2.15. The shapes in the perpendicular geometry $I_{\perp}^{2\omega}$ are readily energy dependent; compare red shapes in Figs. 2.15 (b), (d), and

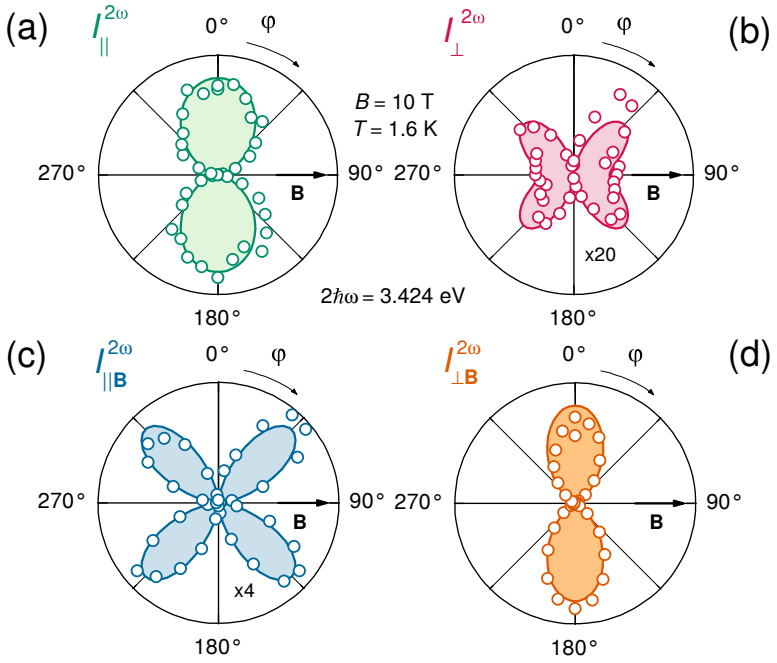

Figure 2.14: Angular dependences of the magnetic-field-induced SHG intensity at 3.424 eV for different geometries and $B = 10$ T. Open circles represent the measured data and lines show fittings following Eqs. (2.7)-(2.12) using the suitable relations from Tab. 2.2. Interference among different mechanisms is taken into account according to Eq. (1.23). (a) $\mathbf{E}^{2\omega} \parallel \mathbf{E}^{\omega}$; fit according to Eq. (2.7). (b) $\mathbf{E}^{2\omega} \perp \mathbf{E}^{\omega}$; fit according to $I^{2\omega} \propto \left(a \sin\varphi + b \sin\varphi \cos^2\varphi\right)^2$ with $a/b = 1/2$. (c) $\mathbf{E}^{2\omega} \parallel \mathbf{B}$; fit according to Eq. (2.8). (d) $\mathbf{E}^{2\omega} \perp \mathbf{B}$; fit according to $I^{2\omega} \propto \cos^4\varphi$.

(f). A more detailed discussion of the SHG polarization properties will follow in the Sec. 2.8.4, after the development of a microscopic theory in Sec. 2.8.2.

The magnetic-field dependence of the spectral-integrated SHG intensity shows a quadratic increase in low fields $B < 6$ T for all configurations, but with individual curvatures. In magnetic fields exceeding $B > 6$ T, this dependence becomes complex, too. For example, the configuration $\mathbf{E}^{2\omega} \parallel \mathbf{B}$ with $\varphi = 45°$ leads to a saturation behavior, whereas the overall signal in the configuration $\mathbf{E}^{2\omega} \parallel \mathbf{E}^{\omega} \perp \mathbf{B}$ shows a step at around $B = 7$ T and increases further afterwards; compare Figs. 2.13 (b) and (c). These behaviors, which are not observed for $1S$ states, point out that the dominant mechanisms for the magnetic-field-induced SHG differ for the $n = 1$ and $n = 2$ states in ZnO.

The temperature dependence of the $2S/2P$ SHG intensity will be discussed in detail in Sec. 2.10, where it will be given in Fig. 2.20 (a). Here, it is only mentioned for completness, that it shows a similar, though, slightly faster decrease compared to that of the $n = 1$ states.

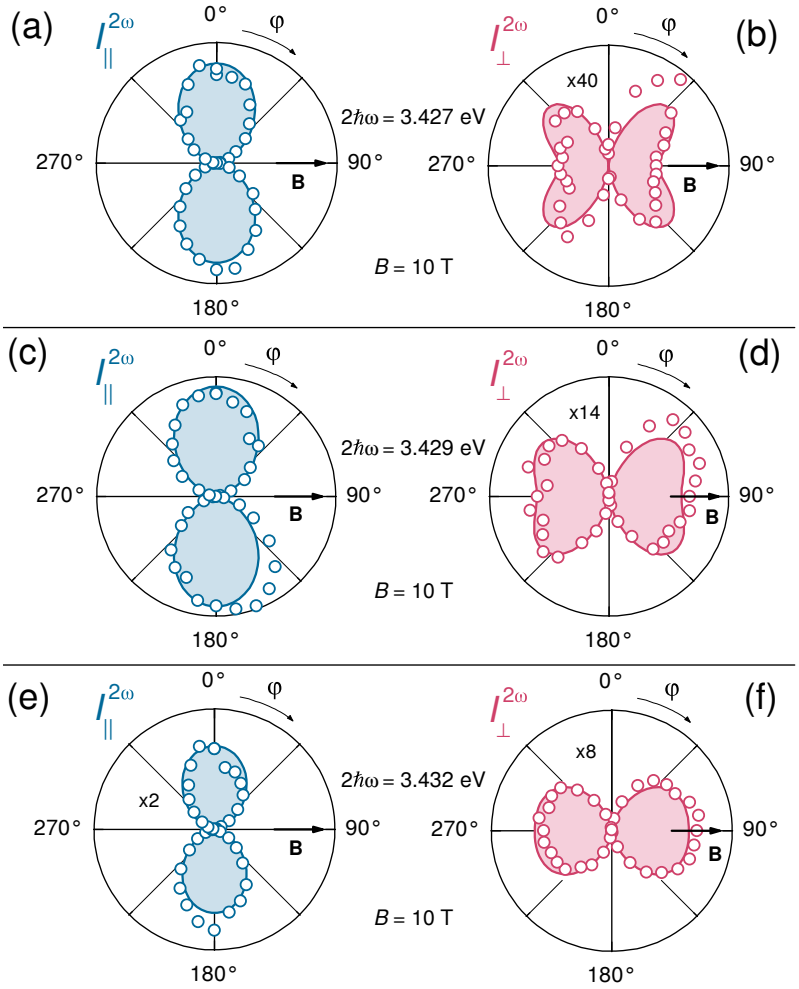

Figure 2.15: Angular dependences of the induced SHG intensity for different energies and $B = 10$ T. Open blue circles represent the measured intensity $I_{\parallel}^{2\omega}$ for $\mathbf{E}^{2\omega} \parallel \mathbf{E}^{\omega}$, and open red circles represent the measured intensity $I_{\perp}^{2\omega}$ for $\mathbf{E}^{2\omega} \perp \mathbf{E}^{\omega}$. Solid lines show fittings with $I_{\parallel}^{2\omega} \propto \cos^2\varphi$ and $I_{\perp}^{2\omega} \propto \left(a\sin\varphi + b\sin\varphi\cos^2\varphi\right)^2$; according to Eqs. (2.11) and (2.12). a and b take into account interference between spin Zeeman effects on S and P envelopes, respectively, following Eq. (1.23). (a) and (b) $2\hbar\omega = 3.427$ eV; $I_{\parallel}^{2\omega}/I_{\perp}^{2\omega} \approx 40/1$; $I_{\perp}^{2\omega}$ with $a/b \approx 3/4$. (c) and (d) $2\hbar\omega = 3.429$ eV; $I_{\parallel}^{2\omega}/I_{\perp}^{2\omega} \approx 14/1$; $I_{\perp}^{2\omega}$ with $a/b \approx 1/1$. (e) and (f) $2\hbar\omega = 3.432$ eV; $I_{\parallel}^{2\omega}/I_{\perp}^{2\omega} \approx 3/1$; $I_{\perp}^{2\omega}$ with $a/b \approx 2/1$.

2.8.2 Theoretical considerations

Interpretation of the observed SHG of $n = 2$ states in ZnO requires a microscopic theory focused on their specific properties. Although theoretical publications on harmonics generation are numerous, e.g., [65–75], and SHG was suggested to selectively probe excitons [76, 77], the role of excitons in harmonics generation has not been discussed theoretically, yet. In the following section, an applicable theory is developed in two steps. First, energies and wave functions of exciton and polariton states in ZnO are analyzed in electric and magnetic fields. Remember that S states in ZnO are polaritons, and P states are not. However, when they become mixed, all resulting states are coupled to the light field. Due to the interaction of the $2S$ states with photons two polariton branches for each of the $2S/2P$ mixed states are formed [78]. For the energies of the polariton branches the interaction of the mixed excitons with photons, and their respective contribution to the dielectric function has to be evaluated. However, the energies of the lower polariton branch (LPB) and upper polariton branch (UPB) can be approximated by considering the energies $\mathcal{E}(2S_T)$ and $\mathcal{E}(2S_L)$ for the $2S$ polariton energy, respectively [78]. The mixing of states and their consequent symmetry reduction will be of particular interest in later discussions. Second, magnetic and electric effects will be analyzed with regard to how they induce new contributions to $\chi^{(2)}$. Afterwards, the observations are interpreted in Sec. 2.8.4 based on the deduced mechanisms.

In analogy to the experiments, the same geometry $\mathbf{k}_{\mathrm{exc}} \parallel \mathbf{k} \parallel \mathbf{z}$, $\mathbf{B} \parallel \mathbf{x}$, and $\mathbf{E} \parallel \mathbf{y}$ is theoretically analyzed, where crystallographic SHG is forbidden.

$2S/2P$ States in an Electric Field

In C_{6v} a static electric field $\mathbf{E} \perp \mathbf{z}$ is represented by Γ_5. Its Stark effect (see Sec. 1.1.5) couples $2S(\Gamma_5)$ and $2P(\Gamma_{1,6})$ states for the A- and B-series in ZnO [60]. The $n = 2$ states of the C-series are not investigated and therefore not discussed. The couplings are described by the 2×2 Hamiltonian

$$\hat{H}_{2S/2P_y} = \begin{pmatrix} \mathcal{E}_{2S} & 3eE_y a_{\mathrm{B}} \\ 3eE_y a_{\mathrm{B}} & \mathcal{E}_{2P_y} \end{pmatrix} . \tag{2.23}$$

where a_{B} is the exciton Bohr radius, $\mathcal{E}_{2S}$ is the zero-field energy of the $2S$ polariton, and $\mathcal{E}_{2P_y}$ is the zero-field energy of the $2P_y$ exciton state. Its solutions are the coupled states

$$\mathcal{E}^{\pm}_{2S/2P_y} = \frac{1}{2}\left[\mathcal{E}_{2S} + \mathcal{E}_{2P_y} \pm \sqrt{(\mathcal{E}_{2P_y} - \mathcal{E}_{2S})^2 + 36(eE_y a_{\mathrm{B}})^2}\right] . \tag{2.24}$$

Their wave functions are obtained by

$$\Psi_{2S/2P_y} = C_{2S}(E_y)\Psi_{2S} + C_{2P_y}(E_y)\Psi_{2P_y}, \tag{2.25}$$

with

$$C_{2S}(E_y) = \frac{\mathcal{E}_{2P_y} - \mathcal{E}^{\pm}_{2S/2P_y}}{\sqrt{(3eE_y a_{\mathrm{B}})^2 + (\mathcal{E}_{2P_y} - \mathcal{E}^{\pm}_{2S/2P_y})^2}}, \tag{2.26}$$

$$C_{2P_y}(E_y) = -\frac{3eE_y a_{\mathrm{B}}}{\sqrt{(3eE_y a_{\mathrm{B}})^2 + (\mathcal{E}_{2P_y} - \mathcal{E}^{\pm}_{2S/2P_y})^2}}. \tag{2.27}$$

$2S/2P$ States in a Magnetic Field

A magnetic field perpendicular to the principle axis transforms like Γ_5, too. In contrast to an electric field of odd parity, a magnetic field is in first order of even parity. But, similar to the just considered effect of the electric field, the effective electric field $E_{\mathrm{eff}} = \frac{\hbar}{M_{\mathrm{exc}}} k_{\mathrm{exc}} B_x$ of the magneto-Stark effect (see Sec. 1.1.5) may mix the envelope functions of $2S$ and $2P_y$ states of different parity. At the same time, a magnetic field mixes $2P_z$ and $2P_y$ states of same parity due to the orbital Zeeman effect. The $2S/2P_z/2P_y$ mixed states $\mathcal{E}^{i}_{2S/2P_z/2P_y}$ are obtained as eigenenergies of the Hamiltonian[4]

$$\hat{H}^{\pm}_{2S/2P_z/2P_y} = \begin{pmatrix} \mathcal{E}^{\pm}_{2S}(B_x) & 0 & 3eE_{\mathrm{eff}}a_{\mathrm{B}} \\ 0 & \mathcal{E}^{\pm}_{2P_z}(B_x) & g_{\mathrm{orb}}\mu_{\mathrm{B}}B_x \\ 3eE_{\mathrm{eff}}a_{\mathrm{B}} & g_{\mathrm{orb}}\mu_{\mathrm{B}}B_x & \mathcal{E}^{\pm}_{2P_y}(B_x) \end{pmatrix}. \tag{2.28}$$

The diagonal terms can take into account the diamagnetic shift and spin splitting:

$$\mathcal{E}^{\pm}_{2S}(B_x) = \mathcal{E}_{2S}(\mathbf{B}=0) + 14C_d B_x^2 \pm \mu_{\mathrm{B}} B_x g_{\mathrm{e}}^{\perp}/2\ , \tag{2.29}$$

$$\mathcal{E}^{\pm}_{2P_z}(B_x) = \mathcal{E}_{2P_z}(\mathbf{B}=0) + 12C_d B_x^2 \pm \mu_{\mathrm{B}} B_x g_{\mathrm{e}}^{\perp}/2\ , \tag{2.30}$$

$$\mathcal{E}^{\pm}_{2P_y}(B_x) = \mathcal{E}_{2P_y}(\mathbf{B}=0) + 12C_d B_x^2 \pm \mu_{\mathrm{B}} B_x g_{\mathrm{e}}^{\perp}/2\ . \tag{2.31}$$

Here, C_d describes the diamagnetic shift, and g_{orb} the orbital g-factor. Expressions for C_d and g_{orb} are given in Ref. [31]. The off-diagonal perturbations in the Hamiltonian (2.28) mix states of same spin state and polariton branch only. In fact, it is sufficient to consider solely the mixing of envelope functions, although there are in

[4] The electron-hole short-range exchange splitting is assumed to be zero for all $2S$ and $2P$ states. All states are two-fold degenerate with respect to their hole spin projection, because the hole $g_h^{\perp}$-factor is assumed to be zero, too; see Ref. [49].

principle 24 mixed A and B polariton states each. Nevertheless, the $2S$ parts lead to the formation of LPB and UPB for each mixed state.

Their energies $\mathcal{E}^i_{2S_{\rm T}/2P_z/2P_y}$ ($i = 1, 2, 3$ describing the new solutions of Eq. (2.28)) of the LPB and $\mathcal{E}^i_{2S_{\rm L}/2P_z/2P_y}$ of the UPB are found as roots of the characteristic equation:

$$(\mathcal{E}^i-\mathcal{E}^{\pm}_{2S})(\mathcal{E}^i-\mathcal{E}^{\pm}_{2P_z})(\mathcal{E}^i-\mathcal{E}^{\pm}_{2P_y})-(3eE_{\rm eff}a_{\rm B})^2(\mathcal{E}^i-\mathcal{E}^{\pm}_{2P_z})-(g_{\rm orb}\mu_{\rm B}B_x)^2(\mathcal{E}^i-\mathcal{E}^{\pm}_{2S})=0, \tag{2.32}$$

with $\mathcal{E}_{2S} = \mathcal{E}_{2S_{\rm T}}$ for LPB and $\mathcal{E}_{2S} = \mathcal{E}_{2S_{\rm L}}$ for UPB. Their eigenfunctions are built according to

$$\Psi^i_{2S/2P_z/2P_y} = C^i_{2S}(B_x)\Psi_{2S} + C^i_{2P_z}(B_x)\Psi_{2P_z} + C^i_{2P_y}(B_x)\Psi_{2P_y}, \tag{2.33}$$

with coefficients

$$C^i_{2S} = \frac{3eE_{\rm eff}a_{\rm B}(\mathcal{E}^i - \mathcal{E}^{\pm}_{2P_z})}{\xi}, \tag{2.34}$$

$$C^i_{2P_z} = \frac{g_{\rm orb}\mu_{\rm B}B_x(\mathcal{E}^i - \mathcal{E}^{\pm}_{2S})}{\xi}, \tag{2.35}$$

$$C^i_{2P_y} = \frac{(\mathcal{E}^i - \mathcal{E}^{\pm}_{2S})(\mathcal{E}^i - \mathcal{E}^{\pm}_{2P_z})}{\xi}. \tag{2.36}$$

The denominator ξ is given by

$$\xi = \sqrt{(\mathcal{E}^i - \mathcal{E}^{\pm}_{2S})^2(\mathcal{E}^i - \mathcal{E}^{\pm}_{2P_z})^2 + (3eE_{\rm eff}a_{\rm B})^2(\mathcal{E}^i - \mathcal{E}^{\pm}_{2P_z})^2 + (g_{\rm orb}\mu_{\rm B}B_x)^2(\mathcal{E}^i - \mathcal{E}^{\pm}_{2S})^2}. \tag{2.37}$$

The Hamiltonian (2.28) can take into account effects of a static electric field E_y, as well, when $E_{\rm eff}$ is replaced with $E_{\rm eff} \pm E_y$. The $\pm$ sign shows their relative alignment; parallel and antiparallel, respectively.

In addition, the spin Zeeman effect of a magnetic field B_x lifts the degeneracy of the $2P_x$ and $2P_y$ states reducing their symmetries. Nevertheless, the $2P_x$ state does not become mixed with other $2P$ or $2S$ states. Its energy is calculated by:

$$\mathcal{E}^{\pm}_{2P_x}(B_x) = \mathcal{E}_{2P_x} + 6C_dB_x^2 \pm \mu_{\rm B}B_x g_{\rm e}^{\perp}/2 \tag{2.38}$$

2.8.3 Mechanisms

The newly derived states demand to discuss selection rules and polarization dependences once more. The optical nonlinear susceptibility $\chi_{ijl}(\mathcal{E}_{\rm exc}, \mathbf{k}_{\rm exc}, \mathbf{B}, \mathbf{E})$ in vicinity of an exciton resonance $\mathcal{E}_{\rm exc} = 2\hbar\omega$ can be written microscopically in the general form:

$$\begin{aligned}\chi_{ijl}(\mathcal{E}_{\rm exc}, \mathbf{k}_{\rm exc}, \mathbf{B}, \mathbf{E}) &\propto \sum_v \frac{\left\langle G|\hat{V}_i^{2\omega}|\Psi_{\rm exc}\right\rangle \left\langle \Psi_{\rm exc}|\hat{V}_j^{\omega}|\psi_v\right\rangle \left\langle \psi_v|\hat{V}_l^{\omega}|G\right\rangle}{(\mathcal{E}_{\rm exc} - 2\hbar\omega - {\rm i}\Gamma_{\rm exc})(\mathcal{E}_v - \hbar\omega)} \\ &\approx \frac{\rm i}{\Gamma_{\rm exc}} \left\langle G|\hat{V}_i^{2\omega}|\Psi_{\rm exc}\right\rangle M^{\rm 2ph}_{{\rm exc},G}. \end{aligned} \tag{2.39}$$

$|G\rangle$ denotes the unperturbed ground state with zero energy, $|\psi_v\rangle$ represents intermediate virtual states, $|\Psi_{\rm exc}\rangle$ is the exciton wave function, and $\Gamma_{\rm exc}$ its damping constant. Eq. (2.39) has to be summed up over all intermediate states that satisfy the symmetry selection rules for the two-photon (2ph) transition from ground to exciton state described by the matrix element $M^{\rm 2ph}_{{\rm exc},G}$. The perturbations $\hat{V}^{\omega}$ of the incoming light field $\mathbf{E}^{\omega} = (E_x^{\omega}, E_y^{\omega}, 0)$ can be expanded in a Taylor series:

$$\hat{V}^{\omega}_{x(y)} = \frac{ie}{m_0\omega}\hat{p}_{x(y)} \exp(ik_z r_z) \approx \frac{ie}{m_0\omega}\hat{p}_{x(y)}(1 + ik_z r_z + ...)\,, \tag{2.40}$$

Here, e is the electron charge and $\hat{p}_{x(y)}$ the projections of the momentum operator $\hat{\mathbf{p}}$ onto the direction of light polarization (x or y, respectively). For $\hat{V}^{2\omega}_{x(y)}$, k_z and ω have to be replaced by $2k_z$ and 2ω. The analysis will be limited to the two terms of lowest order in the expansion of $\exp({\rm i}kr)$ and consider the matrix elements $\hat{V}^{\omega(2\omega)}_{x(y)} = \hat{D}^{\omega(2\omega)}_{x(y)} + \hat{Q}^{\omega(2\omega)}_{x(y)z}$. The first term $\hat{D}^{\omega}_{x(y)} = (ie/m_0\omega)\hat{p}_{x(y)}$ corresponds to the electric-dipole (ED) approximation. The operator $\hat{Q}^{\omega}_{x(y)z} = -(ek_z/m_0\omega)\hat{p}_{x(y)}r_z$ includes the electric-quadrupole (EQ) and magnetic-dipole (MD) contributions and its matrix elements can be replaced by the sum of matrix elements of the electric-quadrupole operator $\hat{Q}^{\omega,q}_{x(y)z} = -(iek_z/2)r_{x(y)}r_z$ and magnetic-dipole operator $\hat{Q}^{\omega,m}_{x(y)z} = \pm(e\hbar k_z/2m_0\omega)\hat{L}_{y(x)}$; see for example in Ref. [24]. Here $\hat{\mathbf{L}}$ is the orbital momentum operator. Depending on the perturbations $\hat{V}^{\omega}$ or $\hat{V}^{2\omega}$ involved in the two-photon absorption or one-photon emission, we denote the resulting three-photon SHG process as $X^{2w}Y^{\omega}Z^{\omega}$, where X, Y, Z are either electric-dipole D, or electric-quadrupole/magnetic-dipole Q transitions. We note, that the presence of an EQ or MD transition for one of the steps either in excitation or in emission leads to a linear dependence of the susceptibility on k_z. Thus, they will be much weaker than the ED transtions.

Resonant SHG will be possible for states being simultaneously one- and two-photon allowed. In case of mixed states, where one part is one-photon allowed and another

part is two-photon allowed, the susceptibility will be proportional to the product of the respective mixing coefficients.

In ZnO, the direct ED transitions between the valence- and conduction-band states are allowed. The strongest one-photon process for $\mathbf{k} \parallel \mathbf{z}$ is the excitation of (or the emission from) the Γ_5 states with the S envelope. The respective matrix elements can be written as $D^{\omega,a}$ or $D^{2\omega,a}$, where the index a denotes the "allowed" transition within the ED approximation according to the notation of R. J. Elliot [79]. In contrast, the one-photon electric-dipole "forbidden" transitions to the $2P$ excitons in the noncentrosymmetric wurtzite semiconductors, such as ZnO, may occur because the valence- and conduction-band states are not of pure even or odd parities. These transitions are much weaker compared to the S exciton transitions, and can be described by the matrix elements $D^{\omega,f}$ or $D^{2\omega,f}$, where the index f denotes the "forbidden" transitions within the ED approximation [79]. In the given geometry, such "forbidden" transitions are theoretically possible only for the $2P_{x,y}$ states, and not for the $2P_z$ state. Alternatively, the one-photon emission from all three $2P_x$, $2P_y$, and $2P_z$ states may occur due to the magnetic-dipole transition described by the matrix element $Q^{2\omega,m}$.

The strongest two-photon process in ZnO is the excitation of $2P$ exciton states. They are electric-dipole allowed and use intermediate states in the valence- or conduction-band. Such process consists of one transition between valence and conduction band states and one transition between s and p envelopes in the same energy band. The relevant two-photon matrix element is $M^{\mathrm{2ph}}_{2P,G} \propto D^{\omega,a}D^{\omega,f}$. On the other hand, the direct two-photon absorption by the S exciton states in non-centrosymmetric semiconductors may occur within ED approximation via the intermediate virtual states in remote bands [80]. In this case the two-photon matrix element is $M^{\mathrm{2ph}}_{S,G} \propto D^{\omega,a}D^{\omega,a}$. However, such processes are much weaker than those for the $2P$ exciton states [81]. Alternatively, the S states can be excited in the two-photon process when the first transition is a MD transition (or ED transition of "forbidden" character) to the $2P_{x,y}$ states and the second one is a ED transition of "forbidden" character between the S and the P envelopes. In this case the two-photon matrix element is $M^{\mathrm{2ph}}_{S,G} \propto D^{\omega,f}Q^{\omega,m}$ (or $M^{\mathrm{2ph}}_{S,G} \propto D^{\omega,f}D^{\omega,f}$, respectively).

Although parity is in principle not a good quantum number in hexagonal ZnO, this symmetry is important for the permissiveness of exciton-(polariton) transitions. Mechanisms mixing spin wave functions of states of the same envelope function, i.e., same parity, will be discussed first. Afterwards mechanisms mixing different envelope functions will be analyzed.

Magnetic-Field-Induced SHG of S Excitons due to the Spin Zeeman Effect

Remember from the discussion about $1S$ excitons in Sec. 2.7, that in the chosen geometry the $S(A\Gamma_5, B\Gamma_5)$ states are one-photon allowed and form polariton branches. The $S(A\Gamma_1)$ and $S(B\Gamma_6)$ are two-photon allowed. Their two-photon processes involve either a quadrupole excitation or use intermediate virtual states in remote bands [80]. It is convenient to consider a two-photon excitation $Q^{\omega}D^{\omega}$ including one quadrupole to underline the high order of this process. The spin Zeeman effect mixes the Γ_{5y} and $\Gamma_{1,6}$ states leading to the observed SHG signals of $1S(A,B)$ exciton states. The same mechanism can also work for the $2S(A,B)$ and $1S(C)$ states. The respective SHG process $D^{2\omega}D^{\omega}Q^{\omega,m}$ is listed in the third row of Table 2.2. In the chosen geometry ($\mathbf{B} \parallel \mathbf{x}$) only the $S(\Gamma_{5y})$ wave functions become mixed and no emission in x-direction is possible, i.e., $\chi_{xxy} = 0$. The nonzero magnetic-field-induced susceptibilities $\chi_{yyy} = \chi_{yxx}$ are

$$\begin{aligned} \chi_{yyy}(\mathcal{E}^{\pm}_{\Gamma_{5y}/\Gamma_{1,6}}, k_{\mathrm{exc}}, B_x, 0) &\propto C_{\Gamma_5}(B_x)C_{\Gamma_{1,6}}(B_x)(k_z a_0) \\ &= \frac{2\mu_{\mathrm{B}} g_{\mathrm{exc}} B_x (\mathcal{E}_{\Gamma_5} - \mathcal{E}^{\pm}_{\Gamma_{5y}/\Gamma_{1,6}})(k_z a_0)}{(\mu_{\mathrm{B}} g_{\mathrm{exc}} B_x)^2 + 4(\mathcal{E}_{\Gamma_5} - \mathcal{E}^{\pm}_{\Gamma_{5y}/\Gamma_{1,6}})^2}. \end{aligned} \tag{2.41}$$

Here, g_{exc} is the exciton g-factor, a_0 the lattice constant, and $\mathcal{E}_{\Gamma_5}$ the zero-field energy of the respective polariton. The factor $a_0 k_z$ is a consequence of the quadrupole excitation.

Magnetic-Field-Induced SHG of P Excitons due to the Spin Zeeman Effect

Envelope orbitals parallel and perpendicular to the magnetic field orientation have to be discussed separately as their degeneracy is lifted.

a. The P_x state. Similar to the mechanism for the S states, the Γ_5 and Γ_1 spin states of the P_x excitons can become mixed due to the spin Zeeman effect. Their excitation is possible by two photons for polarizations $E^{\omega}_x \neq 0$ via dipole perturbations $\hat{V}^{\omega}_{x(y)} = \hat{D}^{\omega}_{x(y)}$ of the first photon and $\hat{V}^{\omega}_{x} = \hat{D}^{\omega}_{x}$ of the second photon or vice versa. The emission is possible due to the quadrupole perturbation $\hat{V}^{2\omega}_{x} = \hat{Q}^{2\omega}_{xz}$. The corresponding process $Q^{2\omega,m}D^{\omega}D^{\omega}$ is listed in the fourth row of Table 2.2. The fundamental mechanism is the same as for S states, but in different limits. The nonzero components $\chi_{xxy} = \chi_{xyx}$ are

$$\chi_{xxy}(\mathcal{E}_{2P_x}) \propto \frac{1}{2}(k_z a_0). \tag{2.42}$$

The susceptibility has no explicit magnetic field dependence, but the mechanism requires a finite magnetic field B_x for the mixing. The dependence on B_x is not seen in Eq. (2.42), because the exchange splitting of mixed states is neglected. As their energy is degenerated, already a very weak magnetic field is able to mix them in equal proportions. This mechanism can also be seen as "a phase transition": no field, no effect whereas a field $B > 0$ induces contributions independent of the field strength.

This mechanism is not linear in $\mathbf{B}$ and violates the relation $\chi_{yyy} = \chi_{yxx} + 2\chi_{xxy}$. Rotational anisotropy patterns for induced SHG of $2P_x$ states are: $I^{2\omega}_{\perp\mathbf{B}} = 0$, $I^{2\omega}_{\parallel\mathbf{B}} = |\chi_{xxy}|^2 \sin^2 2\varphi$, $I^{2\omega}_{\parallel} \propto |\chi_{xxy}|^2 \sin^2 2\varphi \sin^2 \varphi$, and $I^{2\omega}_{\perp} \propto |\chi_{xxy}|^2 \sin^2 2\varphi \cos^2 \varphi$. Another picture to understand this mechanism phenomenologically is based on the degeneracy lifting of $2P_x$ and $2P_y$ by the magnetic field, which is the same as a symmetry reduction.

b. The P_y state. The same symmetry reduction induces contributions of the $2P_y$ states. They lead to one nonzero susceptibility:

$$\chi^{2P_y}_{yyy}(\mathcal{E}^i_{2S/2P_z/2P_y}, k_{\mathrm{exc}}, B_x, 0) \propto \frac{1}{2} k_z a_0 C^i_{2P_y}(B_x), \ . \tag{2.43}$$

This process $Q^{2\omega}D^{\omega}D^{\omega}$ is listed in the fourth row in Table 2.2. For the rotational anisotropies of $2P_y$ follows: $I^{2\omega}_{\perp\mathbf{B}} \propto |\chi_{yyy}|^2 \cos^4 \varphi$, $I^{2\omega}_{\parallel} \propto |\chi_{yyy}|^2 \cos^6 \varphi$, $I^{2\omega}_{\perp} \propto |\chi_{yyy}|^2 \cos^4 \varphi \sin^2 \varphi$, and $I^{2\omega}_{\parallel\mathbf{B}} = 0$. Its effect is reduced by the magnetic field mixing of the $2S/2P_z/2P_y$ envelopes that will be discussed next.

Electric-Field-Induced SHG due to the Stark Effect

In addition to the mixing of different spin states of the same envelope state, electric and magnetic fields mix different envelope states. Envelopes of different parity (although parity is in principle not a good quantum number in ZnO, the parity of envelope states is important for permissiveness) are mixed by a perturbation of odd parity, e.g., the electric field. An electric field E_y of odd parity mixes $2S$ and $2P_y$ states of opposite parity due to the Stark effect for A and B series. Matrix elements for excitation ($2P_y$) and emission ($2S$) in Eq. (2.39) are allowed in the ED approximation. The corresponding process $D^{2\omega}D^{\omega}D^{\omega}$ is listed in the first row in Table 2.2. Corresponding SHG signals are only observed for incoming light with a nonzero component $E^{\omega}_y \neq 0$, which is necessary for the excitation of the $2P_y$ state, because $\chi_{yxx} = 0$. Resulting electric field-induced-contributions $\chi_{yyy} = 2\chi_{xxy} = 2\chi_{xyx}$ are:

$$\chi_{yyy}(\mathcal{E}^{\pm}_{2s/2P_y}, k_{\mathrm{exc}}, 0, E_y) \propto C_{2s}(E_y) C_{2P_y}(E_y) \tag{2.44}$$

$$= \frac{3eE_y a_{\mathrm{B}} (\mathcal{E}_{2P_y} - \mathcal{E}^{\pm}_{2s/2P_y})}{(3eE_y a_{\mathrm{B}})^2 + (\mathcal{E}_{2P_y} - \mathcal{E}^{\pm}_{2s/2P_y})^2} \ . \tag{2.45}$$

The energy correction due to the electric field is much smaller than the zero-field splitting of the exciton states $|eE_y a_\mathrm{B}| \ll |\mathcal{E}_{2P} - \mathcal{E}_{2S_{\mathrm{T(L)}}}|$. Hence, the susceptibilities depend linearly on the electric (magnetic) field E_y (E_eff). In the opossite case a saturation is expected.

Magnetic-Field-Induced SHG of Mixed $2S/2P$ Excitons due to the Magneto-Stark and Orbital Zeeman Effects

The effective electric field due to the magneto-Stark effect (see Sec. 1.1.5) mixes $2S$ and $2P_y$ envelope functions of opposite parities similar to the Stark effect of an electric field. Furthermore, the orbital Zeeman effect couples (in analog to the spin Zeeman effect mixing spin states) $2P_y$ and $2P_z$ envelopes of same parity. The wave functions of the resulting states $\mathcal{E}^i_{2S/2P_z/2P_y}$ $(i = 1, 2, 3)$ are constructed from all three unperturbed states with coefficients $C^i_{2S(2P_z,2P_y)}(B_x)$.

There are three possible mechanisms generating second harmonic of these states, all of them excite the Ψ_{2P_y} component via the ED perturbations $\hat{D}^\omega_{x(y)}\hat{D}^\omega_y$, where one photon has to possess a nonzero polarization component perpendicular to the magnetic field. Their difference lies in the emission: (i) emission due to the Ψ_{2S} component via ED dipole perturbation $\hat{D}^{2\omega}_{x(y)}$; (ii) emission due to the Ψ_{2P_z} component via the quadrupole perturbation $\hat{Q}^{2\omega}_{x(y)z}$; and (iii) emission due to the Ψ_{2P_y} component via the quadrupole perturbation $\hat{Q}^{2\omega}_{yz}$ (or via remote states $\hat{D}^{2\omega,f}_{yz}$).

(i) *The magneto-Stark effect*: The effective field $E_\mathrm{eff} = \frac{\hbar}{M_\mathrm{exc}} k_\mathrm{exc} B_x$ on exciton states coupling $2S$ and $2P_y$ envelopes via the magneto-Stark effect enables the process $D^{2\omega}D^\omega D^\omega$, which is listed in the second row of Table 2.2. Its magnetic-field-induced nonzero susceptibilities $\chi_{yyy} = 2\chi_{xxy} = 2\chi_{xyx}$ are:

$$\chi^{2S/2P_y}_{yyy}(\mathcal{E}^i_{2S/2P_z/2P_y}, k_{exc}, B_x, 0) \propto C^i_{2S}(B_x) C^i_{2P_y}(B_x). \tag{2.46}$$

The susceptibilities depend both on the magnetic field and the wave vector only because of the effective electric field $E_\mathrm{eff} = \frac{\hbar}{M_\mathrm{exc}} k_\mathrm{exc} B_x$. This dependence is linear when the energy of the effective electric field is smaller than the zero field splitting of the states and it saturates in the opposite case.

(ii) *The orbital Zeeman effect*: Mixing of $2P_z$ and $2P_y$ envelopes induces the SHG process $Q^{2\omega}D^\omega D^\omega$. It is listed in the fifth row of Table 2.2. The magnetic-field-induced nonzero susceptibilities $\chi_{yyy} = 2\chi_{xxy} = 2\chi_{xyx}$ are:

$$\begin{aligned}\chi^{2P_y/2P_z}_{yyy}(\mathcal{E}^i_{2S/2P_z/2P_y}, k_\mathrm{exc}, B_x, 0) \propto \\ k_z a_B C^i_{2P_z}(B_x) C^i_{2P_y}(B_x)\end{aligned} \tag{2.47}$$

This dependence on $\mathbf{B}$ is linear when the energy split due to the orbital Zeeman effect is smaller than the zero field splitting of the states. In the opposite case, the mixing and consequent SHG signal is saturated. Its signals are expected to be much weaker than those induced by the magneto-Stark effect and not important at energies where the $2S$ component is dominant.

(iii) *Spin Zeeman Effect*: See the discussion on $1S$ excitons.

The rotational anisotropy patterns for the SHG polarization for both the magneto-Stark and the orbital Zeeman effect processes look the same. Signals vanish in the crossed geometry $\mathbf{E}^{2\omega} \perp \mathbf{E}^{\omega}$ because $I_{\perp}^{2\omega}(\mathcal{E}^{i}_{2S/2P_z/2P_y}) \propto |\chi_{yxx}|^2 = 0$ for any polarization direction of the excitation light $\mathbf{E}^{\omega}$. The SHG signal in the parallel geometry $\mathbf{E}^{2\omega} \parallel \mathbf{E}^{\omega}$ can be modeled as $I_{\parallel}^{2\omega} \propto |\chi_{yyy}|^2 \cos^2\varphi$, while the signal polarized along the magnetic field direction varies as $I_{x}^{2\omega} \propto |\chi_{xxy}|^2 \sin^2 2\varphi$. Signals polarized perpendicular to the magnetic field direction can be modeled as $I_{y}^{2\omega} \propto |\chi_{yyy}|^2 \cos^4\varphi$ since $\chi_{yxx} = 0$.

Summary

Mechanisms	$1s$, $2s$	$2s/2p_y$	$2P_z/2P_y$	$2P_y$	$2P_x$
Stark effect $D_i^{2\omega} D_j^{\omega} D_l^{\omega}$ $E_y \neq 0$, $B_x = 0$		$\chi_{yyy} = 2\chi_{xxy} \neq 0$, $\chi_{yxx} = 0$ ♠			
Magneto-Stark effect $D_i^{2\omega} D_j^{\omega} D_l^{\omega}$ $E_y = 0$, $B_x \neq 0$		$\chi_{yyy} = 2\chi_{xxy} \neq 0$, $\chi_{yxx} = 0$ ♠			
Spin Zeeman effect $D_i^{2\omega} D_j^{\omega} Q_l^{\omega,m}$ $E_y = 0$, $B_x \neq 0$	$\chi_{yyy} = \chi_{yxx} \neq 0$, $\chi_{xxy} = 0$ ♦				
Spin Zeeman effect $Q_i^{2\omega,m} D_j^{\omega} D_l^{\omega}$ $E_y = 0$, $B_x \neq 0$				$\chi_{yyy} \neq 0$, ★ $\chi_{xxy} = \chi_{yxx} = 0$	$\chi_{xxy} \neq 0$, ♣ $\chi_{yyy} = \chi_{yxx} = 0$
Orbital Zeeman effect $Q_i^{2\omega,m} D_j^{\omega} D_l^{\omega}$ $E_y = 0$, $B_x \neq 0$			$\chi_{yyy} = 2\chi_{xxy} \neq 0$, $\chi_{yxx} = 0$ ♠		

Table 2.2: List of induced contributions to $\chi^{(2)}$ due to different mechanisms in external electric and magnetic fields acting on $1S(A,B,C)$, $2S(A,B,C)$ and $2P(A,B)$ exciton(-polariton) states in ZnO. Tensor components are given for the experimental geometry $\mathbf{k} \parallel \mathbf{z}$, $\mathbf{E} = (0, E_y, 0)$, and $\mathbf{B} = (B_x, 0, 0)$. $\chi_{xxy} = \chi_{xyx}$, because the incoming photons are indistinguishable.

All mechanisms considered above for field induced SHG signals of S and P excitons(-polaritons) in ZnO are summarized in Table 2.2. Their model polarization anisotropy patterns are displayed in Fig. 2.16. Although, this theoretical analysis is performed for wurtzite ZnO, the theoretical approach and its derived mechanisms can be carried forward to exciton structures of other semiconductors.

Without going into details, the considered mechanisms do not work in the Faraday geometry $\mathbf{B} \parallel \mathbf{k} \parallel \mathbf{z}$, i.e., a magnetic field applied along the hexagonal z-axis does

not mix Γ_5 and Γ_1 states. The orbital Zeeman term $L_z B_z$ does not lead to an admixture of $2P_z$, and the effective electric field $\mathbf{E}_{\text{eff}}$ vanishes for $\mathbf{B} \parallel \mathbf{k}$.

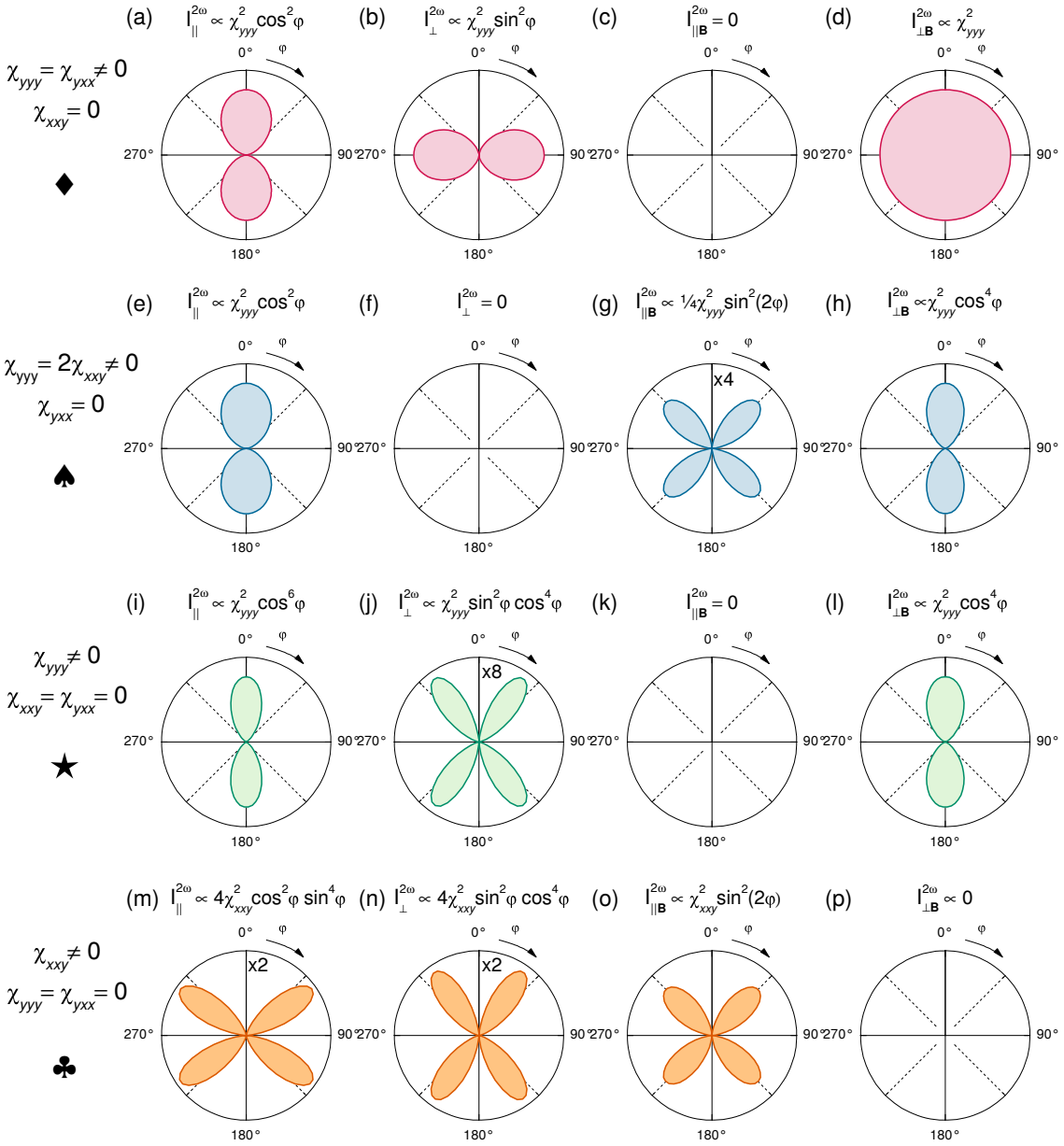

Figure 2.16: Theoretical predictions for rotational anisotropies of induced contributions for $I_{\parallel} \mapsto \mathbf{E}^{\omega} \parallel \mathbf{E}^{2\omega}$, $I_{\perp} \mapsto \mathbf{E}^{\omega} \perp \mathbf{E}^{2\omega}$, $I_{\parallel\mathbf{B}} \mapsto \mathbf{E}^{2\omega} \parallel \mathbf{B}$, and $I_{\perp\mathbf{B}} \mapsto \mathbf{E}^{2\omega} \perp \mathbf{B}$ according to Eqs. (2.7)-(2.12), respectively, obeying the relations summarized in Tab. 2.2: (a)-(d) Spin Zeeman effect for S ♦. (e)-(h) Stark effect / magneto-Stark effect / orbital Zeeman effect ♠. (i)-(l) Spin Zeeman effect for $2P_y$ ★. (m)-(p) Spin Zeeman effect for $2P_x$ ♣.

2.8.4 Discussion

In the following section, field induced mechanisms on exciton(-polaritons) presented in Sec. 2.8.2 are used to explain the experimental observations of Sec. 2.8.1. As a general rule, the mixing of states with different symmetries points out to be the key to induce resonant nonlinear susceptibilities, whereas the spin Zeeman, the orbital Zeeman, the magneto-Stark, and the Stark effect show distinct types of symmetry breaking. It will be shown that the nonlinear interaction of light and matter goes beyond the ED approximation in ZnO. Rotational anisotropy measurements of SHG signals give comprehensive information on the symmetry of involved nonlinear susceptibilities and underlying processes. Thus, they distinguish nonlinear optical mechanisms of different nature, which is especially important and helpful when more than one mechanism may be involved. Consequently, a thorough comparison of measured and predicted rotational anisotropies of the SHG intensity is performed. In addition, energy shifts in magnetic fields and field dependences of the SHG intensity are shown to be in accordance with the linked mechanisms.

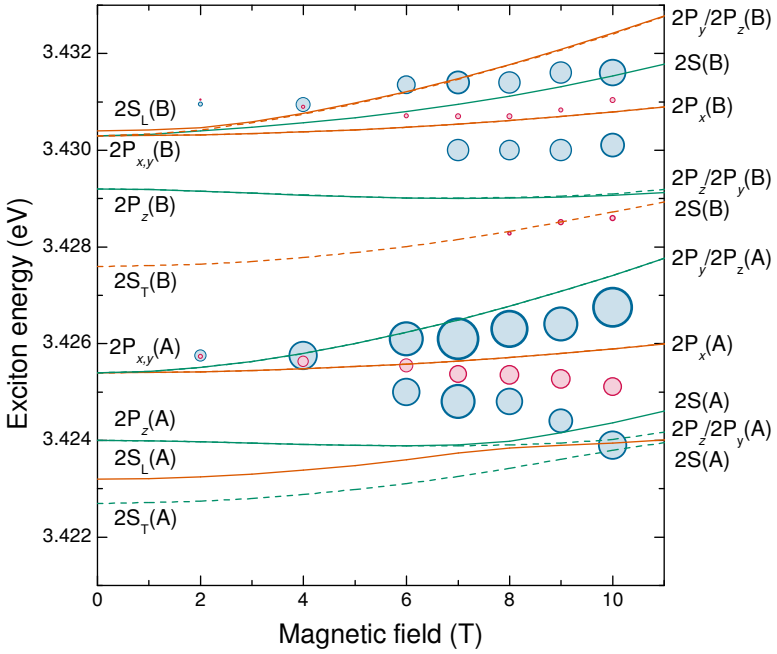

Figure 2.17: Magnetic field dependence of the $2S/2P$ states of A and B series. Lines plot the solutions of Eq. (2.28). Symbols display experimental data. Their circle size scales with the observed peak intensity. Blue and red circles represent the geometries $\mathbf{E}^{2\omega} \parallel \mathbf{E}^{\omega} \perp \mathbf{B}$ and $\mathbf{E}^{2\omega} \parallel \mathbf{B}$ with $\varphi(E^{\omega}) = 45°$, respectively. Labels on left side indicate the zero-field exciton energies, whereas labels on the right hand illustrate the dominant wave function character of the mixed states at 10 T. Solid and dashed lines plot results for the UPB and LPB, respectively.

Modeled energies (see lines in Fig. 2.17) depend strongly on the input parameters, which are the zero-field exciton energies, and electron and hole effective masses.

Calculations use zero-field exciton energies from Refs. [52,58]; see Table 5.1. Electron effective mass $m_e = 0.27m_0$ and hole effective mass are adopted from first principle calculations [49]: $m_{\parallel} = 2.74m_0$, $m_{\perp} = 0.54m_0$ for A series and $m_{\parallel} = 3.03m_0$, $m_{\perp} = 0.55m_0$ for B series. Static dielectric constants $\epsilon_{\parallel} = 8.49$ and $\epsilon_{\perp} = 7.40$ are taken from Ref. [54]. Spin Zeeman splittings are not included in the calculations for the mixed $2S/2P_z/2P_y$ states. The contributions to $\chi^{(2)}$ due to the spin Zeeman effect will be considered for rotational anisotropies, but its energies are neglected. When including the spin Zeeman splittings the number of lines in Fig. 2.17 would increase, which would disturb a comprehensive view, and the qualitative picture for the magnetic field dependences would not be improved.

Figure 2.17 shows the experimentally observed SHG peak energies and the theoretically modeled energies of contributing exciton(-polariton) states for fields up to $B = 10$ T. The radii of displayed experimental data scale with their respective peak intensities. The strongest SHG signals are observed for $I_{\parallel}^{2\omega}$ and their spectral maxima follow the modeled states with dominant proportions of $2P_y$ and $2S$; see blue circles in Fig. 2.17.

Anisotropies measured at $2\hbar\omega = 3.424$ eV and 3.429 eV correspond to states with a dominant $2S(A)$, $2S(B)$ part; see Fig. 2.14 and Figs. 2.15 (a) and (b). Anisotropies measured at $2\hbar\omega = 3.427$ and $2\hbar\omega = 3.432$ reflect states with a dominant $2P_y(A)$, $2P_y(B)$ part; see Fig. 2.15 (c) and Fig. 2.15 (d). These energies show at first glance the same anisotropy patterns. Thus, the main attributes will be discussed for $2\hbar\omega = 3.424$ eV with a dominant $2S$ part first.

The spin Zeeman effect, which delivered the explanation for the observed phenomena for $n = 1$ states, is valid for $2S(A)$ polaritons, too. However, a comparison of Fig. 2.10 (c) and Figs. 2.14 (a) and 2.14 (b) shows that the observed SHG anisotropies of $2S$ states are different from those of the $1S$: For the $2S(A)$ polariton the shape of $I_{\perp}^{2\omega}$ cannot be described by $\sin^2\varphi$, and $I_{\parallel}^{2\omega}$ and $I_{\perp}^{2\omega}$ do not have the same amplitude. These anisotropies need to be explained in first order by other mechanisms than the spin Zeeman effect. Already in Sec. 2.8, the by very strongr SHG intensities of $n = 2$ states implied a more efficient mechanism than for the $n = 1$ states. The magneto-Stark effect is the first mechanism to consider, as it is assumed to be the dominant mechanism for the $2S/2P(A,B)$ exciton(-polariton) region [27,57]. Indeed, it is able to explain the main appearances shown in Figs. 2.14 (a), 2.14 (c), and 2.14 (d), which resemble the predicted shapes for the magneto-Stark effect shown in Figs. 2.16 (e), (g), and (h), respectively. But a closer look at the non vanishing $I_{\perp}^{2\omega}$ reveals that the spin Zeeman effect on both the $2S(A)$ and $2P_y(A)$ states adds a very small contribution. The complex shape of $I_{\perp}^{2\omega}$ presented in Fig. 2.14 (b) can only be explained by a combination of magneto-Stark and spin Zeeman effects on the $2S(A)$ and $2P_y(A)$ parts; their predicted shapes are shown in Figs. 2.16 (b) and (j). The adherence of spin Zeeman contributions to $I_{\perp}^{2\omega}$ can be estimated to be of about 5% of the peak intensity of $I_{\parallel}^{2\omega}$ (remember that no SHG signals due to the mixing of envelopes is seen in this configuration): However, it follows

from the fit in Fig. 2.14 (b) that the spin Zeeman contribution from the $2P_y(A)$ is twice as strong as from the $2S(A)$ part. As a consequence, the SHG induced by the magneto-Stark effect involving only ED excitation as well as ED emission processes is about 40 times more efficient than the SHG due to a spin Zeeman induced process based on ED excitation processes and a QD emission process. The orbital Zeeman effect cannot be distinguished from the magneto-Stark effect via anisotropies (see Table 2.2) and might be of importance, too, due to the $2P_y/2P_z$ mixing. Especially it is true for the $2S(A)$ region, where the $2P_z(A)$ exciton lies energetically very close and within our spectral resolution. However, the probability of the quadrupole emission from the $2P_z$ state is very low in comparison with the probability of the dipole emission from the $2S$ state. Thus, we assume that the orbital Zeeman effect does not play a leading role and the magneto-Stark effect provides the dominant contribution to the SHG signal at $2S/2P$ excitons. This assumption would also explain that for high fields > 6 T the discrepancy between the energetically higher peak positions and calculated contributing polariton energies increases for both series.

Further, the weak nonzero signals in the crossed geometry, that do not follow from the magneto-Stark effect, are more pronounced in the range of the B-series. The anisotropy shapes for the B-series presented in Figs. 2.15 (c), (d), (e) and (f) show many similarities to those of the discussed A-series: Strongest signals are observed for $I_{\parallel}^{2\omega}$, and $I_{\parallel}^{2\omega}$ has a twofold $\cos^2\varphi$ pattern, whereas $I_{\perp}^{2\omega}$ is a mixture of a fourfold $\sin^2\varphi\cos^4\varphi$ and a twofold $\sin^2\varphi$ pattern. The stronger influence of 'S'-type spin Zeeman effect might stem from induced signals of $1S(C)$ or $3S(A)$ states lying in the same energy region. The $3S(A)$ polariton is a rather improbable explanation, because of its larger main quantum number, which reduces its oscillator strength drastically in comparison to $1S$ and $2S$ exciton states. By contrast, the $1S(C)$ is also seen to be strong and broad in the crystallographic SHG spectra; see Fig. 2.7. An additional contribution from the $1S(C)$ exciton would explain why we have observed a stronger influence of the 'S'-type spin Zeeman effect on the shape of the anisotropies of the B-series compared to those of the A-series, especially for $2\hbar\omega = 3.432$ eV where the ratio of $I_{\parallel}^{2\omega}/I_{\perp}^{2\omega} \approx 3/1$ is smallest; compare the relatively strong SHG signals for $\varphi \approx 90°$ in Fig. 2.15 (b) with those for $\varphi \approx 90°$ in Fig. 2.14 (b). Besides the $2S(B)$ region, this influence was also larger for the $2P_y(B)$ dominated states than for the $2P_y(A)$ dominated states; compare Figs. 2.15 (b) and 2.15 (d). The fact that this stronger influence is seen over a broad spectral range relates to a broad line width and, thus, to the $1S(C)$ state as well.

Contributions from the spin Zeeman effect on $2P_x$ states are best seen for $I_{\parallel\mathbf{B}}^{2\omega}$ in the geometry $\varphi(\mathbf{E}^{\omega}) = 45°$ and $\mathbf{E}^{2\omega} \parallel \mathbf{B}$, see Fig. 2.12 (b). The spectral maxima follow the calculated energies of the mixed $2P_x(A,B)$ exciton states; compare $2P_x$ lines and red circles in Fig. 2.17. Furthermore, the ratio of the spectral integrated intensities $I_{\parallel\mathbf{B}}^{2\omega}/I_{\parallel}^{2\omega}$ should be $1/4$ or less without the contribution from the spin Zeeman effect at the $2P_x$ states. While we have observed a ratio of about $1/3$, that clearly shows the importance of this spin Zeeman mechanism for the $2P_x$ orbitals oriented parallel

to the magnetic field. Nevertheless, contributions from this mechanism to $I_{\parallel}^{2\omega}$ are not noticed and the main part of the integrated SHG intensity in the $I_{\parallel\mathbf{B}}^{2\omega}$ spectra stems from $2S/2P_z/2P_y$ mixed states due to the magneto-Stark effect.

The developed theory describes well the measured angular dependences of SHG intensities and it is in reasonable accordance to the energy shifts of the exciton states ensuring the validity of the presented SHG mechanisms. The theory may not predict absolute values of the susceptibilities, but a comparison of the measured crystallographic and induced SHG signals shows that they are of the same order of magnitude. Accurate measurements of the second-order-susceptibility components can be found in Ref. [82, 83].

Another very intriguing feature of the discovered mechanisms is the complex behavior of the integrated SHG intensity; see Figs. 2.13 (b) and (c). SHG from the magneto-Stark and orbital Zeeman effects are expected to saturate when their energies become larger than the zero field splitting of the involved states. The typical values of the $|2S_T - 2P_y|$ exciton splitting is about 3 meV for A and B excitons in ZnO. While the longitudinal-transverse splitting of the $2S(A)$ exciton is about 0.5 meV, the respective splitting for the B exciton is about 3 meV. Thus, the saturation condition is reached for the orbital Zeeman effect ($g_{\mathrm{orb}}\mu_{\mathrm{B}}B_x$) around $B \approx 8$ T, but it is not fulfilled for the magneto-Stark effect $[3eE_{\mathrm{eff}}(B)a_{\mathrm{B}}]$ for $B \leq 10$ T. The spin Zeeman effect for the $2P_x$ state is independent of the magnetic field, whereas the susceptibility decreases with the fraction of C_{2P_y} for the $2P_y$ state. Due to the line width of the exciton resonances, we are not able to resolve individual lines in Fig. 2.13, but rather observe a complex interplay of these contributions from different energies leading to the observed complex behavior in the integrated intensity. For the geometry, shown in Fig. 2.13 (b), we take into account the magneto-Stark and orbital Zeeman effects to model the SHG intensity dependency.

$$I^{\mathrm{SHG}}(B,E) \propto \mathrm{Abs}\left[\sum_{j=1}^{2}\sum_{i=1}^{3}\frac{1}{\mathcal{E}^i(B) - E - \imath\Gamma^i}(\chi^{\text{magneto-Stark}}(B) + \chi^{\text{orbital Zeeman}}(B))\right]^2 . \tag{2.48}$$

Here, the sum over j accounts for the upper and lower polariton branches, and the sum over i for the three mixed states $2S/2P_z/2P_y$. A model calculation for the strongest peak $2\hbar\omega = 3.4254$ eV assuming $\Gamma = 1.2$ meV and $\chi^{\text{magneto-Stark}} : \chi^{\text{orbital Zeeman}} \approx 100 : 1$ is able to reproduce the observed dependence quite well. Slight deviations are expected, since in the experiment the data was spectrally integrated. If the spin Zeeman effect is taken into account with$\Gamma = 1.2$ meV and $\chi^{\text{magneto-Stark}} : \chi^{\text{orbital Zeeman}} : \chi^{\text{spin Zeeman}} \approx 100 : 1 : 1$ in Eq. (2.48), the model calculations lead to a dependence with a shoulder shown in Fig. 2.13 (c).

2.9 SHG in Crossed Electric and Magnetic Fields

Electric fields are another promising option for the SHG spectroscopy. In contrast to a magnetic field of even parity, the electric field is of odd parity and expected to mix exciton wave functions of opposite parity. Furthermore, a static electric field should enhance for parallel or compensate for antiparallel orientation the effective electric field due to the magneto-Stark effect; see remark to Eq. (2.28)[5].

To obtain a preferably homogeneous electric field inside the sample, gold contacts on a titanium basis are thermally evaporated onto the ZnO edges, and the brazen contacts of the custom sample holder are attached with very little pressure. Low resistivity and photoconductivity made these experiments extremely challenging. Best results were obtained for the strongly Lithium-doped ZnO sample EN73.2.

2.9.1 Experimental Results

Fig. 2.18 (b) demonstrates the effect of a static electric field on an SHG spectrum in bulk ZnO. In the absence of an electric field residual SHG signals ($\sim 1\%$ of previously discussed crystallographic amplitudes) are caused by the custom sample holder. The electrical contacts, which were applied with very small pressure to the sample probably induce small strains. The presence of an electric field perpendicular to the z-axis (here $\mathbf{E} \parallel \mathbf{y} \perp \mathbf{k} \parallel \mathbf{z}$) induces further SHG signals. Note that the electric field strength inside the crystal has to be corrected for the static dielectric permittivity perpendicular to the hexagonal z-axis $\epsilon^{\perp} = 7.40$ [54]. When electric and magnetic fields are applied simultaneously and perpendicular to each other the effect of the electric field is more visible. Their interference is readily illustrated in Fig. 2.18 (a). The inset shows that the SHG amplitude is increased for $\mathbf{E} \uparrow\uparrow (\mathbf{k} \times \mathbf{B})$ and decreased for $\mathbf{E} \downarrow\uparrow (\mathbf{k} \times \mathbf{B})$. On the other hand, the electric field does not change the rotational anisotropies. The resistivity measured drops about three orders of magnitude for $2\hbar\omega$ reaching the energies of $2P_{x,y}(A, B)$ excitons. After switching off the laser, the system relaxes within seconds.

2.9.2 Discussion

To verify the magneto-Stark effect as dominant source of the observed SHG signals, it is instructive to discuss a joint action of external magnetic and electric fields. The developed theory predicts that an external electric field produces the same type of symmetry breaking as the effective electric field induced by an external

[5] The Hamiltonian (2.28) can take into account effects of a static electric field E_y as well, when E_{eff} is replaced by $E_{\text{eff}} \pm E_y$. The $\pm$ sign shows their relative alignment; parallel and antiparallel, respectively.

magnetic field. This is proven by the fact that the anisotropy of magnetic-field-induced signals is not changed by an additionally applied electric field. Nevertheless, the applied electric field acts experimentally very differently in comparison to the application of an magnetic field. The effective electric field acts on exciton levels only, whereas the electric field creates an electric potential throughout the crystal. Figure 2.18 (b) shows that an electric field of 550 V/cm has only a weak effect. The interference of its impact with the effective electric field induced by a magnetic field of 1 T shows that the electric field has indeed a surprisingly small contribution. The magnitude of the effective electric field can be estimated as $E_{\text{eff}} = \frac{\hbar}{M_{\text{exc}}} k_{\text{exc}} B_x$. The theoretical estimation of the exciton translation mass in ZnO is about $3m_0$ [49] and $k_{\text{exc}} = nE_{\text{exc}}/\hbar c \approx 0.03$ nm^{-1} for $E_{\text{exc}} = 3.425$ eV and respective refractive index $n \approx 1.97$ [53, 54]. Thus, $E_{\text{eff}} \approx 12$ V/cm for a field of 1 T. Consequently, $a = \frac{1}{12[\text{V/cm}]\epsilon_\perp} \approx 1.13 \times 10^{-2}$ T/V, where $\epsilon_\perp$ is the relative dielectric permittivity) would be the expected value for the fitting function $I^{2\omega} \propto (\pm B \pm aE)^2$. Instead the best fit of the data, shown in the inset of Fig. 2.18 (a), is achieved for a value that is 50 times smaller. Resistivity measurements shown that the incident laser beam reduces the sample resistivity enormously (several orders of magnitude), when the doubled photon energy $2\hbar\omega$ comes close to the $2P$ exciton states, see Fig. 2.18 (c). As the resistivity is not instantaneously restored when the laser is switched off, we assume that carriers become trapped in deep centers. We suggest that the screening of the external field by these carriers is responsible for the observed discrepancy.

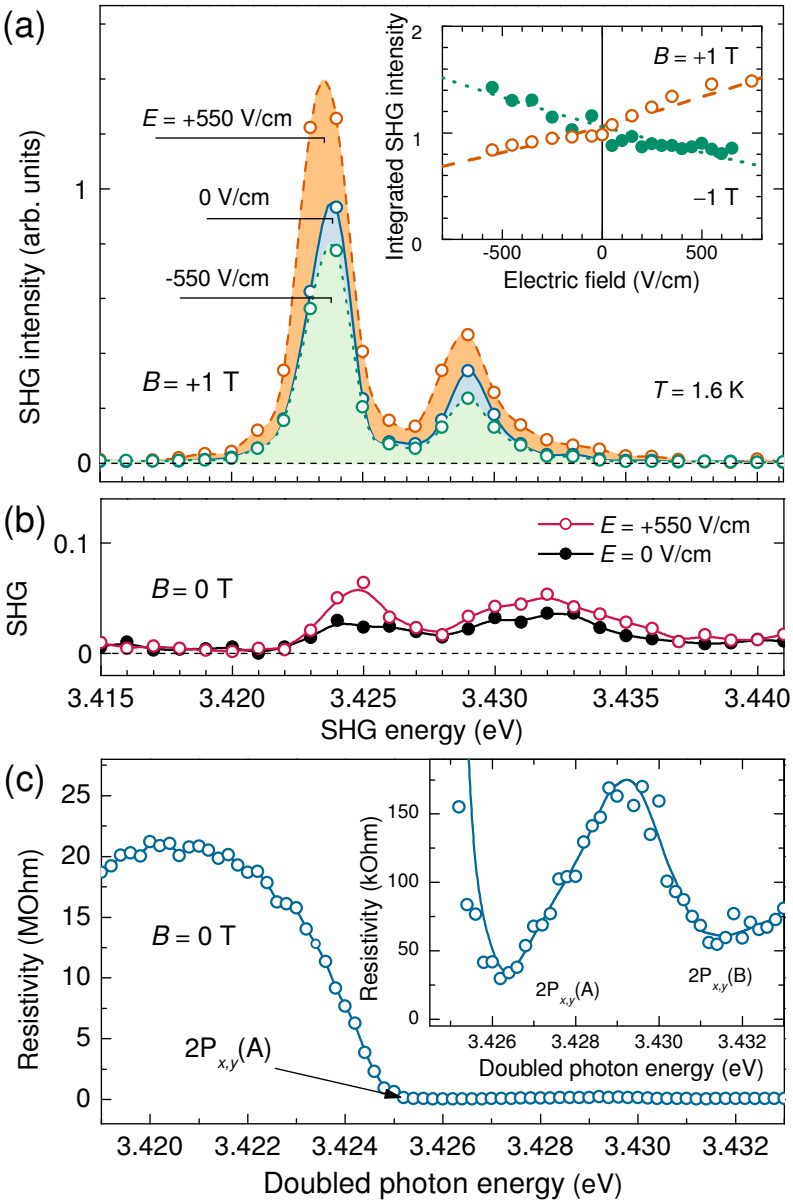

Figure 2.18: (a) SHG spectra in the range of $2S/2P(A,B)$ excitons of ZnO in electric and magnetic fields with $\mathbf{E}^{2\omega} \parallel \mathbf{E}^{\omega} \parallel \mathbf{E} \perp \mathbf{B}$ measured at $B = \pm 1$ T, $-550 \leq E \leq +550$ V/cm, and $T = 1.6$ K. An applied electric field corresponds to $E_y/\epsilon^{\perp}$ inside the crystal. Inset gives the integrated intensity for $3.417 - 3.438$ eV as a function of the electric field at $B = +1$ and -1 T illustrating the interplay of magnetic and electric field. Symbols are experimental data and lines show fits giving $I^{2\omega} \propto \left(\pm B + 2.5 \times 10.4^{-4} E\right)^2$. (b) Electric-field-induced SHG spectrum in the range of $2S/2P(A,B)$ excitons. Red line demonstrates the electric field effect. Black line shows residual crystallographic signals observed only for the custom sample holder. Intensity is increased by a factor of 4 compared to (a). (c) Measured resistivity of the ZnO sample at $B = 0$ T. Inset magnifies the $2P(A,B)$ exciton region by a factor of $\sim 10^3$.

2.10 Temperature Dependence of SHG

Figure 2.19 compares the crystallographic SHG intensities $I^{2\omega}$ at low 1.6 K and high 128 K temperatures. While the off-resonant signal is stable, the resonant signals of excitons show a strong decrease with rising temperature. A closer look at the detailed evolutions of the peak intensities shows that all $1S$ states and the X-line decrease slower than the $2P_{x,y}(A)$ states; compare results shown in Fig. 2.20 (a). At the same time, the full width at a half maximum of the $2P_{x,y}(A)$ line increases much faster than those of the $1S_L(C)$ state and the X-line; see Fig. 2.20 (b). As the induced signals show a similar behavior, we conclude that the signal decays are rather independent of the underlying mechanism. The temperature dependence of the integrated SHG intensity can be qualitatively understood in a simple consideration. Eq. (2.39) shows that the susceptibility depends inverse linear on the exciton damping Γ_{exc}. This damping consists of the inhomogeneous and the homogeneous broadening of the exciton. The inhomogeneous broadening in the studied sample does not exceed 1 meV, which is seen in Fig. 2.10 (a), where the line width is limited by the spectral width of the laser. Therefore, the exciton line width at temperatures $\leq 10-20$ K is controlled by the homogeneous broadening due to scattering by acoustic phonons. A process which is more likely for the $n = 2$ states than for the $n = 1$ states. The SHG peak intensity, proportional to the susceptibility, then depends inverse quadratically on the line width $I^{2\omega} \propto \Gamma_{\text{exc}}^{-2}$. The presented dependencies are spectral integrated, which gives in principle a multiplication with the line width leading to the integrated SHG being proportional to Γ_{exc}^{-1}. In contrast, the crystallographic SHG signal measured in the nonresonance region is stable with increasing temperature; compare blue and red curve in the lower energy region in Fig. 2.19.

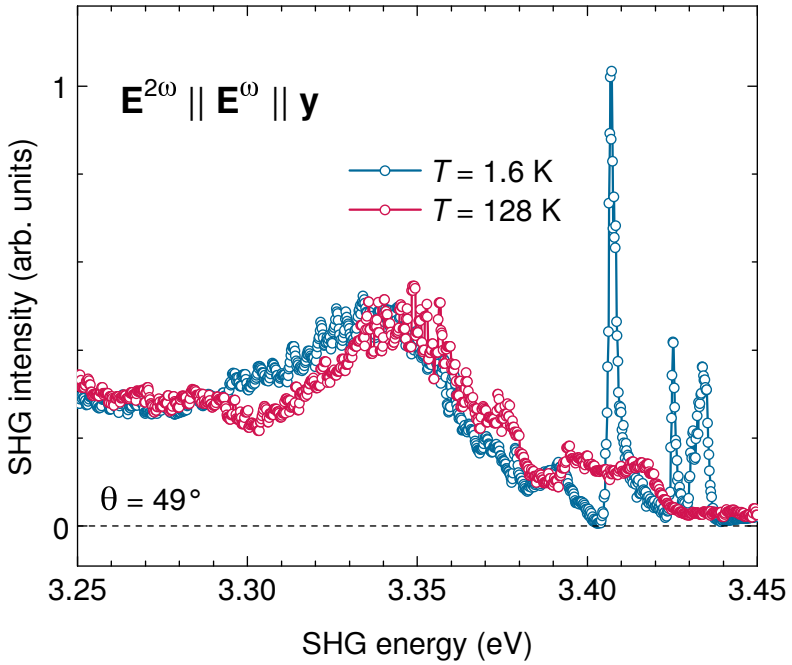

Figure 2.19: Wide range crystallographic SHG spectra at low (blue) and high (red) temperatures measured for $\mathbf{E}^{2\omega} \parallel \mathbf{E}^{\omega} \parallel \mathbf{y}$ and $\theta = 49°$.

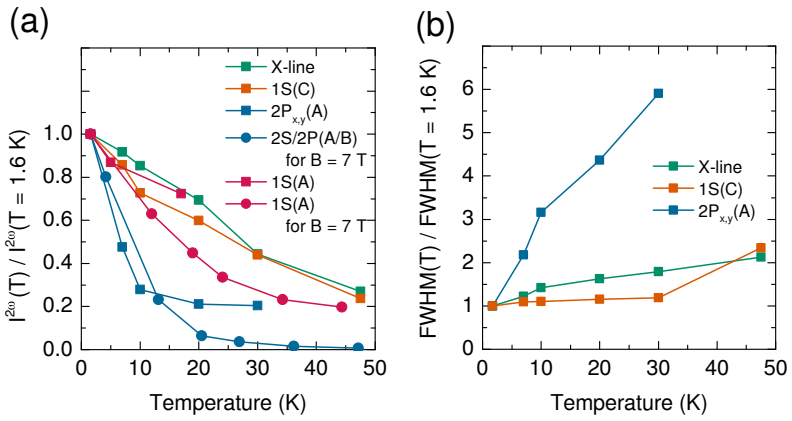

Figure 2.20: Normalized (a) intensity and (b) FWHM of measured SHG peaks versus temperature. Blue color shows $n = 2$ states, red gives $1S(A)$ states, orange represents $1S(C)$, and green shows X-line.

3 Third Harmonic Generation in Magnetic Semiconductors EuTe and EuSe

Applications of the rare earth compounds europium chalcogenides (EuX, X=O, S, Se, Te) are specialized and mainly based on their phosphorescence properties. Europium oxide is commonly used for red or blue colors in televisions and lamps, or in addition with other phosphors to gain different types of white light. Latest scientific interest in this material class is motivated by their proposed value for magneto optic devices.

Recently, spin induced SHG contributions were discovered, that are governed by the spin structures in magnetic EuX [14,15]. Their second order susceptibilities dictated by magnetic dipole transitions, which are usually low in efficiency. In contrast, ED transitions of high efficiency are allowed for THG processes. Thus, it is convenient to investigate the electronic and spin structure of centrosymmetric EuX by means of THG spectroscopy. In Ref. [57] preliminary data is presented, where THG signals could be linked to the $5d$ conduction bands by their energy position, and influences of magnetic fields were reported.

In the next chapter new experimental results are presented, that allow the separation of crystallographic and magnetic field induced THG contributions. Signals in EuTe are discussed on the basis of a microscopic theory developed for THG in EuTe. The deduced interpretations are also transfered to the THG studies in EuSe, because the EuX have strong similarities in their electronic configurations. The THG studies in magnetic fields resolve various magnetic phases. In addition, the interference of crystallographic and magnetic field induced contributions to THG will be examined[1].

3.1 Band Structure and Electronic Configuration

EuX are magnetic semiconductor compounds. Their divalent Eu^{2+} and X^{2-} ions form centrosymmetric cubic rock salt structures; see Figure 3.1 (a). Each ion is

[1] The presented results are already published in Refs. [85] and [86].

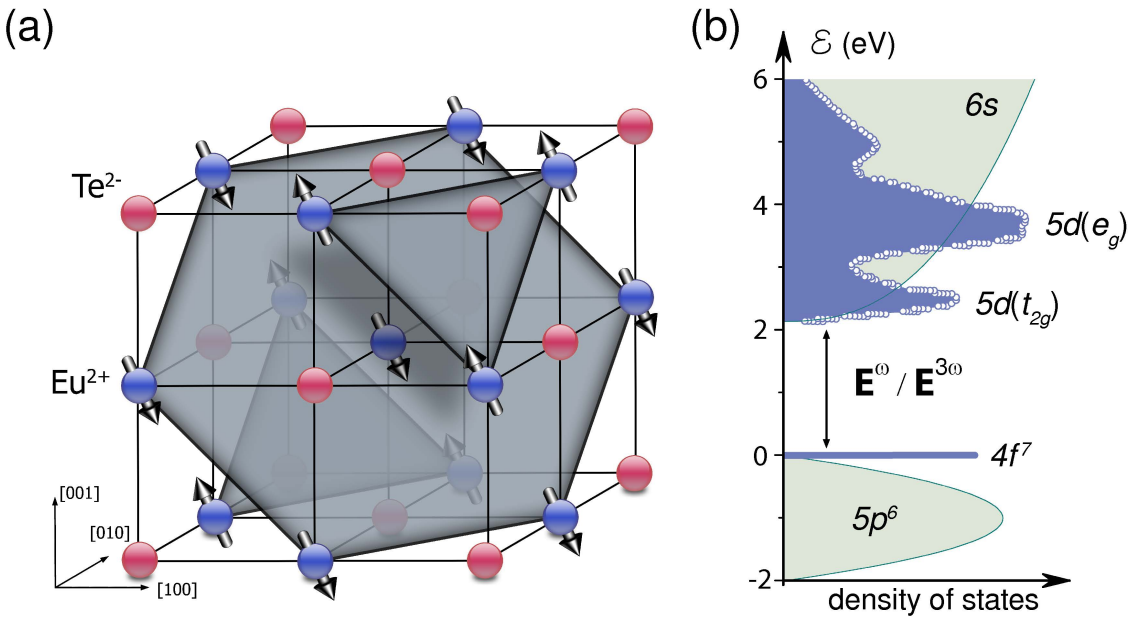

Figure 3.1: (a) Cubic crystal structure of EuX, exemplarily shown for EuTe. (b) Electronic structure of EuTe around the band gap at Γ point ($k = 0$). Circles represent measurements of the imaginary part of the dielectric function from Ref. [88]. Odd number photon transitions are allowed from $4f^7$ states to $5d$ bands, and forbidden to the $6s$ band.

surrounded by six of the other kind forming an octahedron. Lattice constants depend mainly on the group period of the chalcogen; values are $a_0 = 6.598$ Å for EuTe and $a_0 = 6.195$ Å for EuSe.

The direct band gap is formed by localized states, because of the strong ionic bonding. Figure 3.1 shows the energy scheme of EuTe, which is exemplary for all EuX. It its generally accepted [15, 88], that the $4f^7$ electrons and the empty $5d$ orbitals of Eu ions constitute the valence and conduction bands, respectively. The broad np orbitals of the chalcogen ($n = 2, 3, 4, 5$ for O, S, Se, Te) lie directly underneath the $4f^7$ states. The $6s$ orbitals of Eu^{2+} ions overlap energetically with the $5d$ orbitals, but their ED matrix elements from $4f^7$ states are zero and the $6s$ band can generally be neglected for the discussion of optical transitions in vicinity of the band gap. The strongly localized $4f^7$ states can be treated as atomic states. Their ground state has spin $S = 7/2$ denoted as $4f^7(^8S_{7/2})$. The 5_d orbitals are commonly treated by a tight-binding model [15]. The octahedral crystal field splits them into the sub bands $5d(t_{2g})$ and $5d(e_g)$.

One photon (Γ_4^-) and consequently odd number photon transitions from the odd parity $4f^7(^8S_{7/2})$ valence band states ($\Gamma_2^- \oplus \Gamma_4^- \oplus \Gamma_5^-$) to the even parity $5d(t_{2g}/e_g)$ bands (Γ_5^+/Γ_3^+) are generally allowed. Therefore, group theory anticipates THG contributions of electric dipole type.

3.2 Magnetic Properties

The magneto-optical properties of the europium chalcogenides are striking, and some of them are unmatched by any other magnetic semiconductor. When subject to an external magnetic field, EuTe exhibits a giant low-energy shift of 15 meV/T of the optical absorption threshold [89, 90]. The Faraday effect is also extraordinary large with Verdet constants as high as 10^6 deg/cm [91–96]. Due to the giant Faraday rotation EuX films can be applied for high resolution magneto-optical imaging of the flux distribution in superconductors [97].

The magnetic properties of the europium chalcogenides are determined by the large $S = 7/2$ spin of the $4f^7$ electrons in the ground state of the Eu^{2+} ions [89, 90, 98]. The EuX are classical Heisenberg magnets where the magnetic phase is governed by the competing exchange integrals of the nearest neighbor (NN) exchange J_1, which provides a ferromagnetic interaction, and the next-nearest neighbor (NNN) exchange J_2 providing an antiferromagnetic interaction. The resulting magnetic phase diagrams may include antiferromagnetic (AFM), ferrimagnetic (FIM), and ferromagnetic (FM) ordering, as well as a paramagnetic phase at elevated temperatures in EuTe and EuSe [90, 99]. The unique magnetic properties and complicated magnetic phase diagrams of EuX are caused by the varying ratios of the J_1 and J_2 integrals and by their competition with an external magnetic field.

EuTe

In EuTe the antiferromagnetic exchange integral J_2 is larger than the ferromagnetic exchange integral $\mid J_2 \mid > \mid J_1 \mid$ and the compound shows antiferromagnetic ordering of its spin sublattices below the Néel temperature $T_N = 9.58$ K [90]. Eu^{2+} spins align parallel within the (111) planes. Adjacent planes show alternating spin orientations [↑↓↑↓]. For lattice temperatures $T < 2$ K and magnetic fields exceeding $B_c' = 7.2$ T a high field paramagnetic phase is reached, where the magnetization is saturated and oriented along the magnetic field direction.

Below T_N the magnetic ordering in EuTe can be characterized by magnetic moments $\mathbf{m}_1$ and $\mathbf{m}_2$ of the two sublattices with $|m_1| = |m_2|$. To describe the magnetic behavior in magnetic fields the ferromagnetic vector $\mathbf{F} = \mathbf{m}_1 + \mathbf{m}_2$ and the antiferromagnetic vector $\mathbf{A} = \mathbf{m}_1 - \mathbf{m}_2$ are defined. An external magnetic field $\mathbf{B}$ induces a magnetization that is described by increasing $\mathbf{F}$.

EuSe

Ferromagnetic and antiferromagnetic exchange integrals J_1 and J_2 are of comparable magnitude in EuSe leading to several magnetic states; see Fig. 3.2. Such richness in possible magnetic phases is called metamagnetic. EuSe is antiferromagnetic below

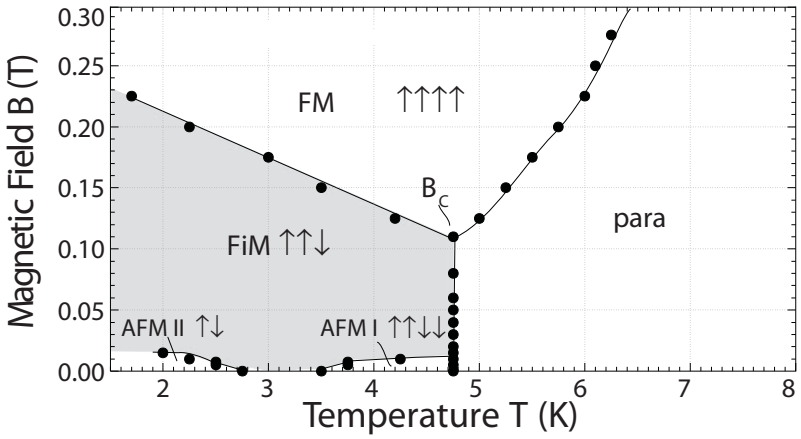

Figure 3.2: Magnetic phase diagram of metamagnetic EuSe taken from Ref. [99].

$T_{\mathrm{N}} = 4.6$ K with adjacent spin planes aligned as [↑↑↓↓]. From $T_C = 3.6$ K to 2.8 K the spin plane structure is ferrimagnetic [↑↑↓]. For temperatures lower than $T_{\mathrm{N}} = 2.8$ K another antiferromagnetic phase is found with the plane alignment [↑↓↑↓]. Already a weak magnetic field switches the two antiferromagnetic phases into a ferrimagnetic phase and the ferrimagnetic phase into a ferromagnetic phase. For a detailed discussion of its magnetic phases see Ref. [99]

3.3 Polarization Selection Rules

Figure 3.3 illustrates the measurement geometry $\mathbf{k}^{\omega} \parallel [111]$. Polarizer and analyzer are turned around the [111]-axis by the angle φ. A static magnetic field $\mathbf{B}$ will be applied only perpendicular to [111]. To account for possible sample tilting around the [111]-axis, the relative angle α is introduced. In the following, this measurement geometry is analyzed.

The face-centered-cubic crystal lattices of EuX belong to the point group $m\bar{3}m$. Group theoretical considerations yield four independent tensor components to their crystallographic third order optical susceptibility $\chi^{\mathrm{cryst}}_{ijkl}$ in the electric dipole approximation [21]:

$$\begin{aligned}
\underline{\chi_{xyyx}} &= \chi_{xzzx} = \chi_{yxxy} = \chi_{yzzy} = \chi_{zxxz} = \chi_{zyyz},\\
\underline{\chi_{xyxy}} &= \chi_{xzxz} = \chi_{yxyx} = \chi_{yzyz} = \chi_{zxzx} = \chi_{zyzy},\\
\underline{\chi_{xxyy}} &= \chi_{xxzz} = \chi_{yyxx} = \chi_{yyzz} = \chi_{zzxx} = \chi_{zzyy},\\
\underline{\chi_{xxxx}} &= \chi_{yyyy} = \chi_{zzzz}.
\end{aligned} \tag{3.1}$$

Incoming photons are indistinguishable and therefore the last three indices permute reducing the number of independent components to χ_{xxyy} and χ_{xxxx}. Crystallographic contributions to the third order nonlinear optical polarization $\mathbf{P}^{3\omega}_i$ are (the

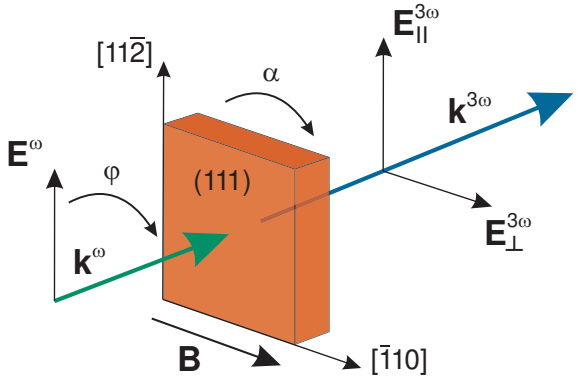

Figure 3.3: A sketch demonstrating the measurement geometry: φ is the turning angle of $\mathbf{E}^{\omega}$ around $\mathbf{k}$. Measurements are performed either for $\mathbf{E}^{3\omega} \parallel \mathbf{E}^{\omega}$ or $\mathbf{E}^{3\omega} \perp \mathbf{E}^{\omega}$. Static magnetic fields are perpendicular to the propagation direction of the light $\mathbf{B} \perp \mathbf{k} \parallel [111]$.

notation is explained in Sec. 2.3)

$$P_{\parallel,\,i}^{3\omega} = \frac{1}{2}(\chi_{xxxx}^{\text{cryst}} + 3\chi_{xxyy}^{\text{cryst}}). \tag{3.2}$$

$$P_{\perp,\,i}^{3\omega} = 0. \tag{3.3}$$

Thus, no polarization anisotropy is expected for $I_{\parallel}^{3\omega}$ and in the crossed geometry crystallographic signals vanish.

Application of a static magnetic field $\mathbf{B} \perp [111]$ reduces the symmetry and new contributions $\chi_{ijklm}^{\text{ind}}$ to the third order nonlinear optical polarization $\mathbf{P}^{3\omega}$ are induced:

$$\begin{aligned}
\underline{\chi_{zyyxy}} &= \chi_{xzzyz} = -\chi_{zxxyx} = \chi_{yxxzx} = -\chi_{yzzxz} = -\chi_{xyyzy},\\
\underline{\chi_{zyyyx}} &= \chi_{xzzzy} = -\chi_{zxxxy} = \chi_{yxxxz} = -\chi_{yzzzx} = -\chi_{xyyyz},\\
\underline{\chi_{zzzyx}} &= \chi_{xxxzy} = -\chi_{zzzxy} = \chi_{yyyxz} = -\chi_{yyyzx} = -\chi_{xxxyz}.
\end{aligned} \tag{3.4}$$

The induced polarization $P_i^{3\omega,\ \text{ind}}$ is then given by

$$P_i^{3\omega,\ \text{ind}} = \chi_{ijklm}^{\text{ind}} E_j^{\omega} E_k^{\omega} E_l^{\omega} M_m. \tag{3.5}$$

Here, $\mathbf{M}$ is the component of the magnetization in direction of the magnetic field $\mathbf{B}$. The consequent anisotropies of the magnetic field induced THG are expected to follow

$$P_{i,\parallel}^{3\omega,\ \text{ind}} = \frac{\sqrt{2}}{12}(\chi_{zzzyx} - \chi_{zyyyx})[\cos(2\varphi - 3\alpha) + \cos(4\varphi - 3\alpha)], \tag{3.6}$$

$$\begin{aligned}
P_{i,\perp}^{3\omega,\ \text{ind}} = \frac{\sqrt{2}}{12}&[(2\chi_{zyyxy} + \chi_{zzzyx} + \chi_{zyyyx})\sin(2\varphi - 3\alpha)\\
&+(\chi_{zzzyx} - \chi_{zyyyx})\sin(4\varphi - 3\alpha)].
\end{aligned} \tag{3.7}$$

In the case crystallographic and induced contributions are present at the same time, the interference has to be taken into account according to Eq. (1.19)

$$I^{3\omega} \propto |\mathbf{P}^{3\omega,\mathrm{cryst}}|^2 + |\mathbf{P}^{3\omega,\mathrm{ind}}|^2 \pm 2|\mathbf{P}^{3\omega,\mathrm{cryst}}||\mathbf{P}^{3\omega,\mathrm{ind}}| \cos\theta, \tag{3.8}$$

θ is the relative phase between crystallographic and induced contributions.

3.4 Samples

Several EuTe and EuSe samples grown by molecular beam epitaxy on BaF_2 substrates in [111] direction were investigated [100,101]. Samples of the same kind show the same qualitative results, but the presented measurements are given for one sample of each kind only: the 1μm layer EuTe 9002 and the 0.5μm layer EuSe Va495. Samples are capped with a 40 nm protection layer BaF_2 to prevent oxidation. BaF_2 is transparent in the region of interest, and the substrates did not show any THG. Different thermal expansion coefficients and the lattice mismatch between sample structures and substrate (EuTe 6.598 Å, EuSe 6.195 Å, BaF_2 6.200 Å) leads to a small trigonal strain in the [111] direction for EuTe, whereas no visible influence is expected for EuSe structures.

3.5 THG in EuTe

In this section, the crystallographic contributions to THG are presented, first. Second, pure magnetic-field-induced contributions are discussed. Thirdly, the interference of crystallographic and induced contributions is analyzed.

3.5.1 Crystallographic Contributions to $\chi^{(3)}$

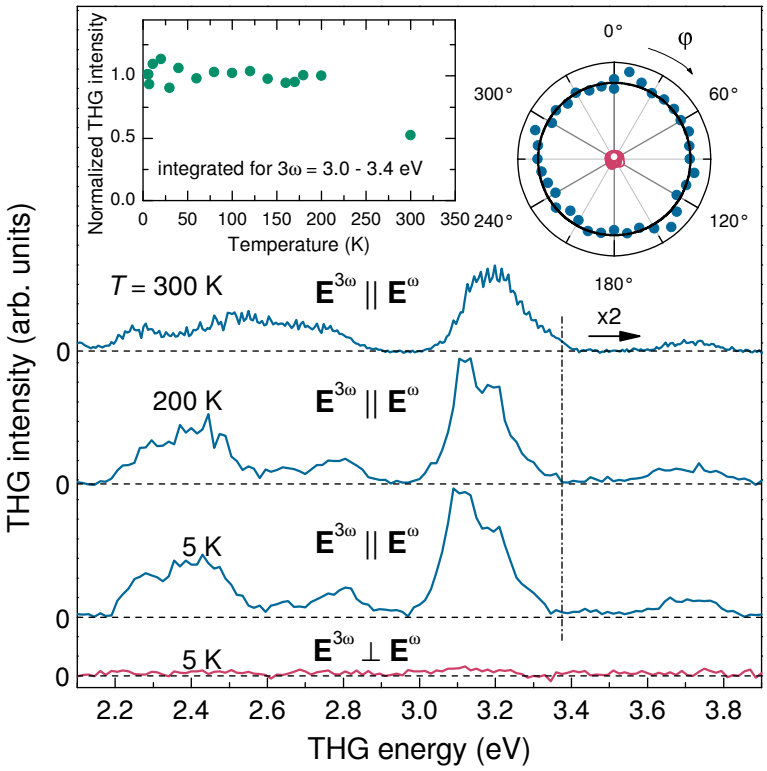

Figure 3.4: Wide-range crystallographic THG spectra of EuTe for $\mathbf{E}^{3\omega} \parallel \mathbf{E}^{\omega}$ measured at $T = 5, 200$, and 300 K (blue data). The high-energy range $\mathcal{E} \geq 3.4$ eV is enhanced by a factor of 2. Left inset shows the temperature dependence of the integrated THG intensity $(3.0 - 3.4$ eV). Right inset illustrates the angular distribution of THG light polarization exemplarily for the strongest peak $3\hbar\omega = 3.15$ eV at 5 K. The line gives the fitted value in accordance with Eq. (3.2). The red data demonstrates for $T = 5$ K that no THG is observed for $\mathbf{E}^{3\omega} \perp \mathbf{E}^{\omega}$.

The propagation of third-harmonic-light waves is allowed in EuTe and several features over a broad spectral range $(2.1 - 3.9$ eV) are observed in its THG spectra; see Figure 3.4. Given spectra are recorded at $T = 5$, 200 and 300 K for $\mathbf{E}^{3\omega} \parallel \mathbf{E}^{\omega}$. These spectra do not show a significant change with increasing temperature; illustrated by the left inset in Figure 3.4. This stability emphasizes that harmonic generation

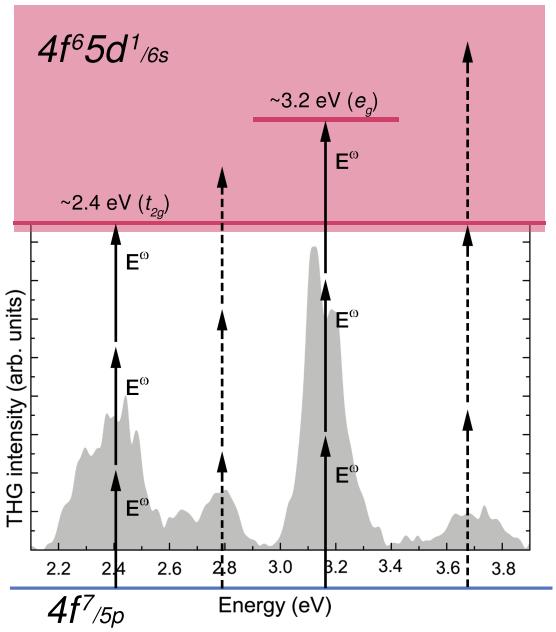

Figure 3.5: A visualization of identified THG processes in EuTe. The observed features around 2.4 eV and 3.15 eV are clearly assigned to the $5d$ subbands. Two more THG bands are observed around 2.75 eV and 3.7 eV. The background displays the $T = 200$ K spectrum from Fig. 3.4.

spectroscopy of band to band transitions is applicable far above liquid-nitrogen temperature and even at room temperature, where no sophisticated cryogenic environments are required. The electronic structure of EuTe leads to four major bands around 2.4, 2.75, 3.15, and 3.7 eV in its THG spectrum. Figure 3.5 schematically draws assignments. The first and lowest energy band around 2.4 eV corresponds to the optical transitions $4f^7 \rightarrow 4f^6 5d^1(t_{2g})$. These transitions are also responsible for observed SHG and absorption spectra [15,102]. The second band around 2.75 eV lies in between the spectral ranges of optical transitions to the two lowest conduction bands $5d(t_{2g}/e_g)$. Possible explanations are that excitonic states below the band gap serve as resonant intermediate states, or that the feature is a consequence of the constructive interference of signals from both $5d$ bands. The band around 3.15 eV is associated to the $4f^7 \rightarrow 4f^6 5d^1(e_g)$ transitions. The high energy band around 3.7 eV may be assigned most likely to a four-photon process in which the $4f^6 5d^1(t_{2g})$ states act as resonant intermediate states, and whose final state lying in the continuum of the $5d/6s$ states is nonresonant.

All bands show isotropic rotational diagrams for $I_{\parallel}^{3\omega}$: $\mathbf{E}^{3\omega} \parallel \mathbf{E}^{\omega}$. The right inset of Fig. 3.4 illustrates such a diagram exemplarily for the strongest signals at $3\hbar\omega = 3.15$ eV. The isotropic third-harmonic-polarization emission is characteristic for the crystallographic contribution of (111) oriented EuX; see Eq. (3.2).

No crystallographic signals are detected for crossed incoming and outgoing polariza-

tions $\mathbf{E}^{3\omega} \perp \mathbf{E}^{\omega}$ exemplified by the red data in Fig. 3.4. This is in accordance with the symmetry considerations for crystallographic contributions given in Eq. (3.3).

3.5.2 Magnetic-Field Induced-Contributions to $\chi^{(3)}$

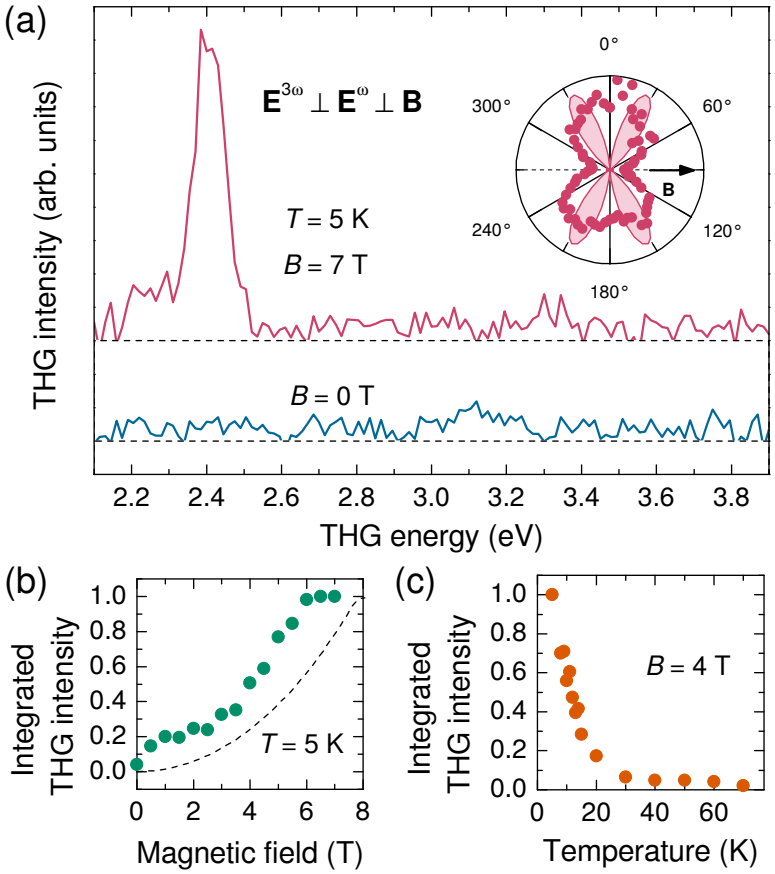

Figure 3.6: Magnetic-field-induced THG signals in EuTe measured for $\mathbf{E}^{3\omega} \perp \mathbf{E}^{\omega} \perp \mathbf{B}$. (a) The wide-range THG spectra measured at $B = 7$ T and for $T = 5$ K. Inset shows the rotational anisotropy for the observed induced peak at $3\hbar\omega = 2.4$ eV. Points represent experimental data and the line shows the model anisotropy according to Eq. (3.7). (c) Magnetic field dependence of the integrated THG intensity for the observed peak ($2.2 - 2.5$ eV) at $T = 5$ K. Points represent experimental data and the dashed line gives the squared magnetization $\mathbf{M}^2(B)$ taken from Ref. [103]. (c) Temperature dependence of the integrated THG intensity for the peak $2.2 - 2.5$ eV at $B = 4$ T.

The crossed geometry $\mathbf{E}^{3\omega} \perp \mathbf{E}^{\omega}$, where crystallographic signals are absent, is chosen for the examination of induced contributions to $\chi^{(3)}$ of EuTe. Figure 3.6 displays respective results: (a) In the wide spectral range $2.1 - 3.9$ eV, one feature around 2.4 eV is observed, which was previously linked to the transitions $4f^7 \rightarrow 4f^6 5d^1(e_g)$. The inset displays its rotational anisotropy for $I_{\perp}^{3\omega}$. The shape with its minima at

the axis of the magnetic field is dominated by the predicted shape given in Eq. (3.7). The deviations might stem from either not pure band function symmetries, or the interference with higher order contributions. (b) The integrated induced THG intensity of EuTe follows in principle its squared magnetization; compare data points and dashed line in Fig. 3.6 (b). In lower fields, the signals scale with B^2 and, in higher fields $B > 6$ T, a saturation is reached. (c) The induced signals decrease significantly with increasing temperature and vanish for $T > 30$ K.

The distinct polarization anisotropy, the strong dependence on temperature, and the clear correlation to the magnetization allow the separation of these magnetic-field-induced signals from the reported crystallographic signals. Further, these induced signals can be linked to the ferromagnetic component of the magnetization, like it was also done for SHG [15].

3.5.3 Interference of Crystallographic and Induced Signals

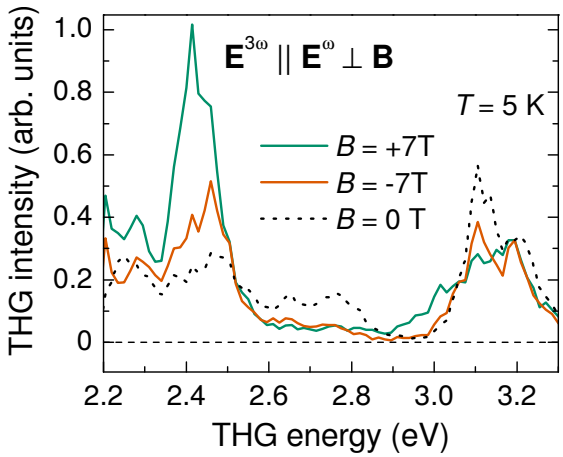

Figure 3.7: A direct comparison of THG spectra of EuTe measured at $B = \pm 7$ T and 0 T in the energy range $2.2 - 3.3$ eV. All spectra are measured for $\mathbf{E}^{3\omega} \parallel \mathbf{E}^{\omega}$ at $T = 5$ K. The magnetic-field $\mathbf{B} \perp \mathbf{k}$ is applied perpendicular to $E^{3\omega/\omega}$.

It has been shown in the past that allegedly small contributions are enhanced and unveiled when interfering with stronger contributions; see, e.g., Ref. [15]. In the configuration $\mathbf{E}^{3\omega} \parallel \mathbf{E}^{\omega} \perp \mathbf{B}$ crystallographic and magnetic field induced contributions are allowed in EuX. Figure 3.7 demonstrates their interference. Switching the magnetic field direction from $B = -7$ T to $+7$ T doubles the peak intensity around $3\hbar\omega \approx 2.4$ eV. Apparently, this switch corresponds to a $\theta = \pi$ phase shift in Eq. (3.8) changing the destructive interference to be constructive.

More detailed measurements are presented in Fig. 3.8. The comparison of wide range spectra measured at different magnetic fields in the configuration $\mathbf{E}^{3\omega} \parallel \mathbf{E}^{\omega} \perp \mathbf{B}$ shows, on the one hand, the strong influence of the observed magnetic field induced

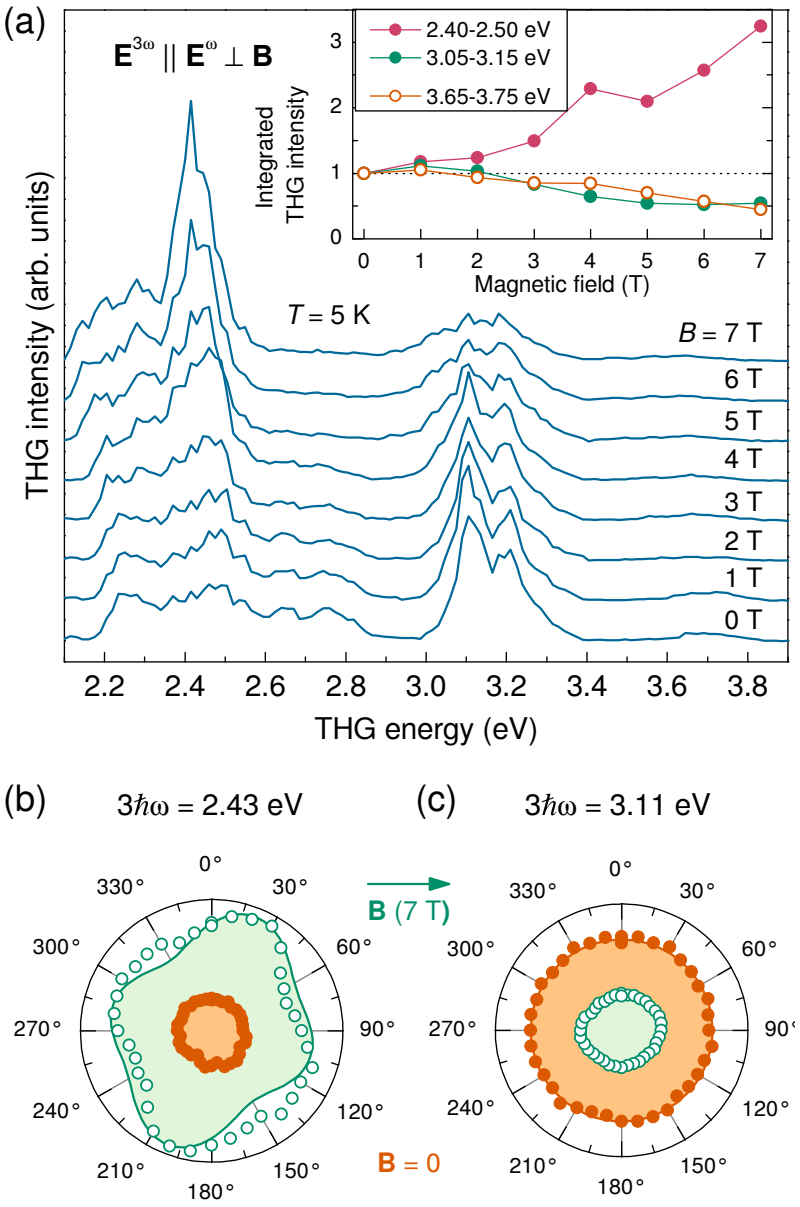

Figure 3.8: (a) Wide range THG spectra of EuTe measured for $\mathbf{E}^{3\omega} \parallel \mathbf{E}^{\omega} \perp \mathbf{B}$ in various magnetic fields $B \leq 7$ T at $T = 5$ K. The inset illustrates the magnetic field dependence of the integrated THG intensity for three different bands. (b) and (c) display rotational diagrams for $I_{\parallel}^{3\omega}$ at $3\hbar\omega = 2.43$ eV and 3.11 eV, respectively. Green data is measured at $B = 7$ T and orange data at $B = 0$ T (green data is enhanced by a factor of 4 for $3\hbar\omega$). The filled areas give fittings following Eqs. (3.2) and (3.6), while in magnetic fields their interference is considered according to Eq. (1.19).

signals for the lowest conduction band and, on the other hand, discloses interference effects for other bands as well. The inset in Fig. 3.8 (a) shows the integrated THG intensity for different bands demonstrating the interference effects not only for the 2.4 eV peak, but also for the bands 3.05−3.15 eV and 3.65−3.75 eV. Although, mod-

ifications of the signal strength is much weaker for the high energy bands, they allow to conclude magnetic field induced signals in these regions as well. Further proof for the interference of crystallographic and magnetic field induced signals is given by the induced anisotropy of emitted third harmonic light polarization. Figs. 3.8 (b) and (c) display rotational diagrams for $3\hbar\omega = 2.43$ eV and 3.11 eV. From $B = 0$ T to 7 T the isotropic shape of pure crystallographic THG becomes distorted and can then be modeled by the interference (Eqs. (1.19) and (3.8)) of crystallographic (Eq. (3.2)) and magnetic field induced (Eq. (3.6)) contributions.

3.5.4 Discussion

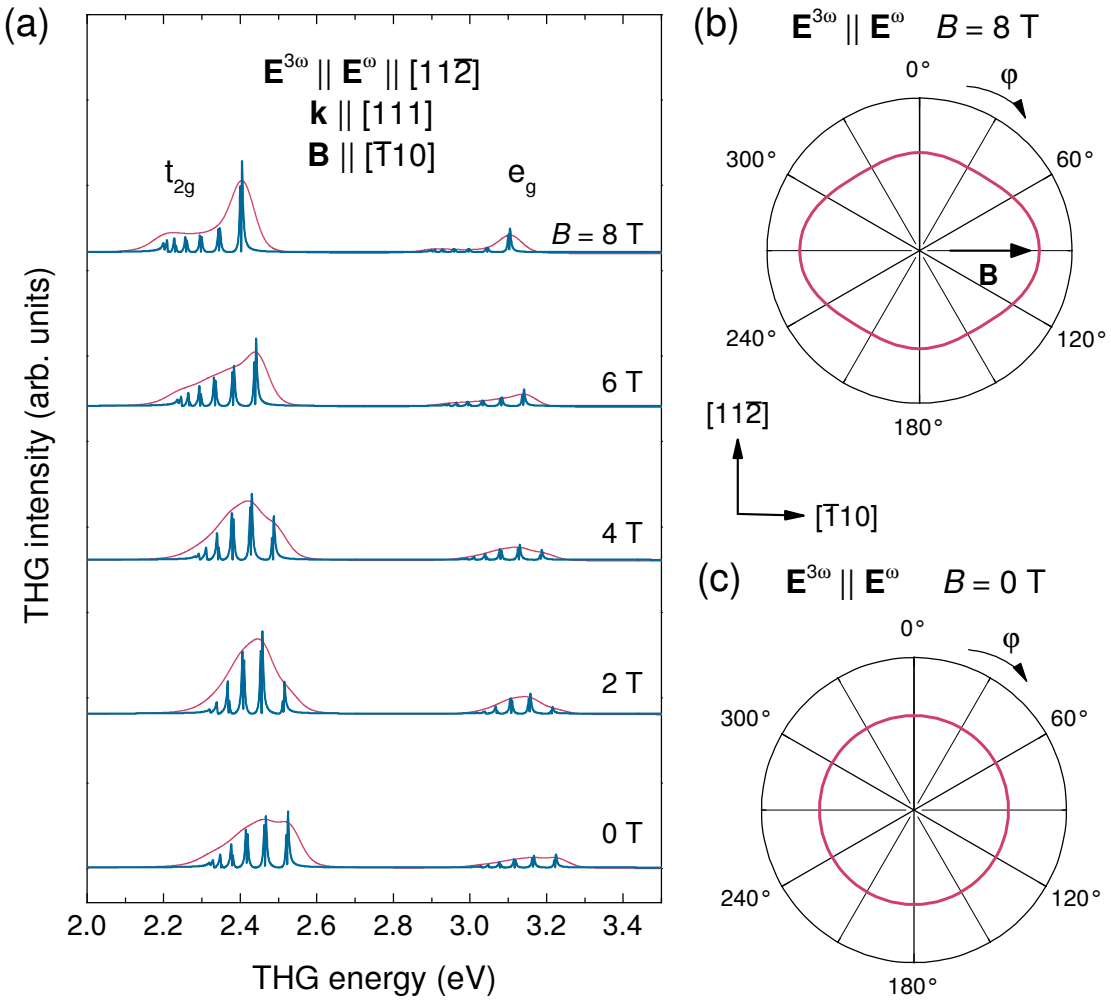

Figure 3.9: The results of model calculations taken from [85]. (a) Theoretically estimated THG spectra for $\mathbf{E}^{3\omega} \parallel \mathbf{E}^{\omega} \perp \mathbf{B}$, $\mathbf{E}^{3\omega/\omega} \parallel [11\bar{2}]$, $\mathbf{k} \parallel [111]$, and $\mathbf{B} \parallel [\bar{1}10]$ for $B = 0, 2, 4, 6$, and 8 T. (b) and (c) display theoretically estimated rotational anisotropies with and without a magnetic field.

In the course of collaboration Prof. A. B. Henriques has performed model calculations to theoretically estimate spectra and rotational anisotropies of THG in EuTe for magnetic fields 0 T$\leq B \leq$ 8 T. Figure 3.9 summarizes parts of his results taken from [85]. Appendix 5.3 briefly summarizes the main ideas and limits of the model; for more detail descriptions see Refs. [85].

A comparison of calculated (Fig. 3.9) and measured (Fig. 3.8) THG spectra underlines that the emission around 2.4 eV and 3.15 eV is governed by the optical transitions $4f^7 \rightarrow 4f^6 5d^1(t_{2g})$ and $4f^7 \rightarrow 4f^6 5d^1(e_g)$. The model based on these transitions reproduces the redshift and the narrowing of the lower energy THG peak with increasing magnetic field strength. The induced anisotropy of third harmonic light polarization by a static magnetic field is predicted by the model as well; compare Figs. 3.9 (b), (c) and 3.8 (b), whereas no anisotropy is predicted and measured without a magnetic field.

In contrast to the good agreement between the model and the experimental results around 2.4 eV, the theoretical description of the higher energy band shows some discrepancies. Calculations always predict smaller THG signals for the e_g band than for the t_{2g} band. In contrast, the measured THG signals for e_g band are larger than for the t_{2g} band in low magnetic fields. They are smaller only in high magnetic fields. The theory is based on tight-binding approximations being more appropriate for lower energetic states. Further, only the $^8S_{7/2}$ and $^7F_{JM}X$ electronic levels with identical broadening are taken into account by the model. Although these approximations are apparently acceptable to describe the lower energy conduction band, higher energy states need a more advanced model.

The model also lacks the description of interference. It does not separate crystallographic and induced contributions. Despite these limitations, the theoretical model describes reasonably well many of the observed THG characteristics and consolidates the conclusion, that THG in EuTe is associated with its direct band gap states.

Comparison of THG and SHG Spectra

Figure 3.10 (a) displays THG and SHG spectra measured on the same EuTe sample for $B = 7$ T at $T = 5$ K. Both measurements are performed in the configuration $\mathbf{E}^{3\omega/2\omega} \parallel \mathbf{E} \perp \mathbf{B}$ for maximum signals. The ED allowed four photon process THG is much more efficient than the MD contributions to SHG despite its higher order susceptibility. Thus, the dominant emission bands are more pronounced and visible in the THG spectra showing a better signal to noise ratio. In addition, with THG spectroscopy higher energy bands are uncovered. In centrosymmetric EuTe, THG spectroscopy reflects the electronic configuration even without a magnetic field. Nevertheless, the importance of spin induced contributions to THG is reported as well.

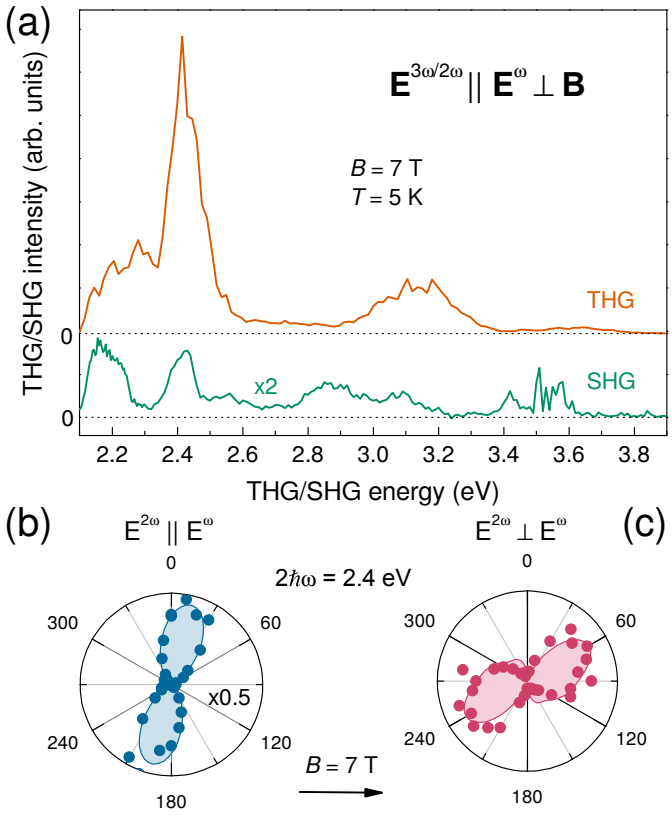

Figure 3.10: (a) THG and SHG spectra of EuTe measured for $\mathbf{E}^{3\omega/2\omega} \parallel \mathbf{E} \perp \mathbf{B}$ at $B =$ T and $T = 5$ K. The SHG signals are enhanced by a factor of 2. (b, c) Rotational anisotropies of the second harmonic light polarization shown exemplarily for $2\hbar\omega = 2.4$ eV. Points resemble measurements and areas give fittings following Eqs. (12)-(16) from [15].

Theory predicts zero field contribution stemming from the antiferromagentic ordering of the spin lattices. Extensive temperature dependency measurements did not resolve any results pointing at pure antiferromagnetic contributions. These signals would be expected to vanish for $T > T_{\mathrm{N}}$ in the paramagnetic phase abruptly. But no change in intensity could be linked to this temperature. Therefore, the theoretical model is able to give a qualitative understanding, but it is insufficient to draw deeper conclusions on quantitative mechanisms.

3.6 THG in EuSe

In this chapter, the THG in the metamagnetic EuSe will be discussed. THG spectroscopy is able to resolve the various magnetic phases of EuSe as well as it was done with SHG spectroscopy [15], but the dominant features of its electronic structure are already resolved without magnetic fields, which was not within the reach of SHG spectroscopy.

3.6.1 Crystallographic Contributions to $\chi^{(3)}$

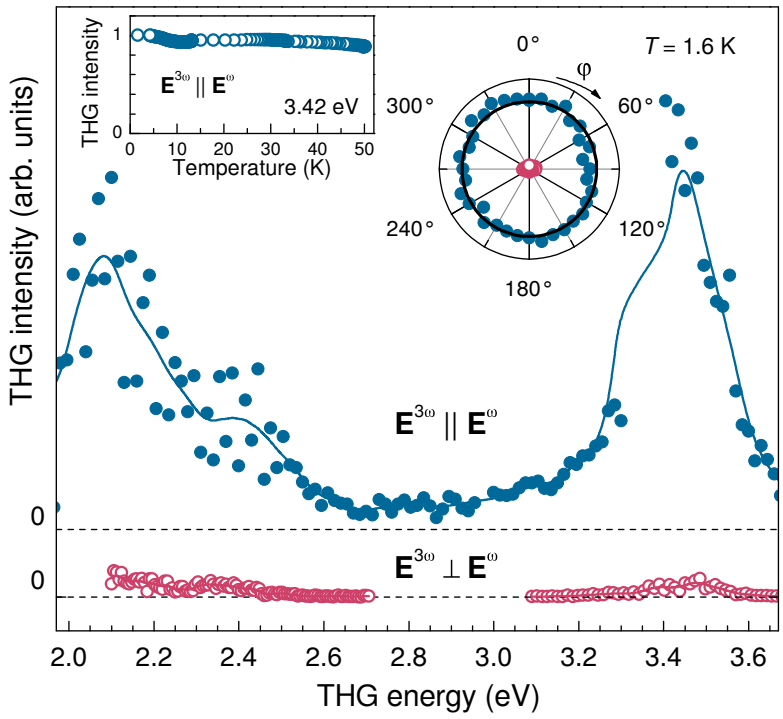

Figure 3.11: Wide-range crystallographic THG spectra of EuSe for $\mathbf{E}^{3\omega} \parallel \mathbf{E}^{\omega}$ and $\mathbf{E}^{3\omega} \perp \mathbf{E}^{\omega}$ measured at $T = 1.6$ K (blue and red data). Solid lines are guides for the eye. Left inset shows the temperature dependence of the THG intensity and right inset illustrates the angular distribution of the THG light polarization; both are exemplarily shown for $3\hbar\omega = 3.24$ eV. The line gives the fitted value in accordance with Eq. 3.2.

The wide-range crystallographic THG spectra of EuSe given in Fig. 3.11 show the same principle features as that of EuTe displayed in Fig. 3.4. In the parallel configuration $\mathbf{E}^{3\omega} \parallel \mathbf{E}^{\omega}$ the THG signals can be linked to transitions from $4f^7$ states to the $5d(t_{2g})$ and $5d(e_g)$ bands. The 1.2 eV splitting between these bands in EuSe is about $\sim$ 0.4 eV larger than in EuTe due to its stronger crystal field [87]. The inset of Fig. 3.11 illustrates that the observed THG intensity $I_{\parallel}^{3\omega}$ does not depend on the temperature, at least up to 50 K. The rotational diagram of $I_{\parallel}^{3\omega}$ is isotropic

and in accordance with Eq. (3.2). In contrast to EuTe residual signals are observed for $\mathbf{E}^{3\omega} \perp \mathbf{E}^{\omega}$ in EuSe, although no crystallographic signals are predicted in this configuration. Their overall strength is very weak $\frac{I_{\perp}^{3\omega}}{I_{\parallel}^{3\omega}} \approx 1\%$ and they show the same temperature and angle dependencies as signals measured in the parallel configuration pointing at possible leakage as an explanation for these residual THG signals. The observed THG signals without a magnetic field have shown pure crystallographic character and no contributions from the anti-ferromagnetic ordering of the spin lattices could be resolved.

3.6.2 Magnetic-Field-Induced Contributions to $\chi^{(3)}$

Figures 3.12 and 3.13 display the results of THG spectroscopy in static magnetic fields for the high $5d(e_g)$ and low $5d(t_{2g})$ bands in EuSe, respectively. The induced effects are studied in the configuration $\mathbf{E}^{3\omega} \perp \mathbf{E}^{\omega} \parallel \mathbf{B}$, where crystallographic signals are forbidden; see Eq. (3.3). The signals of both bands depend on the magnetic phase determined by the magnetic field; compare with Fig. 3.2.

On the one hand, the THG spectrum of the high-energy range does not change significantly, when the magnetic field is increased from $B = 0$ T to -0.12 T, and the magnetic phase is switched from AFM to FIM; compare orange and blue spectra in Fig. 3.12 (a). The intensity increases slightly, but the spectral shape is unchanged. On the other hand, a further increase in magnetic field strength to $B = -2$ T switches the magnetic phase to FM and new features show up; see green spectrum in Fig. 3.12 (a). These features stem from the complicated electronic structure of the excited states $f^6 5d^1(e_g)$, which are not discussed in detail here. The magnetic-field dependence of the integrated intensity of the spectral range $3.1 - 3.7$ eV is given in Fig. 3.12 (b). THG signals increase from AFM over FIM phases to FM phases. They reach a saturation level in the FM phase for $B > 1$ T. It is already known from a Faraday effect study (see Ref. [94]) that in EuSe the internal alignment of spins reaches 80% of its saturation value at magnetic fields of about 1 T, and it is only weakly increased in higher fields up to 7 T. A good approximation for this behavior gives the dependence $[a + bM(B)]^2$ with $a \approx 1.3b$ and $M(B)$ after Ref. [99]. The parameters a and b are almost equal demonstrating that in the perpendicular configuration $I_{\perp}^{3\omega}$ the magnetic-field-induced and residual crystallographic THG intensities are comparable strong.

On the other hand, in the low-energy region a feature appears around 2.35 eV already in the FIM phase; compare blue and orange spectra in Fig. 3.13.Its intensity increases further with growing field strength, reaching a saturation level in the FM phase for $B > 1$ T. The inset in Fig. 3.13 illustrates that the integrated magnetic-field-induced THG intensity is well approximated by the dependence $[a + bM(B)]^2$ with $a \approx 1.3b$ and $M(B)$ after Ref. [99], which gives a good description for the high-energy band $5d(e_g)$ as well. The microscopic origin of this feature remains unclear.

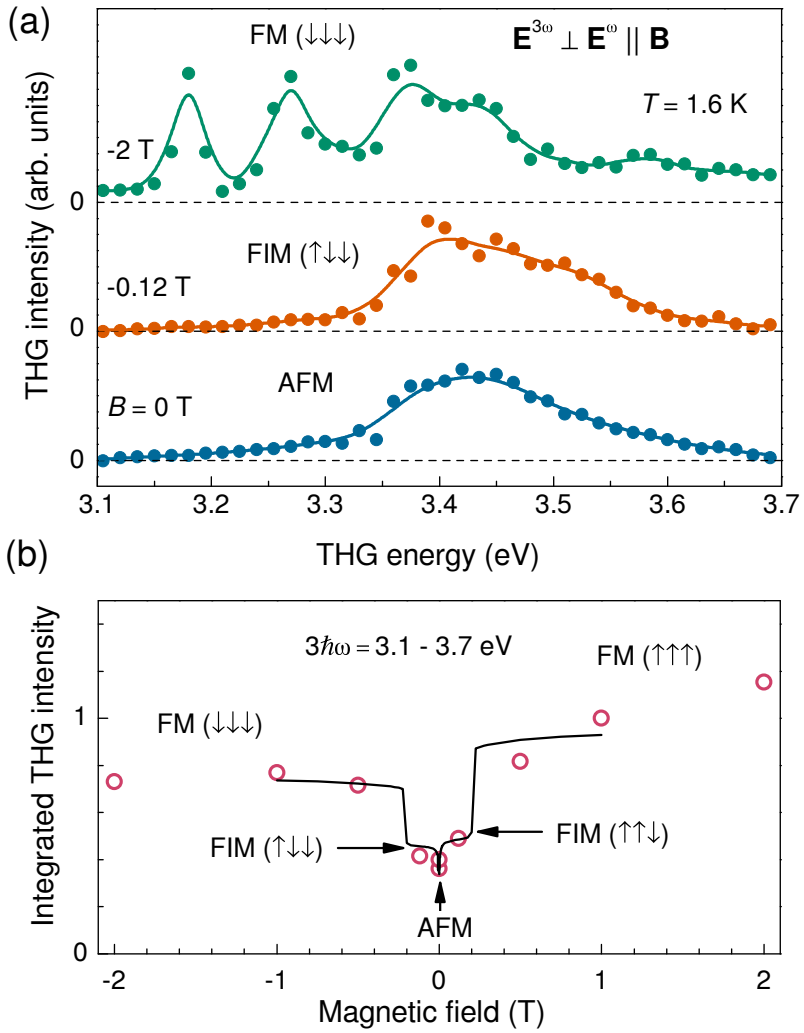

Figure 3.12: (a) THG spectra of EuSe in the energy range $3.1-3.7$ eV for $\mathbf{E}^{3\omega} \perp \mathbf{E}^{\omega} \parallel \mathbf{B}$ at $T = 1.6$ K. Green, orange, and blue spectra display THG signals measured at $B = -2$ T, -0.12 T, and 0 T. Solid lines are guides for the eye, and dashed lines indicate zero levels. (b) Magnetic-field dependence of the THG intensity integrated over the spectral range $3.1-3.7$ eV. The solid line shows the normalized function $[a+bM(B)]^2$ with $a = 1.3b$ and $M(B)$ after Ref. [99].

Magnetic-field-induced THG signals show polarization anisotropies as depicted in Fig. 3.14. Their shapes for the parallel $I_{\parallel}^{3\omega}$ [see Fig. 3.14 (a)] and crossed $I_{\perp}^{3\omega}$ [see Fig. 3.14 (a)] configurations are in accordance with Eqs. (3.2) and (3.6), and Eqs. (3.3) and (3.7), respectively. It is important to take into account the interference of crystallographic and magentic-field-induced signals according with Eqs. (1.19) and (3.8).

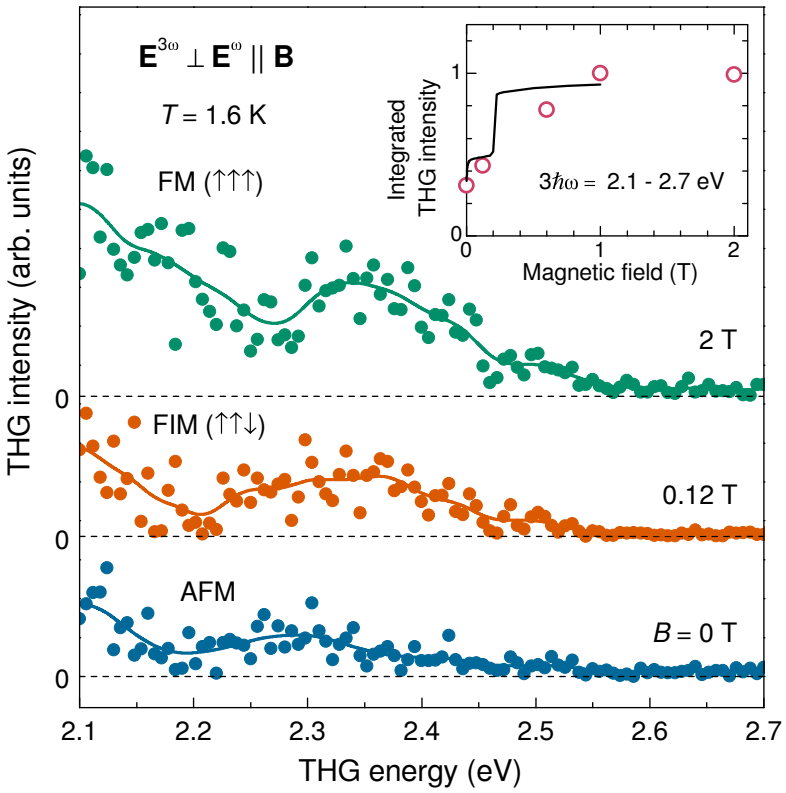

Figure 3.13: (a) THG spectra of EuSe in the energy range $2.1-2.7$ eV for $\mathbf{E}^{3\omega} \perp \mathbf{E}^{\omega} \parallel \mathbf{B}$ at $T = 1.6$ K. Green, orange, and blue spectra display THG signals measured at $B = 2$ T, 0.12 T, and 0 T, respectively. Solid lines are guides for the eye, and dashed lines indicate zero levels. Inset shows the magnetic-field dependence of the THG intensity integrated over the spectral range $2.1-2.7$ eV. The solid line shows the normalized function $[a+bM(B)]^2$ with $a = 1.3b$ and $M(B)$ after Ref. [99].

3.6.3 Discussion

Comparison of THG and SHG Spectra

A direct comparison of wide-range THG and SHG spectra presented in Fig. 3.15 confirms that both are governed by the same specific electronic properties of EuX. The given data is mostly measured for $\mathbf{E}^{3\omega,2\omega} \perp \mathbf{E}^{\omega} \parallel \mathbf{B}$ except the SHG signals for the higher band $3.2-3.6$ eV, which are only seen for $\mathbf{E}^{2\omega} \parallel \mathbf{E}^{\omega} \parallel \mathbf{B}$. SHG and THG spectroscopy deliver in principle the same spectral results, but THG signals are an order of magnitude stronger. Signals due to electric-dipole contributions to $\chi^{(3)}$ can be as strong and even stronger than signals due to magnetic-dipole contributions to $\chi^{(2)}$. Therefore, the THG spectroscopy seems to be the more suitable tool for studies of centrosymmetric materials.

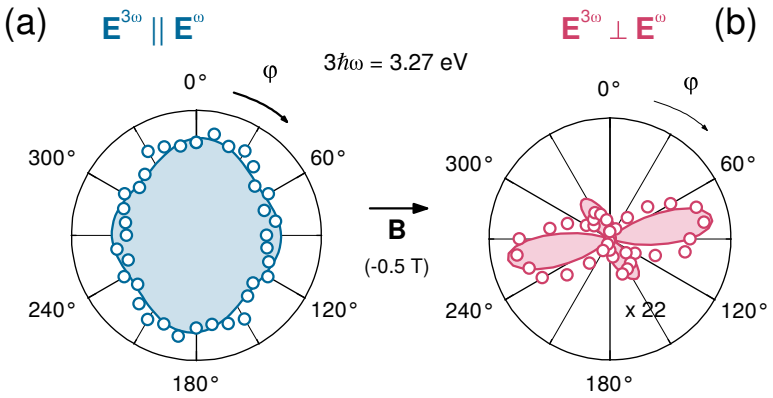

Figure 3.14: Rotational anisotropies of the third-harmonic-light polarization in EuTe measured for the strongest peak at $3\hbar\omega = 3.27$ eV for $B = -0.5$ T at $T = 1.6$ K. Circles in (a) and (b) display parallel $I_{\parallel}^{3\omega}$ and perpendicular $I_{\perp}^{3\omega}$ configurations, respectively. The areas give fittings following (a) Eqs. (3.2) and (3.6), and (b) Eqs. (3.3) and (3.7), while the interference of crystallographic and magentic-field-induced signals is considered according to Eqs. (1.19) or (3.8).

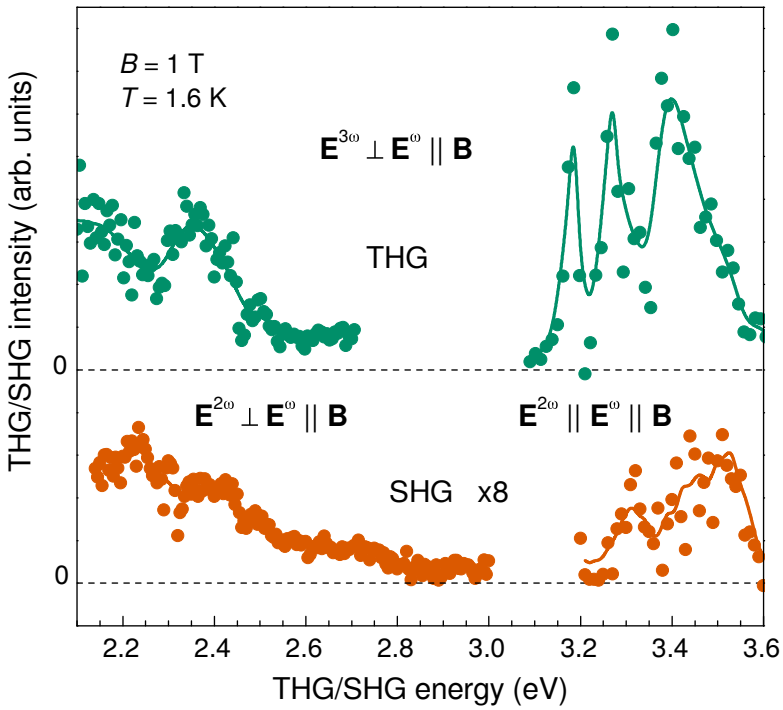

Figure 3.15: THG and SHG spectra of EuSe measured mostly for $\mathbf{E}^{3\omega} \perp \mathbf{E}^{\omega} \parallel \mathbf{B}$ and $B = 1$ T at $T = 5$ K. The high-energy range of the SHG spectra is measured for $\mathbf{E}^{3\omega} \parallel \mathbf{E}^{\omega} \parallel \mathbf{B}$. The SHG signals are enhanced by a factor of 8. Points resemble measurements and lines are guides for the eye.

4 Summary

For resonant SHG, the responsible state needs to fulfill the selection rules for one- and two-photon transitions simultaneously. The thorough analyses of the spectral, polarization, temperature, magnetic field, and electric field dependences of the observed SHG signals and the consequent theoretical discussion of excitations reveal four distinct mechanisms, which enable the emission of SHG resonant to the energy levels of Wannier excitons. All of them have in common that they enable the coherent three photon process by the field-induced mixing of one-photon and two-photon allowed exciton(-polariton) states. First, an electric field leads to the mixing of states with envelope wave functions of even and odd parity, e.g., S and P. This mechanism enables the three-photon process via three electric dipole transitions. Second, a comparable effect is observed, when the exciton exhibits an external magnetic field. The effective electric field due to the magneto-Stark effect leads to a mixing of states with odd and even parity, which results in the efficient SHG. Thirdly, exciton states with different spin wave functions, but with the same main quantum number n, can become mixed as a consequence of the spin Zeeman effect in magnetic fields. Thus, states that are spin forbidden for either one- or two-photon transitions can form new states that are active for the SHG. Forthly, the mixing of different orbital wave functions for states of the same main quantum number $n \geq 2$ by the orbital Zeeman effect in magnetic fields can lead to new states that allow the SHG. All mechanisms lead to significant SHG signals, although their microscopic explanations go beyond the electric dipole approximation. The unveiled microscopic mechanisms are specific to excitons. SHG signals were not induced by external fields neither off-resonant nor above the band gap at all.

This variety of mechanisms may help to understand the microscopic origin of previously reported optical harmonics generation in vicinity of exciton resonances, e.g., in GaAs and CdTe [12], or (Cd,Mn)Te [13]. The simultaneous application of electric and magnetic fields fortified the proposed mechanism based on the magneto-Stark effect. Therefore, this technique is suggested to clarify, if the magneto-Stark effect is the main mechanism for the magnetic-field-induced SHG of excitons in other semiconductors, e.g., GaAs, too.

The study of the THG in centrosymmetric EuX allows the separation of the crystallographic and the magnetic-field-induced THG signals. The main characteristics of the observed THG is explained by the specific electronic structure of these magnetic materials, i.e., their strongly localized ground states, which give rise to their

distinct magnetic properties, too. The theoretically predicted pure antiferromagnetic contributions to THG could not be observed. Nevertheless, the THG is able to resolve antiferro-, ferri-, and ferromagnetic phases. This can be used to surveil the magnetic structure for example during growth processes. The comparison of spectroscopic SHG and THG studies in EuX leads to the recommendation of the THG spectroscopy for the investigation of centrosymmetric materials.

5 Appendix

5.1 Modeling of Polarization Anisotropies

For simplicity the basis of the laboratory system is defined by:

$$\begin{pmatrix} 1 & 0 & 0 \\ 0 & 1 & 0 \\ 0 & 0 & 1 \end{pmatrix}$$

An Euler-matrix SampleTilt accounts for the arbitrary sample orientation, where $\mathbf{n}$ is the rotation axis and α the rotation angle for a rotation, that transforms the laboratory axes to the intrinsic crystal axes:

$$\text{SampleTilt}(\mathbf{n}, \alpha) = \tag{5.1}$$
$$\begin{pmatrix} \cos\alpha + n_1^2(1-\cos\alpha) & n_1 n_2(1-\cos\alpha) - n_3\sin\alpha & n_2\sin\alpha + n_1 n_3(1-\cos\alpha) \\ n_1 n_2(1-\cos\alpha) + n_3\sin\alpha & \cos\alpha + n_2^2(1-\cos\alpha) & -n_1\sin\alpha + n_2 n_3(1-\cos\alpha) \\ -n_2\sin\alpha + n_1 n_3(1-\cos\alpha) & n_1\sin\alpha + n_2 n_3(1-\cos\alpha) & \cos\alpha + n_3^2(1-\cos\alpha) \end{pmatrix}$$

The basis of the crystallographic system can therefore be written as the matrix product:

$$\text{CrystalBasis} = \text{SampleTilt}(\mathbf{n}, \alpha) \begin{pmatrix} 1 & 0 & 0 \\ 0 & 1 & 0 \\ 0 & 0 & 1 \end{pmatrix} \tag{5.2}$$

The complex tensor components of the crystallographic susceptibility χ are defined according to the symmetry group of the crystal under investigation, e.g., ZnO [21, 22]:

$$\begin{aligned} \chi_{1,1,3} = \chi_{2,2,3} = \chi_{1,3,1} = \chi_{2,3,2} &= \text{xxz} + \text{ixxz}' \\ \chi_{3,1,1} = \chi_{3,2,2} &= \text{zxx} + \text{izxx}' \\ \chi_{3,3,3} &= \text{zzz} + \text{izzz}' \\ \text{all other elements} &= 0 \end{aligned} \tag{5.3}$$

To calculate the rotational anisotropy of the emitted SHG light, φ is the turning angle of the incoming polarization around the direction of light propagation (here the z-axis):

$$\mathbf{E}^{\omega} = \begin{pmatrix} \cos\varphi & -\sin\varphi & 0 \\ \sin\varphi & \cos\varphi & 0 \\ 0 & 0 & 1 \end{pmatrix} \tag{5.4}$$

Now it is possible to transform the incoming light polarization into the basis of the crystal system, calculate the polarization of the outgoing light in the basis of the crystal system (for which the symmetry relations can be looked up, for example in [21, 22]), and then transform it back into the basis of the laboratory system:

$$\mathbf{E}^{\omega\prime} = \mathrm{CrystalBasis}^{\mathrm{T}}\mathbf{E}^{\omega} \tag{5.5}$$

$$\mathbf{E}^{2\omega\prime} = \begin{pmatrix} \sum_{i=1}^{3}\sum_{j=1}^{3}\chi_{1,i,j}E^{\omega\prime}{}_{i}E^{\omega\prime}{}_{j} \\ \sum_{i=1}^{3}\sum_{j=1}^{3}\chi_{2,i,j}E^{\omega\prime}{}_{i}E^{\omega\prime}{}_{j} \\ \sum_{i=1}^{3}\sum_{j=1}^{3}\chi_{3,i,j}E^{\omega\prime}{}_{i}E^{\omega\prime}{}_{j} \end{pmatrix} \tag{5.6}$$

$$\mathbf{E}^{2\omega} = \mathrm{CrystalBasis}\mathbf{E}^{2\omega\prime} \tag{5.7}$$

The measured configurations $I_{\parallel}^{2\omega}$ and $I_{\perp}^{2\omega}$ correspond to the respective projection of the outgoing light polarization:

$$I_{\parallel}^{2\omega} \propto= \mathbf{E}^{2\omega}\begin{pmatrix} \cos\varphi \\ \sin\varphi \\ 0 \end{pmatrix}, I_{\perp}^{2\omega} = \mathbf{E}^{2\omega}\begin{pmatrix} -\sin\varphi \\ \cos\varphi \\ 0 \end{pmatrix} \tag{5.8}$$

If, for example, the dependence on an external magnetic field $\mathbf{B}$ can be extracted from the susceptibility, Eq. (5.6) can be written as [1] :

$$\mathbf{E}^{2\omega\prime} = \begin{pmatrix} \sum_{i=1}^{3}\sum_{j=1}^{3}\sum_{k=1}^{3}\sum_{l=1}^{3}\chi_{1,i,j,k,l}E^{\omega\prime}{}_{i}E^{\omega\prime}{}_{j}B'_{kl} \\ \sum_{i=1}^{3}\sum_{j=1}^{3}\sum_{k=1}^{3}\sum_{l=1}^{3}\chi_{2,i,j,k,l}E^{\omega\prime}{}_{i}E^{\omega\prime}{}_{j}B'_{kl} \\ \sum_{i=1}^{3}\sum_{j=1}^{3}\sum_{k=1}^{3}\sum_{l=1}^{3}\chi_{3,i,j,k,l}E^{\omega\prime}{}_{i}E^{\omega\prime}{}_{j}B'_{kl} \end{pmatrix}, \tag{5.9}$$

[1] Please note that the magnetic field is represented by a third rank tensor rather than a pseudo vector:

$$\mathbf{B} = \begin{pmatrix} 0 & -B_z & B_y \\ B_z & 0 & -B_x \\ -B_y & B_x & 0 \end{pmatrix}$$

B_{kl} directly reflects the transformation properties of the magnetic field and there is no need to distinguish between vectors and pseudo vector nor c and i tensors [104].

where $\chi_{o,i,j,k,l}$ reflects the reduced symmetry of the crystal, when the external perturbation is present.

The obtained function of such a model calculation can be used to fit the introduced parameters (n, α) describing the sample orientation with respect to the direction of light propagation z, and the tensor components of χ. The fitting results can be used to draw qualitative conclusions to discuss the nature of the involved processes and states.

5.2 Polariton Parameters in ZnO

	Fiebig (eV)	Wrzensinski (ev)
$T_{1S(A)}$	3.3759	3.37599
$L_{1S(A)}$	3.3778	3.37741
$T_{1S(B)}$	3.3816	3.38256
$L_{1S(B)}$	3.3929	3.39253
$T_{2S(A)}$	3.4227	
$L_{2S(A)}$	3.4232	
$T_{2S(B)}$	3.4276	
$L_{2S(B)}$	3.4304	
T_{b1}	4.4396	3.527
L_{b1}	4.4405	3.647
T_{b2}	4.5	
L_{b2}	5.9274	
$\epsilon_{\perp,\mathrm{b}}$	2.0484	3.658
$T_{1S(C)}$	3.4209	3.42162
$L_{1S(C)}$	3.4327	3.43264
$T_{2S(C)}$	3.4664	
$L_{2S(C)}$	3.4678	
T_{b1}	4.4723	3.561
L_{b1}	4.4790	3.683
T_{b2}	4.5	
L_{b2}	5.8658	
$\epsilon_{\parallel,\mathrm{b}}$	2.1171	3.754

Table 5.1: Polariton parameters for the $1S$ excitons in ZnO according to Fiebig [52] and Wrzesinski [50] (energies are given in eV and at $k = 0$).

5.3 Theoretical Model of THG in EuTe

The quantum mechanical model of the THG in EuTe provided by A. B. Henriques is based on certain assumptions made on the electronic structure of EuTe, which led to a successful description of the dichroic band-edge optical absorption (see Refs. [100, 102, 105]) as well as the SHG in EuTe [106]. This section gives a brief summary of his model; for a more detailed description see Ref. [85].

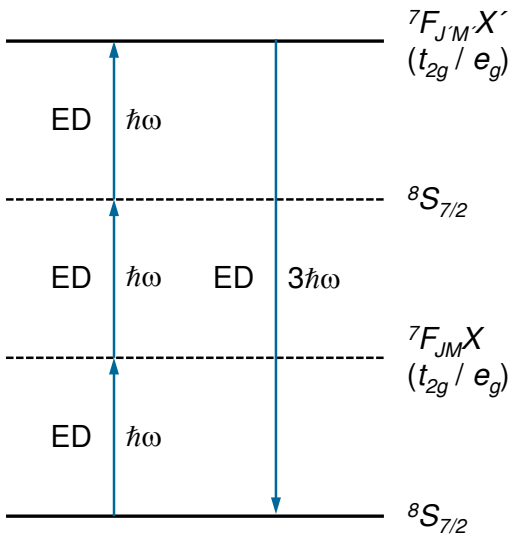

Figure 5.1: A Scheme of the four-photon process, which is used for the theoretical model of the THG in EuTe described in Ref. [85].

The model considers the four-photon process illustrated in Fig. 5.1. It is assumed that the three-photon transition is resonant with the energy of the $^8S_{7/2} \longleftrightarrow ^7 F_{J'M'}X'$ energy gap (this energy is approximately the band gap of EuTe). The solid line at the bottom represents the ground state, $^8S_{7/2}$ of the seven f-electrons localized at an Eu^{2+} lattice site; see Fig. 3.1 (b). The solid line at the top represents an excited state $^7F_{J'M'}X'$, which is formed by six localized electrons at an Eu^{3+} site and one electron in the $5d(t_{2g})$ or $5d(e_g)$ conduction bands; see Fig. 3.1 (b). The dashed lines illustrate the two intermediate states. They are virtual excitations to which one-photon transitions are electric-dipole (ED) allowed. It must be emphasized that in order to keep the model tractable, the following simplifications were made: (1) Only the $^8S_{7/2}$ and $^7F_{JM}X$ electronic levels were assumed to be optically active; (2) The tight-binding approximation with a common broadening parameter for all levels was used. Although these approximations can be quite acceptable to describe the t_{2g} conduction band, they can only provide a very crude description of the more energetic e_g states. The contribution of the considered four-photon process to the

third order polarization $\mathbf{P}^{3\omega}$ is approximated by

$$P^{3\omega} \propto \sum_{\substack{JMX,\\ J'M'X'}} E_J^2 E_{J'} \frac{\left|\langle {}^8S_{7/2}| \sum_{i=1}^7 x_i \, |{}^8F_{JM}X\rangle\right|^2 \left|\langle {}^8S_{7/2}| \sum_{i=1}^7 x_i \, |{}^8F_{J'M'}X'\rangle\right|^2}{(E_{J'X'} - \hbar\omega)(0 - 2\hbar\omega)(E_{JX} - 3\hbar\omega)}. \quad (5.10)$$

Here, x_i denotes the i-th electron position vector projected onto the polarization vector of the exciting light.

The model uses a limited set of electronic states that includes the $4f^7\left({}^8S_{7/2}\right)$ ground state, and the excited states contained in the $4f^6 5d^1$ configuration, i.e., one electron is excited from the $4f^7$ states to a state of the $5d$ subbands; see Figure 10 Ref. [85]. Thus, an excited state consists of six electrons in the $4f$ shell at an Eu^{3+} site (denoted as ${}^7F_{JM}$) and an electron in a Bloch state X. It is assumed that X and X' belong to the same crystal field split conduction band, i.e., either $5d(t_{2g})$ or $5d(e_g)$. In the tight-binding scheme X is given by

$$X(\mathbf{k}, \mathbf{r}) = \frac{1}{\sqrt{\mathcal{N}}} \sum_{\mathbf{R}} e^{i\mathbf{R}\cdot\mathbf{k}} \phi(\mathbf{r} - \mathbf{R}), \quad (5.11)$$

where $\phi(\mathbf{r})$ represents one of the three $5d(t_{2g})$ europium orbitals (d_{xy}, d_{yz} or d_{zx}), or one of the two $5d(e_g)$ europium orbitals (d_{z^2} or $d_{x^2-y^2}$). $\mathbf{R}$ is the position vector of an Eu atom in the lattice, and $\mathcal{N}$ is the number of lattice sites inside the Born-von Karmán volume.

The Zeeman energies of the Eu^{2+} ions are disregarded, because they are negligible compared to the energy shift associated with the $d - f$ exchange interaction. Consequently, the ${}^7F_{JM}$ levels have a $2M + 1$-fold degeneracy, and the energy of an electronic excitation, E_{JX}, depends only on the quantum numbers J and X:

$$E_{JX} = E_G + \Delta_X + \frac{1}{2}\lambda_{4f} J(J+1) + \epsilon_X(\mathbf{k}), \quad J = 0, \ldots, 6, \quad (5.12)$$

where $\lambda_{4f} = 9.6$ meV is the spin-orbit interaction constant for electrons in the $4f$ orbital of the Eu^{2+} ion, [102] and $\epsilon_X(\mathbf{k})$ is the energy dispersion of the $5d(t_{2g})$ or $5d(e_g)$ conduction band; Δ_X is given by

$$\Delta_X = \begin{cases} 0 & \text{if } X \text{ belongs to a } 5d(t_{2g}) \text{ band} \\ \Delta_{\mathrm{CF}} & \text{if } X \text{ belongs to a } 5d(e_g) \text{ band.} \end{cases} \quad (5.13)$$

E_G is the magnetic-field-dependent energy band gap of the EuX system, which for EuTe is given by [100]:

$$E_G = E_G(0) - J_{df} S \times \begin{cases} \left(\frac{B}{B_{\mathrm{sat}}}\right)^2 & \text{if } B < B_{\mathrm{sat}} \\ 1 & \text{if } B \geq B_{\mathrm{sat}}, \end{cases} \quad (5.14)$$

where $E_G(0) = 2.321$ eV is the zero-field band gap, and $J_{df}S$ is the d-f exchange constant, taken to be$J_{df}S$=130 meV [106].

We shall use two characteristics of the above described electronic energy level scheme:

(i) the energy spread of the excited states is much smaller than the band gap, i.e., $E_G \gg \lambda_{4f}$, and E_G is much larger than the energy width of $\epsilon_X(\mathbf{k})$;

(ii) all excited states have the same parity, which is opposite to the parity of the ground state.

From the first property, it can be concluded that the dominant third-order induced polarization will be strongly resonant when the photon energy is about $\hbar\omega \sim \frac{1}{3}(E_G + \Delta_X)$. Therefore, we may discard the anti-resonant contributions [1, 2] to the induced third-order dipole moment. From the second property, electric-dipole matrix elements between excited states vanish.

The matrix elements given in Eq. (5.10) involve seven electrons, but they can be rewritten to computable one electron matrix elements by a Clebsch-Gordon expansion of the ${}^7F_{JM}$ states. To obtain the THG spectrum, the conduction band dispersion is ignored, and the one electron matrix elements are calculated using transition between the orbital functions of $5d(t_{2g})$ or $5d(e_g)$ and the $4f$ orbitls; for details see Ref. [106]. The width of the conduction band energy is taken into account by convolving the third order polarization with a sum of Gaussian functions centered at the energies E_{JX} (Eq. (5.12)). For simplicity, their the full widths are assumed as constant.

Further, it is necessary to make assumptions on the spatial orientation of the Eu^{2+} spins [107]. Naturally at $B = 0$, the Eu^{2+} spins lie in the (111) planes. It is known that epitaxial layers of EuTe grown by MBE contain only one single T-domain, i.e., all spins align in one type of the four equivalent (111) planes [108].

Values and dependences of the THG intensity in a magnetic field are determined by the transitions between $4f$ and $5d$ orbitals. These matrix elements dependent strongly on the spatial orientation of these orbitals, which is determined by the modulus of the magnetic field, as well as its direction with respect to the crystallographic axes. However, the model does not change the calculated THG intensity, when the the magnetic field direction is inverted.

The characteristic values used for the parameters to calculate the THG spectra for EuTe can be found in Ref. [106].

Comparison Between Modeled SHG and THG

An external magnetic field has a fundamental effect on the SHG and THG efficiencies in EuX, because its strength and direction determines the orientation of the

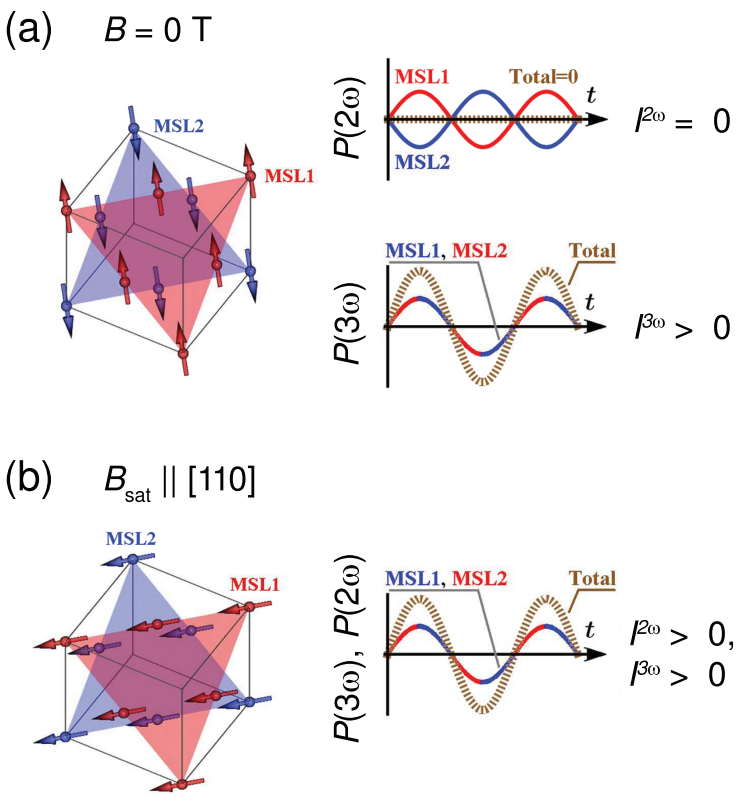

Figure 5.2: An illustration of the modeled SHG and THG polarizations in EuTe at (a) $\mathbf{B} = 0$ and $\mathbf{B} = \mathbf{B}_{\text{saturation}}$.

Eu^{2+} spins [107]. Fig. 5.2 illustrates the role of the spin orientation in the generation of second and third harmonics. On the one hand at $\mathbf{B} = 0$, the spin sublattices are oriented antiparallel. SHG orginates from the magnetic dipole coupling between excited states, [14, 15, 106] and the polarization waves arising from both magnetic sublattices pointing in opposite directions. Thus, their interference leads to a zero net polarization, and no SHG occurs without an external field. In contrast, the third-order polarizations originating from electric-dipole coupling between $4f$ and $5d$ orbitals are in phase with one another, regardless of the orientation of the sublattices. Thus, their amplitudes add up and crystallographic THG is allowed. On the other hand at $\mathbf{B} = \mathbf{B}_{\text{saturation}}$ (the field in which all spins are alligned parallel to the external magnetic field direction), the ferromagnetic alignment, where only one single magnetic sublattice remains, leads to SHG as well as to THG.

List of Publications

- **M. Lafrentz**, D. Brunne, A. V. Rodina, V. V. Pavlov, R. V. Pisarev, D. R. Yakovlev, A. Bakin, and M. Bayer, *Second harmonic generation spectroscopy of excitons in ZnO*, submitted to Phys. Rev. B.
- **M. Lafrentz**, D. Brunne, B. Kaminski, V. V. Pavlov, A. V. Rodina, R. V. Pisarev, D. R. Yakovlev, A. Bakin, and M. Bayer, *Magneto-Stark Effect of Excitons as the Origin of Second Harmonic Generation in ZnO*, Phys. Rev. Lett. **110**, 116402 (2013).
- **M. Lafrentz**, D. Brunne, B. Kaminski, V. V. Pavlov,, R. V. Pisarev, A. B. Henriques D. R. Yakovlev, G. Springholz, G. Bauer, E. Abramof, P. H. O. Rappl, and M. Bayer, *Optical third harmonic generation in the magnetic semiconductor EuSe*, Phys. Rev. B **85**, 03520 (2012).
- **M. Lafrentz**, D. Brunne, B. Kaminski, V. V. Pavlov, A. B. Henriques, R. V. Pisarev, D. R. Yakovlev, G. Springholz, G. Bauer, and M. Bayer, *Optical third-harmonic spectroscopy of the magnetic semiconductor EuTe*, Phys. Rev. B **82**, 235206 (2010).
- B. Kaminski, **M. Lafrentz**, R. V. Pisarev, D. R. Yakovlev, V. V. Pavlov, V. A. Lukoshkin, A. B. Henriques, G. Springholz, G. Bauer, E. Abramof, P. H. O. Rappl, and M. Bayer, *Optical Second Harmonic Generation in the Centrosymmetric Magnetic Semiconductors EuTe and EuSe*, Phys. Rev. B **81**, 155201 (2010).
- R. V. Pisarev, B. Kaminski, **M. Lafrentz**, V.V. Pavlov, D. R. Yakovlev, and M. Bayer, *Novel mechanisms of optical harmonics generation in semiconductors*, Phys. Stat. Sol. B **247**, 1498 (2010).
- B. Kaminski, **M. Lafrentz**, R. V. Pisarev, D. R. Yakovlev, V. V. Pavlov, V. A. Lukoshkin, A. B. Henriques, G. Springholz, G. Bauer, E. Abramof, P. H. O. Rappl, and M. Bayer, *Spin-Induced Optical Second Harmonic Generation in the Centrosymmetric Magnetic Semiconductors EuTe and EuSe*, Phys. Rev. Lett. **103**, 057203 (2009).

Bibliography

[1] R. W. Boyd, *Nonlinear Optics*, Third Edition, (Academic/Elsevier, Burlington, 2008).

[2] Y. R. Shen, *The Principles of Nonlinear Optics* (Wiley, New York, 2003).

[3] R. L. Sutherland, *Handbook of Nonlinear Optics*, Second Edition (Marcel Dekker Inc., New York, 2003)

[4] *Nonlinear Optics in Semiconductors I and II*, edited by E. Garmire and A. Kost (Academic, New York, 1999).

[5] E. Garmire, *Resource Letter NO-1: Nonlinear Optics*, Am. J. Phys. **79**(3), 245 (2011).

[6] P. A. Franken, A. E. Hill, C. W. Peters, and G. Weinreich, *Generation of Optical Harmonics*, Phys. Rev. Lett. **7** 118 (1961).

[7] *Non-Linear Optical Properties of Matter - From Molecules to Condensed Phases*, edited by M. G. Papadopoulos, A. J. Sadlej, and J. Leszczynski (Springer, Dordrecht, 2006).

[8] K. R. Parameswaran, J. R. Kurz, M. M. Roussev, and Fejer, *Observation of 99% pump depletion in single-pass second-harmonic generation in a periodically poled lithium niobate waveguide*, Optics Letters **27**, 43 (2002).

[9] D. J. Brown, N. Morishige, A. Neekhra, Don S. Minckler, J. V. Jester, *Application of second harmonic imaging microscopy to assess structural changes in optic nerve head structure ex vivo*, Journal of Biomedical Optics **12** (2), 024029 (2007).

[10] M. Fiebig, V. V. Pavlov, and R. V. Pisarev, *Second-Harmonic Generation as a Tool for Studying Electronic and Magnetic Structures of Crystals: Review*, J. Opt. Soc. Amer. **22**, 96 (2005).

[11] R. V. Pisarev, B. Kaminski, M. Lafrentz, V.V. Pavlov, D. R. Yakovlev, and M. Bayer, *Novel mechanisms of optical harmonics generation in semiconductors*, Phys. Stat. Sol. B **247**, 1498 (2010).

[12] I. Sänger, B. Kaminski, D. R. Yakovlev, R. V. Pisarev, M. Bayer, G. Karczewski, T. Wojtowicz, and J. Kossut, *Orbital Quantization of Electronic States in a Magnetic Field as the Origin of Second-Harmonic*, Phys. Rev. B **74**, 165208 (2006).

[13] I. Sänger, D. R. Yakovlev, R. V. Pisarev, V. V. Pavlov, M. Bayer, G. Karczewski, T. Wojtowicz, and J. Kossut, *Spin and Orbital Quantization of Electronic States as Origins of Second Harmonic Generation in Semiconductors*, Phys. Rev. Lett. **96**, 117211 (2006).

[14] B. Kaminski, M. Lafrentz, R. V. Pisarev, D. R. Yakovlev, V. V. Pavlov, V. A. Lukoshkin, A. B. Henriques, G. Springholz, G. Bauer, E. Abramof, P. H. O. Rappl, and M. Bayer, *Spin-Induced Optical Second Harmonic Generation in the Centrosymmetric Magnetic Semiconductors EuTe and EuSe*, Phys. Rev. Lett. **103**, 057203 (2009).

[15] B. Kaminski, M. Lafrentz, R. V. Pisarev, D. R. Yakovlev, V. V. Pavlov, V. A. Lukoshkin, A. B. Henriques, G. Springholz, G. Bauer, E. Abramof, P. H. O. Rappl, and M. Bayer, *Optical Second Harmonic Generation in the Centrosymmetric Magnetic Semiconductors EuTe and EuSe*, Phys. Rev. B **81**, 155201 (2010).

[16] J. D. Jackson, *Classical Electrodynamics* (John Wiley & Sons Ltd., New York, 1962)

[17] J. A. Armstrong, N. Bloembergen, J. Ducuing, and P.S. Pershan, *Interactions between Light Waves in a Nonlinear Dielectric*, Phys. Rev. **127** 1918 (1962).

[18] P. S. Pershan, *Nonlinear Optical Properties of Solids: Energy considerations*, Phys. Rev. **130** 919 (1963)

[19] L. D. Landau and E. M. Lifshitz, *Electrodynamics of Contiuous Media* (Pergamon Press, Oxford, 1960).

[20] P. Guyot-Sionnest and Y. R. Shen, *Bulk Contribution in Surface Second-Harmonic Generation*, Phys. Rev. B **38**, 7985 (1988).

[21] S. V. Popov, Y. P. Svirko, and N. I. Zheludev, *Susceptibility Tensors for Nonlinear Optics* (Institute of Physics Publishers, Philadelphia, 1995).

[22] R. R. Birss, *Symmetry and Magnetism* (North-Holland, Amsterdam, 1967).

[23] C. Cohen-Tannoudji, B. Diu, and F. Laloë, *Quantum Mechanics*, Volume I and II (Wiley, Lodon, 1977).

[24] D. Park, *Introduction to the Quantum Theory* (McGraw-Hill Companies, New York and others, 1974)

[25] F. Schwabel, *Quantenmechanik I*, 6th edition (Springer, Berlin, 2005)

[26] V. V. Pavlov, A. V. Kalashnikova, R. V. Pisarev, I. Sänger, D. R. Yakovlev, and M. Bayer, *Magnetic-Field-Induced Second-Harmonic Generation in Semiconductor GaAs*, Phys. Rev. Lett. **94**, 157404 (2005).

[27] M. Lafrentz, D. Brunne, B. Kaminski, V. V. Pavlov, A. V. Rodina, R. V. Pisarev, D. R. Yakovlev, A. Bakin, and M. Bayer, *Magneto-Stark Effect of Excitons as the Origin of Second Harmonic Generation in ZnO*, Phys. Rev. Lett. **110**, 116402 (2013).

[28] C. Klingshirn, *Semiconductor Optics*, 2nd edition (Springer-Verlag, Berlin, 2001).

[29] B. Hönerlage, R. Lévy, J. B. Grun, C. Klingshirn, and K. Bohnert, *The Dispersion of Excitons, Polaritons and Biexcitons in Semiconductors*, Phys. Rep. **124**, 161 (1985).

[30] R. S. Knox, *Theory of Excitons*, Solid State Physics Supplement **5**, edited by H. Ehrenreich, F. Seitz, and D. Tunbull (Academic Press, New York and London, 1963)

[31] R. G. Wheeler and J. O. Dimmock, *Exciton Structure and Zeeman Effects in CdSe*, Phys. Rev. **125**, 1805 (1962).

[32] C. Schweitzer, *Nicht lineare Spektroskopie an Halbleitern mit großer Bandlücke* Dissertation (Dortmund, Germany, 2002).

[33] D. G. Thomas and J. J. Hopfield, *Direct Observation of Exciton Motion in CdS*, Phys. Rev. Lett. *5*, 505 (1960).

[34] D. G. Thomas and J. J. Hopfield, *A Magneto-Stark Effect and Exciton Motion in CdS*, Phys. Rev. **124**, 657 (1961).

[35] *Spitlight 600 manua*l, Innolas (2007).

[36] *premiScan brochure*, GWU (2007)

[37] *Crystal catalog 2010-2011*, Castech (2010)

[38] *Advances in Atomic Spectroscopy Volume 5*, edited by J. Sneddon (1999)

[39] Specifications brochure *Gratings for HR460*, Jobyn Ivon (2013)

[40] *Pixis256 datasheet*, Pixis (2010)

[41] Ü. Özgür, Ya. I. Alivov, C. Liu, A. Teke, M. A. Reshchikov, S. Doğan, V. Avrutin, S.-J. Cho, and H. Morkoç, *A Comprehensive Review of ZnO Materials and Devices*, J. Appl. Phys. **98**, 041301 (2005).

[42] D. C. Haueisen and H. Mahr, *Nonlinear Electronic Dispersion in CuCl*, Phys. Rev. Lett. **26**, 838 (1971).

[43] D. C. Haueisen and H. Mahr, *Resonant Second-Harmonic Generation in the Exciton Region of CuCl and ZnO*, Phys. Rev. B **8**, 734 (1973).

[44] C. Klingshirn, *ZnO: From Basics Towards Applications*, Phys. Stat. Sol. (b) **244**, 3027 (2007).

[45] C. Klingshirn, *ZnO: Material, Physics and Applications*, Chem. Phys. Chem. **8**,782 (2007).

[46] *Zinc Oxide Bulk, Thin Films and Nanostructures*, edited by C. Jagadish and S. Pearton (Elsevier Science, 2006).

[47] Landolt-Börnstein, *Numerical Data and Functional Relationship in Science and Technology*, New Series III Vols. **17B**, **22**, and **41B**, edited by U. Rösler et al. (Springer, Berlin, 1999).

[48] J. J. Hopfield and D. G. Thomas, *Photon Momentum Effects in the Magneto-Optics of Excitons*, Phys. Rev. Lett. **4**, 357(1960).

[49] W. R. L. Lambrecht, A. V. Rodina, S. Limpijumnong, B. Segall, and B. K. Meyer, *Valence-Band Ordering and Magneto-Optic Exciton Fine Structure in ZnO*, Phys. Rev. B **65**, 075207 (2002).

[50] J. Wrzesinski, D. Fröhlich, *Two-Photon and Three-Photon Spectroscopy of ZnO Under Uniaxial Stress*, Phys. Rev. B **56**, 13087 (1997).

[51] E. L. Ivchenko, in *Excitons*, edited by E. I. Rashba and M.D. Sturge (North-Holland, Amsterdam, 1982).

[52] M. Fiebig, D. Fröhlich, and Ch. Pahlke-Lerch, *Multiphoton Polariton Spectroscopy on ZnO*, Phys. Stat. Sol. (b) **177**, 187 (1993).

[53] W. L. Bond, *Measurement of the Refractive Indices of Several Crystals*, J. Appl. Phys. **36**, 1674 (1965).

[54] H. Yoshikawa and S. Adachi, *Optical Constants of ZnO*, Jpn. J. Appl. Phys. **36**, 6237 (1997).

[55] Th. Hahn, *International Tables for Crystallography Volume A: Space-Group Symmetry*, 5th edition (Springer-Verlag, Berlin, 2002)

[56] Ch. Pahlke-Lerch, *Experimentelle Untersuchungen zu den Maxwellschen Randbedingungen in der nichtlinearen Spektroskopie* Dissertation (Dortmund, Germany, 1993).

[57] B. Kaminski, *New Mechanisms of Optical Harmonic Generation in Semicondutors* Dissertation (Dortmund, Germany, 2009)

[58] M. Fiebig, *Multiphoton Polariton Spectroscopy on Zink Oxide* Dissertation (Dortmund, Germany, 1992).

[59] G. Blattner, G. Kurtze, G. Schmieder, and C. Klingshirn, *Influence of magnetic fields up to 20 T on excitons and polaritons in CdS and ZnO*, Phys. Rev. B. **25** 7413 (1982).

[60] G. F. Koster, J. O. Dimmock, R. G. Wheeler, and H. Statz, *Properties of the thirty-two point groups* (MIT Press Cambridge, Massachusetts, 1963).

[61] R. Dinges, D. Fröhlich, B. Staginnus, and W. Staude, *Two-photon Magnetoabsorbtion in ZnO*, Phys. Rev. Lett. **25**, 922 (1970).

[62] W. Kaule, *Zum Zweiquantenabsorbtionsspektrum freier Exzitonen* Dissertation Coburg, Germany, 1971).

[63] M. Cobet, Ch. Cobet, M. R. Wagner, N. Esser, Ch. Thomsen, and A. Hoffmann, *Polariton Effects in the Dielectric Function of ZnO Excitons Obtained by Ellipsometry*, Appl. Phys. Lett. **96**, 031904 (2010).

[64] V. V. Pavlov, A. M. Kalashnikova, R. V. Pisarev, I, Sänger, D. R. Yakovlev, and M. Bayer, *Second-Harmonic Generation in the Magnetic Semiconductor (Cd,Mn)Te*, J. Opt. Soc. Amer. B **22**, 168 (2005).

[65] J. E. Sipe, D. J. Moss, and H. M. Van Driel, *Phenomenological theory of optical 2-nd and 3-rd harmonic generation from cubic centrosymmetric crystals*, Phys. Rev. B **35**, 1129 (1987).

[66] J. L. P. Hughes and J. E. Sipe, *Calculation of second-order optical response in semiconductors*, Phys. Rev. B 53, 10751 (1996).

[67] J. E. Sipe and E. Ghahramani, *Nonlinear-optical response of semiconductors in the independent-particle approximation*, Phys. Rev. B 48, 11705 (1993).

[68] J. E. Sipe and A. I. Shkrebtii, *Second-order optical response in semiconductors*, Phys. Rev. B **61**, 5337 (2000).

[69] D. J. Moss, E. Ghahramani, and J. E. Sipe, et al., *Band-structure calculation of chi(3) for 3rd-harmonc generation in Si, Ge, and GaAs*, Phys. Rev. B *41*, 1542 (1990).

[70] D. J. Moss, J. E. Sipe, and H. M. van Driel, *Empirical tight-binding calculations of dispersion in the 2-nd order nonlinear optical constants for zincblend crystals*, Phys. Rev B **36**, 9708 (1987).

[71] C. Aversa and J. E. Sipe, *Nonlinear optical susceptibilities of semiconductors - results with a length-gauge analysis*, Phys. Rev. B **52**, 14636 (1995).

[72] S. N. Rashkeev, W. R. L. Lambrecht, and B. Segall, *Efficient ab initio method for the calculation of frequency-dependent second-order optical response in semiconductors,* Phys. Rev. B **57**, 3905 (1998).

[73] S. N. Rashkeev, W. R. L. Lambrecht, *Second-harmonic generation of I-III-VI2 chalcopyrite semiconductors: Effects of chemical substitutions*, Phys. Rev. B **63**, 165212 (2001).

[74] S. N. Rashkeev, S. Limpijumnong, and W. R. L. Lambrecht, Phys. Rev. B **59**, 2737 (1999)

[75] S. N. Rashkeev, W.R.L. Lambrecht, and B. Segall, *Second-harmonic generation in SiC polytypes*, Phys. Rev. B **57**, 9705 (1998).

[76] A.-M. Janner, H. T. Jonkman, and G. A. Sawatzky, *Second-Harmonic Generation Spectroscopy: A Technique for Selectively Probing Excitons*, Phys. Rev. B **63**, 085111 (2001).

[77] A.-M. Janner, R. Eder, B. Koopmans, H. T. Jonkman, and G. A. Sawatzky, *Second-Harmonic Generation in C_{70} Film*, Phys. Rev. B **52**, 17158 (1995).

[78] A. Rodina, *private communications* (2012-2013).

[79] R. J. Elliot, *Intensity of Optical Absorption by Excitons*, Phys. Rev. **108**, 1384 (1957).

[80] R. D. R. Bhat, P. Nemec, Y. Kerachian, H. M. van Driel, J. E. Sipe, and A. L. Smirl, *Two-Photon Spin Injection in Semiconductors*, Phys. Rev. B **71**, 035209 (2005).

[81] L. E. Golub and E. L. Ivchenko, *Shift Photocurrent Induced by Two Quantum Transitions*, JETP **112**, 152 (2011).

[82] M. Abe, N. Awata, T. Matsushita, M. Hakamata, K. Ozawa, R. Murakami, I. Shoji, and T. Kondo, *Accurate Measurement of Quadratic Nonlinear-Optical Coefficients of Zinc Oxide*, J. Opt. Soc. Am. B **29**, 2392 (2012).

[83] G. Wang, G. K. L. Wong, and J. B. Ketterson, *Redetermination of Second-Order Susceptibility of Zinc Oxide Single Crystals*, Appl. Opt. **40**, 5436 (2001).

[84] T. S. Santos, J. S. Moodera, K. V. Raman, E. Negusse, J. Holroyd, J. Dvorak, M. Liberati, Y. U. Idzerda, and E. Arenholz, Phys. Rev. Lett. **101**, 147201 (2008).

[85] M. Lafrentz, D. Brunne, B. Kaminski, V. V. Pavlov, A. B. Henriques, R. V. Pisarev, D. R. Yakovlev, G. Springholz, G. Bauer, and M. Bayer, *Optical third-harmonic spectroscopy of the magnetic semiconductor EuTe*, Phys. Rev. B **82**, 235206 (2010).

[86] M. Lafrentz, D. Brunne, B. Kaminski, V. V. Pavlov,, R. V. Pisarev, A. B. Henriques D. R. Yakovlev, G. Springholz, G. Bauer, E. Abramof, P. H. O. Rappl, and M. Bayer, *Optical third harmonic generation in the magnetic semiconductor EuSe*, Phys. Rev. B **85**, 03520 (2012).

[87] A. Mauger and C. Godart, *The magnetic, optical, and transport properties of representatives of a class of magnetic semiconductors: The europium chalcogenides*, Phys. Rep. **141**, 51 (1986).

[88] G. Güntherodt, *Optical properties and electronic structure of europium chalcogenides*, Phys. Cond. Matter **18**, 37 (1974).

[89] T. Kasuya, *s-f Exchange Interactions and Magnetic Semiconductors*, Crit. Rev. Solid State Mater. Sci. **3**, 131 (1972).

[90] P. Wachter, *Handbook on the Physics and Chemistry of Rare Earths*, Vol. 11, Eds. K. A. Gschneider and L. R. Eyring (North Holland, Amsterdam, 1979), p. 507.

[91] J. Ferré, *Propriétés magnéto-optiques de matériaux para-, ferro-et antiferromagnétiques contenant l'ion europium divalent*, J. Phys. France **35**, 781 (1974).

[92] J. Schoenes and P. Wachter, *Magnetooptic Spectroscopy of EuS, EuSe, and EuTe*, IEEE Trans. Magnetics MAG **12**, 81 (1976).

[93] G. Busch, J. Schoenes, and P. Wachter, *Effect of magnetic ordering on the photoluminescence of EuS and EuTe*, Solid State Commun. **8**, 1841 (1970).

[94] J. Schoenes and P. Wachter, *High field magneto-optical study of EuSe and EuTe* , Physica B **89**, 155 (1977).

[95] M. Suekane, G. Kido, N. Miura, and S. Chikazumi, *Faraday rotation and magnetization observed for EuS and EuSe in megagauss fields*, J. Magn. Magn. Mater. **31-34**, 589 (1983).

[96] H. Hori, R. Akimoto, M. Kobayashi, S. Miyamoto, M. Furusawa, N. Kreines, A. Yamagishi, and M. Date, *High field Faraday rotation in a thin film of single crystal EuTe*, Physica B **201**, 438 (1994).

[97] M. R. Koblischka and R. J. Wijngaarden, *Magneto-optical investigations of superconductors*, Supercond. Sci. Technol. **8**, 199 (1995).

[98] T. Kasuya, *Exchange mechanisms in europium chalcogenides*, IBM J. Res. Developm. **14**, 214 (1970).

[99] R. T. Lechner, G. Springholz, T. U. Schülli, J. Stangl, T. Schwarzl, and G. Bauer, *Strain Induced Changes in the Magnetic Phase Diagram of Metamagnetic Heteroepitaxial EuSe/$PbSe_{1-x}Te_x$ Multilayers*, Phys. Rev. Lett. **94**, 157201 (2005).

[100] L. K. Hanamoto, A. B. Henriques, N. F. Oliveira, Jr. P. Rappl, E. Abramof, and Y. Ueta, *Sharp lines in the absorption edge of EuTe and $Pb_{0.1}Eu_{0.9}Te$ in high magnetic fields*, J. Phys.: Condens. Matter. **16**, 5597 (2004).

[101] W. Heiss, G. Prechtl, and G. Springholz, *Giant tunability of exciton photoluminescence emission in antiferromagnetic EuTe*, Phys. Rev. B **63**, 165323 (2001).

[102] A. B. Henriques, A. Wierts, and M. A. Manfrini, G. Springholz, P. H. O. Rappl, E. Abramof, and A. Y. Ueta, *Band-edge polarized optical absorption in europium chalcogenides*, Phys. Rev. B **72**, 155337 (2005).

[103] N. F. Oliveira, S. Foner, Y. Shapira, and T. B. Reed, *EuTe. I. Magnetic Behavior of Insulating and Conducting Single Crystals*, Phys. Rev. B **5**, 2634 (1972).

[104] J. Roche, *Axial vectors, skew-symmetric tensors and the nature of the magnetic field*, Eur. J. Phys. **22** 193 (2001).

[105] A. B. Henriques, M. A. Manfrini, P. H. O. Rappl and E. Abramof, *Modeling the dichroic absorption band edge and light-induced magnetism in EuTe*, Phys. Rev. B **77**, 035204 (2008).

[106] A. B. Henriques, E. Abramof, and P. H. O. Rappl, *Theory of near-gap second harmonic generation in centrosymmetric magnetic semiconductors: Europium chalcogenides*, Phys. Rev. B **80**, 245206 (2009).

[107] A. B. Henriques, G. D. Galgano, B. Díaz, P. H. O. Rappl, and E. Abramof, *Magnetic field dependence of the circular dichroism in EuTe* , J. Phys.: Condens. Matter **19**, 406234 (2007).

[108] B. Díaz, E. Granado, E. Abramof, P. H. O. Rappl, V. A. Chitta, and A. B. Henriques, *Magnetic resonant x-ray diffraction study of europium telluride*, Phys. Rev. B **78**, 134423 (2008).

Acknowledgments

This work would not have been possible without the help of many, whom I want to thank here for their support, valuable discussions, and technical assistance.

I greatly acknowledge Prof. Dr. Dmitri R. Yakovlev for his invaluable guidance and admirable help. I would like to thank Prof. Dr. Manfred Bayer for providing me the opportunity to carry out all the studies and his fruitful support. I am deeply grateful to Prof. Dr. Victor V. Pavlov, Prof. Dr. Roman V. Pisarev, and Dr. Anna V. Rodina from the Ioffe institute for the productive collaboration, fruitful discussions, and very helpful advices. Many thanks to David Brunne for the irreplaceable help in the laboratory and the countless discussions. I would like to thank Prof. Dr. Dietmar Fröhlich for providing unique advices and helpful references. I am thankful to Prof. Dr. André B. Henriques for his theoretical contributions on THG in EuX. I appreciate the collaboration with Dr. Benjamin Kaminski during the early stages of this work.

I would like to thank all members of the E2-chair for their support and the joyful times.

I owe my deepest gratitude to my parents Sigrid and Klaus for their continuous support in every respect. I am thankful to my sister Janine for her ongoing belief in me.